Functional role of RIM3 in the regulation of neuronal network excitability

Insights from transcriptomics and network activity analysis

Doctoral thesis

to obtain a doctorate

from the Faculty of Medicine

of the University of Bonn

Alexandra Lazaridis

from Moers

2025

Written with authorization of

the Faculty of Medicine of the University of Bonn

First reviewer: Prof. Dr. Susanne Schoch McGovern

Second reviewer: Prof. Dr. Tobias Gerd Rose

Day of oral examination: 28.02.2025

From the Department of Neuropathology

Table of Contents

List of Abbreviations

%BL	*percentage of baseline*
2xHeBS	*HEPES-buffered saline*
AAV	*adenovirus-associated viral particles*
AMPA	*α-amino-3-hydroxy-5-methyl-4-isoxazole-propionic acid*
AZ	*active zone*
BHK cells	*baby hamster kidney cells*
BME	*basal medium Eagle*
bp	*base pairs*
Ca^{2+}	*calcium*
CaMKIV	*calcium/calmodulin-dependent protein kinase IV*
CaMKK	*calcium/calmodulin-dependent protein kinase kinase*
cAMP	*cyclic adenosine monophosphate*
CaPO4	*calcium phosphate*
Ca_V	*voltage-gated calcium channel*
CAZ	*cytomatrix at the active zone*
cKO	*conditional knock-out*
CNS	*central nervous system*
CO_2	*carbon dioxide*
Da	*Dalton*
DAPI	*4',6-diamidino-2-phenylindole*
ddH_2O	*double-distilled water*
DEGs	*differentially expressed genes*
DIV	*days in vitro*
DKO	*double knock-out*
Dlx	*distal-less homeobox*
DMEM	*Dulbecco's modifed eagle medium*
DNA	*deoxyribonucleic acid*
dPBS	*Dulbecco's phosphate-buffered saline*
EDTA	*ethylenediaminetetraacetic acid*
EGFP	*enhanced green fluorescent protein*
EGTA	*ethylene glycol-bis(β-aminoethyl ether)-N,N,N',N'-tetraacetic acid*

E-I	*excitation-inhibition*
ER	*endoplasmic reticulum*
ES cells	*embryonic stem cells*
FA	*formic acid*
FBS	*fetal bovine serum*
FC	*Foldchange*
FCS	*fetal calf serum*
FDR	*false discovery rate*
FLP	*flippase*
GAD	*glutamate decarboxylase*
GO	*gene ontology*
HBSS	*Hank's balanced salt solution*
HEK293T cells	*human embryonic kidney 293T cells*
i.e.	*id est*
IBI	*inter-burst-interval*
IEG	*immediate early genes*
iGluSnFR	*intensity-based glutamate-sensing fluorescent reporter*
IMDM	*Iscove's modified Dulbecco's medium*
INBI	*inter-network-burst-interval*
iPSC	*induced pluripotent stem cells*
ISI	*inter-spike-interval*
KCl	*potassium chloride*
KO	*knock-out*
LTD	*long-term depression*
LTP	*long-term potentiation*
m/z	*mass-to-charge-ratio*
MAP2	*microtubuli associated protein 2*
MEA	*multielectrode array*
mEPSC	*miniature excitatory postsynaptic currents*
$MgCl_2$	*magnesium chloride*
mGluR	*metabotropic glutamate receptor*
mRNA	*messenger ribonucleic acid*

NaCl	*sodium chloride*
NaF	*sodium fluoride*
NES	*nuclear export signal*
NLS	*nuclear localization signal*
NMDA	*N-methyl-D-aspartate*
NT	*neurotransmitter*
PBS	*phosphate-buffered saline*
PFA	*paraformaldehyde*
PHP	*presynaptic homeostatic plasticity*
PI	*propidium iodide*
PKA	*protein kinase A*
PMSF	*phenylmethylsulfonyl fluoride*
ppm	*parts per million*
PSD	*postsynaptic density*
PSM	*peptide-spectrum match*
rAAV	*recombinant adenovirus-associated viral particles*
rcf	*relative centrifugal force*
RIM-BP	*RIM-binding protein*
RIMs	*Rab3-interacting molecules*
RNA	*ribonucleic acid*
RNA Seq	*RNA Sequencing*
rpm	*revolutions per minute*
SCZ	*schizophrenia*
SD	*standard deviation*
SDS	*sodium dodecyl sulfate*
SEM	*standard error of the mean*
SPS	*synchronous precursor selection*
SV	*synaptic vesicle*
TBS	*Tris-buffered saline*
TMT	*tandem mass tag*
Tris-HCl	*tris(hydroxymethyl)-aminomethan-hydrochlorid*
TTX	*tetrodotoxin*

VGCC	*voltage-gated calcium channel*
VGLUT2	*vesicular glutamate transporter 2*
WT	*wildtype*

1 Introduction

1.1 The Synapse

In the human brain billions of neurons form highly complex networks via inter-neuronal connections, called synapses. Synapses are specialized intercellular junctions that allow information to be transmitted from one neuron to another neuron or to a different cell type using chemical or electrical signaling. Chemical synapses can generally be categorized into three main compartments: a presynapse and a postsynapse, which are separated by a gap of approximately 20 nm, the synaptic cleft (Südhof, 2021).

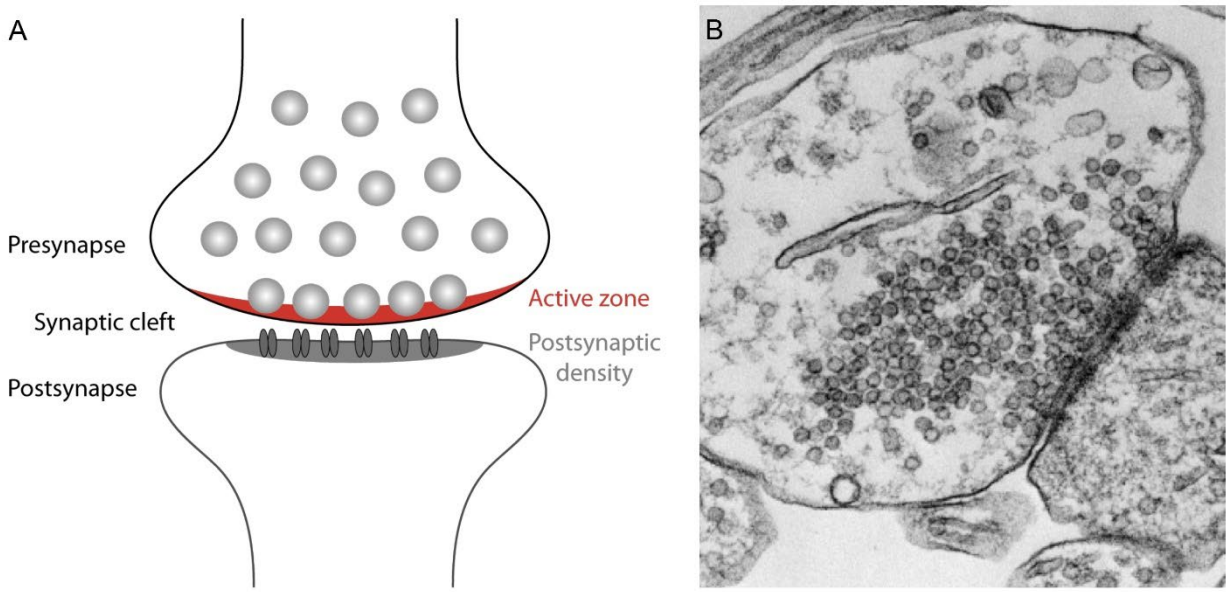

Figure 1.1: General structure of the synapse. (A) Cartoon depicting the main compartments of a synapse. The presynaptic terminal is separated from the postsynaptic neuron by the synaptic cleft. The presynaptic compartment contains vesicles that can release neurotransmitters into the cleft at a specialized release site, the active zone (AZ). Postsynaptically, neurotransmitters bind to receptors in the postsynaptic density (PSD) that elicit ionotropic or metabotropic signaling. **(B)** Electron micrograph of a hippocampal synapse showing the different synaptic compartments, such as synaptic vesicles, AZ and PSD. (Modified from Michel, 2015).

Information is passed throughout the axon of the presynaptic neuron in the form of rapid membrane depolarizations, so-called action potentials. Upon the arrival of an action potential at the presynaptic terminal, calcium channels in the presynaptic membrane open and the subsequent Ca^{2+}-influx triggers the release of neurotransmitters from synaptic vesicles into the synaptic cleft (Südhof, 2004). After crossing the synaptic cleft by diffusion,

neurotransmitters bind to specialized receptors in the postsynaptic membrane, which elicit an ionotropic (binding results in ion influx/efflux) or metabotropic (binding results in the activation of second messengers) response. This modulates the membrane potential of the postsynaptic neuron or initiates intracellular signaling cascades, respectively, thereby influencing the firing probability of the postsynaptic neuron (Smart and Paoletti, 2012).

The fine-tuned processes of neurotransmitter release and reception take place at specialized sections of the presynaptic and postsynaptic plasma membrane, which present themselves as electron-dense structures in electron microscopy images (Figure 1.1). In the presynaptic terminal, this area is called the active zone (AZ) and contains a complex subset of proteins that control the release of neurotransmitters into the synaptic cleft. The AZ is precisely aligned with the opposing electron-dense area of the postsynapse, the postsynaptic density (PSD), which contains a protein network specialized for neurotransmitter reception and subsequent signaling. Both, the AZ and the PSD are stable and persistent over time, but at the same time highly dynamic as they adapt to changes in activity, a process called synaptic plasticity (Ziv and Fisher-Lavie, 2014).

1.2 The presynaptic terminal

The main function of the presynaptic terminal is the release of neurotransmitters. Neurotransmitters are stored in synaptic vesicles and are released by fusion of the vesicles with the presynaptic plasma membrane in a highly regulated, Ca^{2+}-dependent process. This is mediated by a complex protein machinery at the active zone, which is also referred to as the cytomatrix at the active zone (CAZ) (Südhof, 2012).

1.2.1 Neurotransmitter release and the synaptic vesicle cycle

The release of neurotransmitters can generally be separated into docking, priming, fusion and recycling of synaptic vesicles (Figure 1.2), which is called the synaptic vesicle cycle (Südhof, 2004). The ability of vesicles to rapidly fuse with the plasma membrane is a major determining factor of synaptic transmission.

Neurotransmitters are produced in the neuronal soma or synthesized locally at the presynaptic terminal and are loaded into synaptic vesicles by specialized transporters. After neurotransmitter uptake, vesicles must be recruited to the AZ and tethered to the plasma membrane, which is referred to as docking (Südhof, 2004). While the exact mechanisms of this process are not fully understood, different AZ proteins have been implied to play a role, such as Munc18, Rab3A, RIMs and Synapsin (Becherer and Rettig, 2006; Coleman et al., 2008; Imig et al., 2014; Südhof, 2004). In a process called priming, the AZ protein Munc13-1 initiates the assembly of the trans-SNARE complex (Augustin et al., 1999; Ma et al., 2013), consisting of the plasma-membrane-bound proteins SyntaxinI and SNAP25, as well as Synaptobrevin/VAMP2, which is located on synaptic vesicles (Sutton et al., 1998). Priming renders vesicles release-ready and prepares them for rapid fusion with the plasma membrane upon the arrival of an action potential (Südhof, 2004).

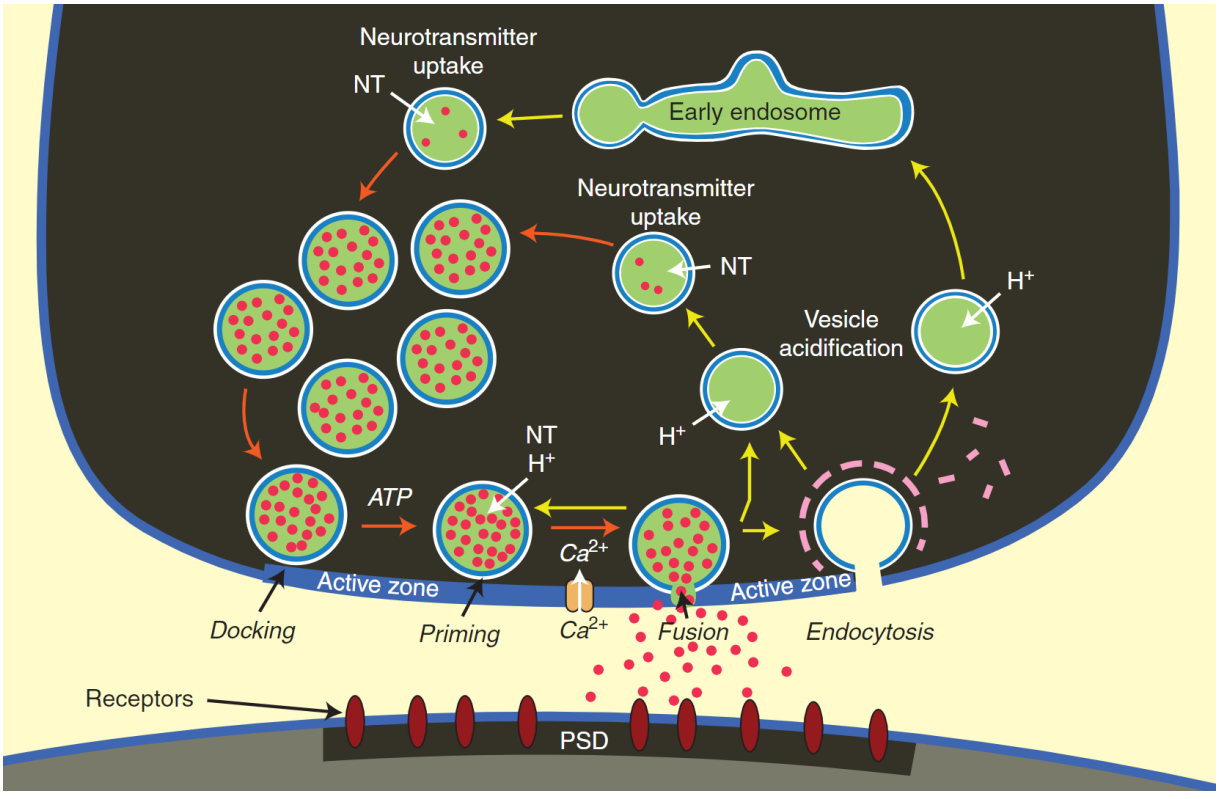

Figure 1.2: The synaptic vesicle cycle. A presynaptic nerve terminal (black) and a post-synapic neuron (grey) are depicted schematically. The synaptic vesicle cycle can be separated into docking, priming, fusion and recycling (endocytosis). First, synaptic vesicles (green circles) are filled with neurotransmitters (NT; red dots) by active transport (neurotransmitter uptake). In preparation to synaptic exocytosis, synaptic vesicles are docked at the active zone (AZ) and

primed, which renders the vesicles competent to respond to a Ca^{2+}-signal. When an action potential depolarizes the presynaptic membrane, Ca^{2+} channels open, causing a local increase in intracellular Ca^{2+} at the AZ that triggers vesicle fusion. Released neurotransmitters then bind to receptors at the postsynaptic density (PSD). After fusion pore opening, synaptic vesicles can ~~probably~~ recycle via different pathways: local refilling with neurotransmitters without undocking or with undocking, or full recycling via an endosomal pathway. Red arrows and yellow arrows indicate the processes of exocytosis and recycling, respectively. (From Südhof and Rizo, 2011).

The presynaptic plasma membrane exhibits a high abundance of voltage-gated calcium channels (VGCC) which open when an action potential arrives and allow influx of Ca^{2+}-ions into the presynapse (Sheng et al., 1998). Action-potential induced Ca^{2+} entry is then recognized by the Ca^{2+}-sensor Synaptotagmin-1, which is located on the membrane of synaptic vesicles (Brose et al., 1992; Chang et al., 2018). Ca^{2+}-ions bind to Synaptotagmin-1 and force it to interact with the SNARE complex and the plasma membrane, triggering the fusion of readily releasable synaptic vesicles with the plasma membrane and thus the release of neurotransmitters into the synaptic cleft. Synaptic vesicles can fuse either partially or completely with the plasma membrane, which determines the way they are recycled and thus the time-course of their re-availability (Südhof, 2004; Südhof and Rizo, 2011).

Rapid neurotransmitter secretion upon presynaptic action potential arrival highly depends on correct spatial positioning of synaptic vesicles and VGCCs: keeping the sites of Ca^{2+}-influx in close proximity to Ca^{2+}-sensor Synaptotagmin-1 is essential for effective vesicle fusion and has to be mediated by various AZ components (Südhof, 2013).

1.2.2 Molecular organization of the active zone

The precise spatio-temporal control of synaptic vesicle release requires highly organized structures at the active zone. Apart from proteins directly involved in the fusion of synaptic vesicles like the beforementioned members of the SNARE-complex and Synaptotagmin-1, several scaffolding proteins have been shown to play a crucial role in the organization and function of the presynapse (Schoch and Gundelfinger, 2006; Südhof, 2012). Scaffolding proteins form a molecular grid and enable correct positioning of presynaptic proteins and synaptic vesicles, as well as localizing and tethering of signaling components into complexes. By this they are able to regulate signaling efficiency, in this case

neurotransmitter release (Michel et al., 2015). Apart from interactions with the synaptic vesicle release machinery, presynaptic scaffolding proteins bind to VGCCs, cell adhesion molecules and cytoskeletal components (Held and Kaeser, 2018).

Several scaffolding protein families have been identified to be enriched at the presynaptic active zone: Munc13 (mammalian Unc13), RIMs (Rab3 interacting molecules), RIM-BP (RIM binding protein), Piccolo/Bassoon, ELKS and Liprins- α (Schoch and Gundelfinger, 2006). By linking presynaptic components together, they are organizers of the AZ and exert different functions: Munc13, for example, has been shown to be important for priming of synaptic vesicles, while α-Liprins seem to play a role in the formation and maintenance of the AZ via interaction with the protein tyrosine phosphatase LAR (Schoch and Gundelfinger, 2006).

As shown in Figure 1.3, RIM occupies a central position at the active zone, interacting with all other AZ enriched proteins and many other important presynaptic components, such as VGCCs and Rab3 and Synaptotagmin-1, proteins located on synaptic vesicles (Schoch et al., 2002; Wang et al., 1997).

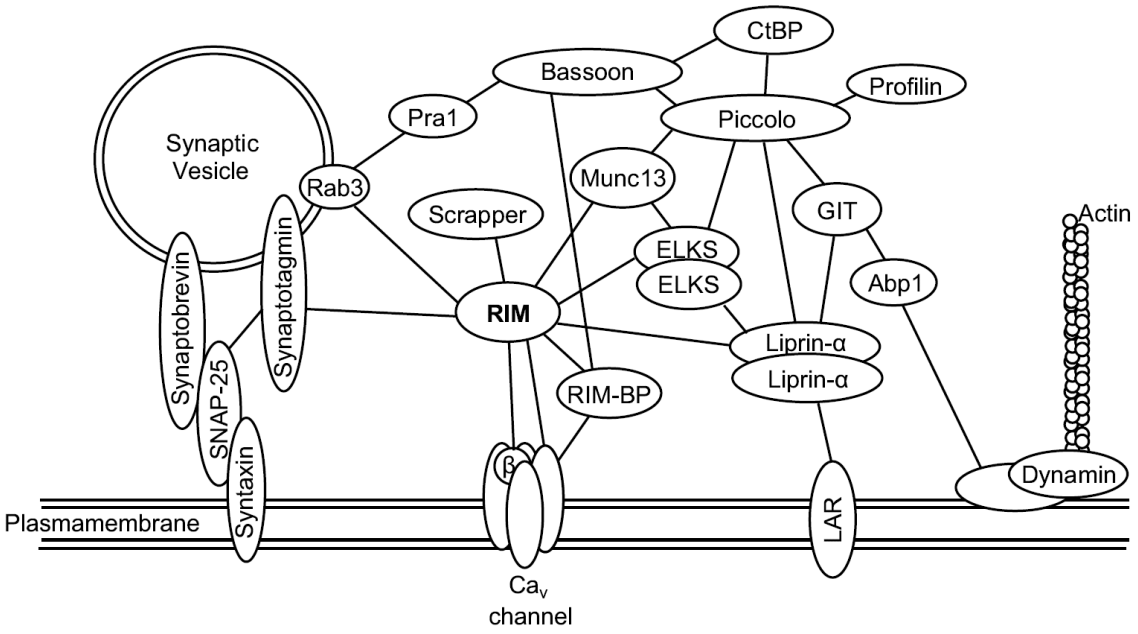

Figure 1.3: Organization of the cytomatrix at the active zone (CAZ). The cartoon illustrates the interactions of the proteins at the active zone. RIM is closely associated with the enriched core CAZ proteins, such as Bassoon, Munc13, ELKS and Liprin-α. Additionally, its function is

dependent on binding to Rab3, Synaptotagmins, RIM-BPs and Ca^{2+}-channels. (From Müller, 2020).

Scaffolding proteins do not only play a role in the presynapse: in the opposing PSD, important scaffolding proteins like PSD95, Shank and Homer1 mediate the localization of receptors in the postsynaptic plasma membrane and link them to intracellular signaling cascades, thereby enabling postsynaptic responses and adaptation mechanisms (Kaizuka and Takumi, 2018).

1.3 Synaptic plasticity

Synaptic plasticity refers to the process of changing the current state of a neuronal network in response to physiologically relevant stimuli. To date, several forms of synaptic plasticity are known: short-term plasticity, long-term plasticity and homeostatic plasticity.

Short-term plasticity describes changes in the strength of synaptic transmission that only last for milliseconds to seconds. These events occur mostly during ongoing transmission and are characterized by transient changes in presynaptic neurotransmitter release (Regehr, 2012). When synapses with low release probability experience increased stimulation, vesicle release is enhanced, a process called short-term facilitation. In case of synapses with high release probability rapid decrease in transmitter release can be monitored when the synapse is subjected to sustained activity, a mechanism which is called short-term depression. (Zucker and Regehr, 2002)

Long-term plasticity, on the other hand, describes activity-dependent changes in synaptic efficacy persisting from hours to weeks. There are two opposing forms: Long-term potentiation (LTP) is characterized by an increase in synaptic strength after repetitive activation, while long-term depression (LTD) describes long-lasting decreases in synaptic strength, induced by low levels of activation (Citri and Malenka, 2008). Among other things, pre- and postsynaptic increases in Ca^{2+}-concentrations (Castillo, 2012; Zalutsky and Nicoll, 1990) and PKA/cAMP signaling (Nguyen and Woo, 2003; Weisskopf et al., 1994) are essential for these forms of synaptic plasticity.

The strengthening and weakening of synapses through LTP and LTD are thought to be the basis of learning and memory (Nabavi et al., 2014; Smolen et al., 2019; Whitlock et al., 2006). Without an active counterbalance though, LTP and LTD would drive activity in a self-reinforcing way towards hyperexcitability or complete quiescence, respectively. Homeostatic plasticity functions as a regulating counterpart to prevent these extreme states of neuronal activity (Turrigiano and Nelson, 2004).

1.3.1 Homeostatic plasticity

Homeostatic plasticity refers to the ability of neurons to compensate drastic changes in activity to move back towards a physiological state, thereby stabilizing neuronal and circuit function (Turrigiano, 2012). On the level of synaptic transmission, perturbations are rebalanced by changing either the amount of presynaptic neurotransmitter release or the expression and localization of postsynaptic receptors (Davis, 2013).

In 1998, Turrigiano et al. first demonstrated homeostatic plasticity in mammalian central neurons. In experiments with primary cortical neurons from rats, chronic blockade of action potential firing with the voltage-dependent sodium channel blocker Tetrodotoxin (TTX) increased the amplitude of miniature excitatory postsynaptic currents (mEPSC). Conversely, chronic elevation of neuronal activity with the $GABA_A$-receptor antagonist Bicuculline resulted in decreased mEPSC amplitudes. Extensive research has attempted to elucidate the underlying mechanisms of these homeostatic responses.

The most investigated form of homeostatic plasticity is the regulation of postsynaptic receptor expression, termed synaptic scaling (Figure 1.4, top panel). Localization and expression of both AMPA (α-amino-3-hydroxy-5-methyl-4-isoxazolepropionic acid) and NMDA (N-methyl-D-aspartate) receptors have been shown to be homeostatically regulated upon chronic activity perturbations (Watt et al., 2000). This process takes several hours to days since it requires new protein synthesis (Sutton et al., 2006; Turrigiano, 2011). Synaptic scaling has been shown to be highly dependent on Ca^{2+} signaling: upon chronic inhibition, CaMKIV (calcium/calmodulin-dependent protein kinase IV) and CaMKK (calcium/calmodulin-dependent protein kinase kinase) are essential for the enhanced transcription of receptor subunits and subsequent positioning of receptors

in the postsynaptic membrane (Goold and Nicoll, 2010; Ibata et al., 2008). Another mechanism of synaptic scaling involves the immediate early gene Homer1a, which is likewise induced in a calcium-dependent manner and regulates the postsynaptic membrane localization of mGluRs (Hu et al., 2010; Turrigiano, 2012).

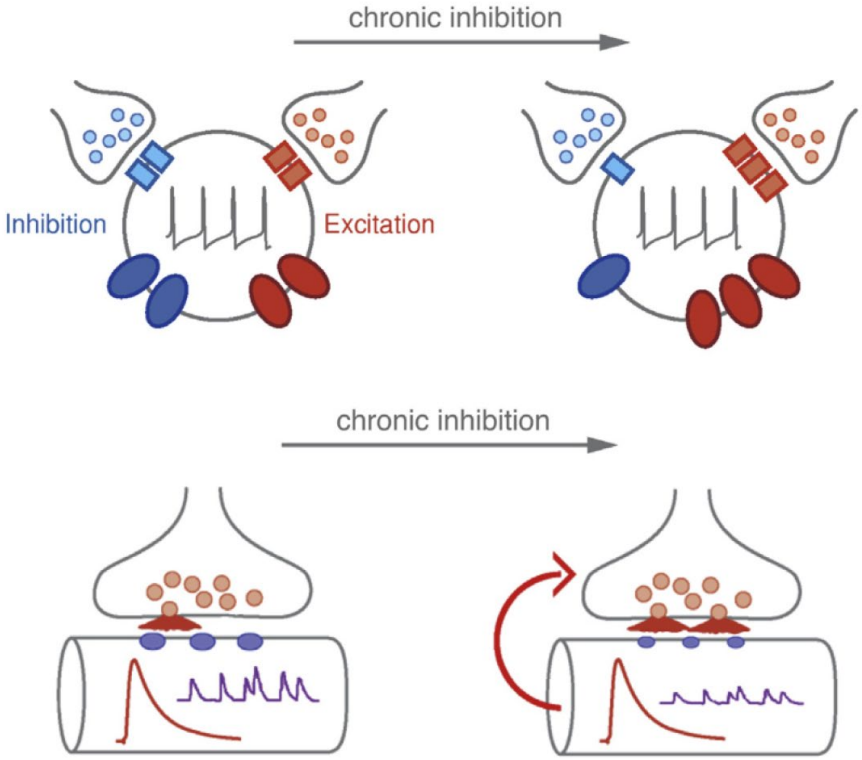

Figure 1.4: Homeostatic mechanisms offset changes in neuronal excitability back to baseline. Top panel: Synaptic scaling. Upon chronic activity inhibition, neurons rescale the ratio of depolarizing (= excitatory) postsynaptic receptors (red ovals) and postsynaptic receptors opposing depolarization (= inhibitory; blue ovals). This results in higher excitability, enabling the neuron to regain the firing rate it had prior to activity perturbation. Bottom panel: in presynaptic homeostatic plasticity, inhibition due to perturbation of postsynaptic receptors (blue ovals) leads to retrograde signaling to the presynapse and subsequent increase in neurotransmitter release. As a result, the net postsynaptic response (red trace) is adjusted back to the initial set-point, although postsynaptic responses to individual release events remain smaller (blue trace). The enhanced neurotransmitter output is mediated by increased Ca^{2+}-influx and number of readily releasable vesicles. (From Müller, 2020).

Changes in neurotransmitter release, as they occur in presynaptic homeostatic plasticity (PHP; Figure 1.4, bottom panel), can be rapidly inducible and have been shown to be mediated by different mechanisms: Modulation of presynaptic Ca^{2+} influx through VGCCs,

changes in Ca^{2+}-release-coupling (distance between sites of Ca^{2+} influx and Ca^{2+} sensors on synaptic vesicles) and adaption of the pool size of readily-releasable vesicles at the presynaptic active zone (Delvendahl and Müller, 2019). Some important effector molecules have been characterized for these forms of homeostatic plasticity, among them RIM1/2 (Müller et al., 2012), RIM-BP (Müller et al., 2015) Rab3 (Müller et al., 2011), and SRPK2 (serine arginine protein kinase 2) (Müller et al., 2022).

1.3.2 Regulating the excitation-inhibition balance in cortical networks

In addition to stabilizing activity on the level of individual neurons, homeostatic plasticity can act at a network level to coordinate changes in excitability across multiple neurons to stabilize network function (Tien and Kerschensteiner, 2018).

Cortical networks consist of excitatory and inhibitory neurons, whose connections construct highly organized neuronal circuits that control higher order information processing (Yizhar et al., 2011). Excitatory neurons in the central nervous system mainly use glutamate as their neurotransmitter and project over wide distances, while the majority of inhibitory neurons use gamma-aminobutyric acid (GABA) and form circuits with nearby excitatory neurons, as so-called interneurons (Petroff, 2002). As interneurons project onto numerous excitatory neurons at once, they modulate and control excitatory activity, as well as synchronize cortical network activity (Tremblay et al., 2016). This form of synchronization seems to play an important role in information processing (Saalmann, 2014; Singer, 1993). Through feedback or feedforward inhibition, alterations in excitatory activity by different stimuli are matched with coordinated changes in inhibitory activity (Yizhar et al., 2011). Other neurotransmitters such as serotonin, acetylcholine, noradrenaline and dopamine can elicit either excitatory or inhibitory responses and thereby exert different neuromodulatory functions in the central nervous system (Hyman, 2005; Pitzer, 2019).

For intact neuronal communication and cortical network function, the maintenance of a finely adjusted balance between excitation (E) and inhibition (I) is essential. Several studies have shown that even small changes in the excitation-inhibition balance (E-I balance) of such networks can lead to runaway excitation (Chagnac-Amitai and Connors,

1989; Kriegstein, 1987), altered experience-dependent plasticity (Hensch et al., 1998; Huang et al., 1999) and impaired sensory responses in the primary visual cortex (Nelson, 1991). An important part of keeping firing rates and excitability at a stable level in cortical networks consists of dynamic adaptations of the relative strengths of excitatory and inhibitory feedback onto pyramidal neurons. Here not only alterations in synaptic transmission through changes in neurotransmitter release and postsynaptic receptor expression are relevant, but also adjustments of cell-type specific connectivity (Turrigiano and Nelson, 2004). In dissociated cortical networks, it was shown that chronic activity blockade resulted in a reduction of functional inhibitory synapses onto pyramidal neurons (Kilman et al., 2002).

The maintenance of an appropriate E-I balance seems to be highly relevant for information processing, working memory, cognition and social behavior (Ferguson and Gao, 2018; Sohal and Rubenstein, 2019; Yizhar et al., 2011). Many neuropsychiatric conditions have been associated with pathological alterations in local circuit excitability (Sohal and Rubenstein, 2019). Although being a simplified concept, the E-I balance and its disturbances have emerged in the recent years as a framework for the pathogenesis of many neurological and psychiatric symptoms, such as they occur in epilepsy (Scharfman, 2007), schizophrenia (Foss-Feig et al., 2017), affective disorders (Fee et al., 2017) and autism (Culotta and Penzes, 2020).

In addition to homeostatic plasticity mechanisms, imbalances between excitation and inhibition can also derive from defects in developmental processes, such as neuronal morphogenesis and synapse formation (Sohal and Rubenstein, 2019). One example are Neurexins and Neuroligins: by forming a trans-synaptic complex these cell adhesion molecules precisely link the presynaptic active zone to the postsynaptic density, thereby being highly relevant for synaptogenesis throughout development (Cao and Tabuchi, 2017). Mutations and change-of-function of both molecules have been associated with alterations of the E-I balance (Cline, 2005; Levinson and El-Husseini, 2005) and the emergence of schizophrenia and autism (Hu et al., 2019; Jiang et al., 2018; Kirov et al., 2009).

1.4 RIM protein family

The RIM family of multidomain proteins was first identified by the interaction of RIM1α with the synaptic vesicle protein Rab3a, which termed them Rab3-interacting molecules, in short RIM (Wang et al., 1997). In the following years, extensive research on the molecular and genetic structures, as well as neuronal functions of RIM proteins, identified them as key players in the presynaptic active zone.

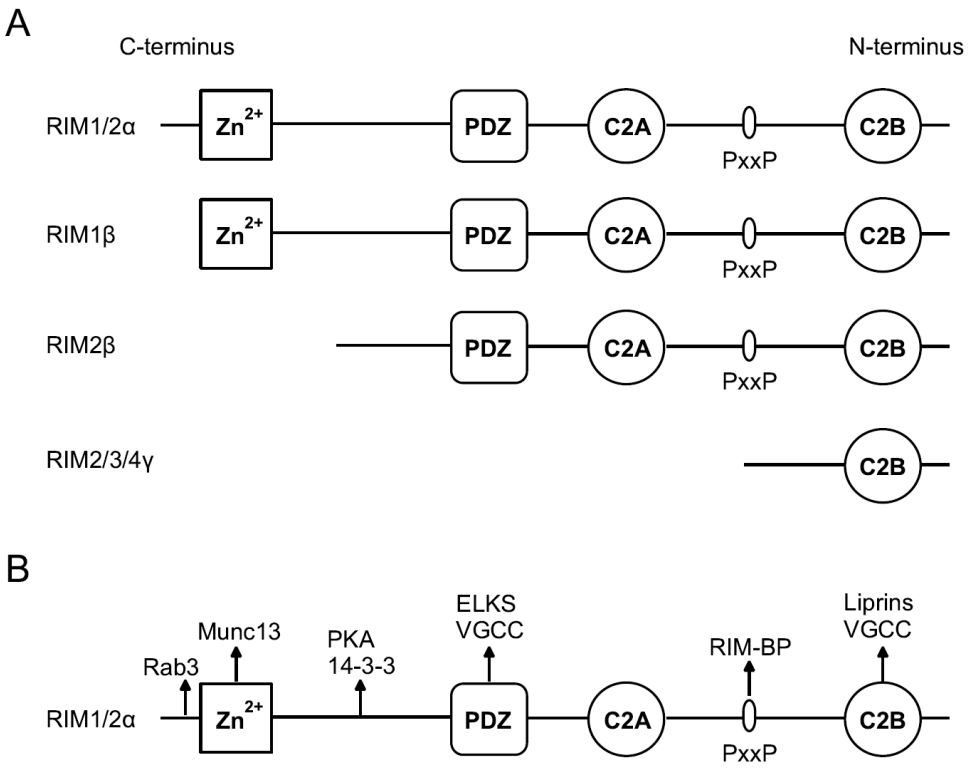

Figure 1.5: Domain structure of the RIM protein family. (A) RIM1α and RIM2α are the largest members and compose of all domains: Zn^{2+}-finger, PDZ, C2A and C2B domains. Between the C2 domains a proline-rich region (PxxP) is located. The shortest isoforms are the γ-RIMs which only consist of the C2B domain and an isoform specific N-terminal sequence. **(B)** Interaction partners of the different RIM1/2α domains. (From Müller, 2020).

The RIM protein family is encoded by four different genes (*Rims1-4*) and expressed in three variants through alternative splicing: α, β and γ (Figure 1.5 A). RIM1α and RIM2α are the largest members and contain the full RIM structure: an N-terminal Zn^{2+}-finger domain, a central PDZ and C2A domain, and a C-terminal C2B domain. β-RIMs are almost

identical to their alpha variants and contain all domains except the Rab3-binding part of the zinc finger domain in RIM1β and the whole zinc finger in RIM2β. The shortest members of the RIM family are the γ-variants RIM2γ, RIM3γ and RIM4γ, which contain only the C2B domain and an isoform-specific N-terminus. Unlike RIM1/2, RIM3 and RIM4 are not alternatively spliced and exist only as γ-variants (Mittelstaedt et al., 2010; Wang and Südhof, 2003).

To date multiple interaction partners have been proposed and validated for the different α-RIM domains (Figure 1.5 B). The C2B-domain, for example, has been shown to bind to α-Liprins, Synaptotagmin-1 and the β4-subunit of VGCCs, indicating a function in coupling of Ca^{2+}-influx to synaptic vesicles (Schoch et al., 2002; Uriu et al., 2010). While this applies to the C2B-domain of the large RIM isoforms, the binding characteristics, interaction partners and subsequent functions of the C2B-domain in γ-RIMs are still unresolved and remain to be elucidated.

1.4.1 Synaptic functions of large RIM isoforms

In the recent years it has been shown that RIM1α does not only interact with the SV protein Rab3a, but also with most CAZ enriched core proteins, VGCCs and many other essential presynaptic components (Deng et al., 2011; Schoch et al., 2002; Shibasaki et al., 2004; Takao-Rikitsu et al., 2004; Wang et al., 2000). This puts RIM1/2 in a central position at the AZ and makes it highly relevant for presynaptic function, as studies with RIM1α KO and conditional RIM1/2 double knock-out (DKO) neurons revealed. Neurons lacking RIM1α exhibit a considerable reduction in release probability (Calakos et al., 2004; Castillo et al., 2002; Fourcaudot et al., 2008; Han et al., 2011; Schoch et al., 2002), which can be partly explained by decreased Ca^{2+}-influx and reduced vesicle to Ca^{2+}-channel coupling (Fourcaudot et al., 2008; Han et al., 2011; Kaeser et al., 2011). Furthermore, a reduction in Ca^{2+}-sensitivity was also shown to be a reason for the decreased release probability (Han et al., 2011).

RIM1α has been identified as a key player in mediating presynaptic plasticity (Südhof, 2012b). Short-term plasticity has been shown to be impaired after KO of RIM1α, together with the changed release probabilities (Fourcaudot et al., 2008; Schoch et al., 2002).

Presynaptic LTP and LTD both were abolished in the absence of RIM1α in various synapse types (Castillo et al., 2002; Chevaleyre et al., 2007; Fourcaudot et al., 2008; Lachamp et al., 2009; Pelkey et al., 2008), in a PKA-dependent manner (Castillo et al., 2002; Fourcaudot et al., 2008; Pelkey et al., 2008). In addition to these forms of plasticity, RIM1α seems to play a crucial role in presynaptic homeostatic plasticity as well: at the neuromuscular junction of Drosophila melanogaster, loss of the RIM homolog has been shown to block the homeostatic enhancement of presynaptic neurotransmitter release. The study also revealed that primarily the ability of RIM to modulate the size of the readily-releasable vesicle pool was required for homeostatic responses (Müller et al., 2012). Since Rab3a also seems to be involved in presynaptic homeostasis in Drosophila melanogaster (Müller et al., 2011), it has been proposed that the interaction of RIM and Rab3a plays a role in homeostatic plasticity by linking synaptic vesicles to Ca^{2+} channels. In mammalian central nervous system synapses, it was shown that RIM1α was redistributed during chronic blockade of network activity, which lead to increased RIM1α levels in a subpopulation of synapses (Lazarevic et al., 2011). While the work of Lazarevic et al. describes homeostatic changes solely on the structural level, a recent study first investigated the functional relationship between RIM1α and homeostatic plasticity in mammalian CNS neurons (Müller et al., 2022), reporting the absence of silencing-induced, homeostatic plasticity in hippocampal RIM1/2 DKO neurons. Furthermore, the study uncovered that RIM1α-dependent homeostatic upscaling is achieved by increasing the number of RIM1α nanoclusters at the active zone and is mediated by phosphorylation of RIM1α by its recently identified binding partner SRPK2 (Müller et al., 2022).

1.4.2 RIM3

While the large RIM isoforms have been extensively studied during the last years, only little is known about the small isoforms RIM3γ and RIM4γ. For RIM4, unpublished data from our lab suggest a role in motor coordination since KO of RIM4 induces an ataxia-like motor phenotype. Knock-out of RIM3, however, did not result in motor phenotypes or any other overt deficits. This poses the question, if and how RIM3 participates in neuronal function.

In-situ hybridization experiments performed by Liang et al. in 2007 and Uriu et al. in 2010 indicated highest expression of RIM3 in the thalamus, followed by neuronal subpopulations in cortex layer III-IV, the hippocampal CA1-CA3 region and dentate gyrus, as well as the cerebellar Purkinje cell and granular cell layer. Single-cell RNA Seq data from Linnarsson Lab's database mousebrain.org indicated that RIM3 expression in the thalamus predominates in excitatory neurons. In the cortex, however, RIM3 seems to be mainly expressed in inhibitory interneurons, mostly cholecystokinin-positive interneurons and long-ranging, somatostatin-positive, sleep-active interneurons (Linnarsson Lab, 2024).

On a subcellular level, RIM3 has been shown to exhibit a much wider distribution, compared to the distinct presynaptic localization of α- and β-RIMs: Double immunostainings with primary hippocampal neurons showed colocalization of RIM3 with presynaptic marker Synapsin, the dendritic marker MAP2, and postsynaptic marker PSD-95 (Alvarez-Baron et al., 2013). Localization of RIM3 to the nucleus has also been observed (Michel, 2015). This divergent localization indicates that RIM3 might have a broader spectrum of functions than α-RIMs and might not be limited to presynaptic vesicle release.

1.4.2.1 Possible role of RIM3 in Ca^{2+}-signaling, synaptic vesicle anchoring and neuronal growth

First studies with non-neuronal cells suggested a role of RIM3 in the modulation of presynaptic Ca^{2+}-influx through binding to voltage-gated calcium channels (VGCC) and enhancing their density in the plasma membrane, as well as in the regulation of synaptic vesicle anchoring. Co-expressing VGCCs and RIMs in cultured BHK cells revealed that RIM3 inhibited the inactivation of VGCCs via binding to accessory β-subunits in a similar way as α-RIMs, leading to prolonged Ca^{2+} influx. However, RIM3 seemed to be less effective in binding to VGCCs than α-RIMs (Uriu et al., 2010). In HEK293T cells, RIM3 was observed to positively regulate the density of the VGCC subunit Ca_V 1.3 in the plasma membrane (Picher et al., 2017). Interestingly, knock-down of RIM3 in neuroendocrine PC12 cells lead to an increased number of docked vesicles, proposing a role as a negative

regulator of synaptic vesicle anchoring, antagonistic to α-RIMs (Uriu et al., 2010). Conversely, another study showed that overexpression of RIM3 in PC12 cells lead to increased calcium-evoked exocytosis (Wang et al., 2000). Although the exact function and direction of RIM3 effects remain unclear, these results point towards a possible role in regulating neurotransmitter release.

Alvarez-Baron et al. (2013) first investigated the effects of RIM3 inactivation in mammalian hippocampal neurons and discovered a potential role of RIM3 in neuronal growth and development. Knock-down of RIM3 in hippocampal neurons leads to defects in neuronal arborization *in vitro* and *in vivo*, with a drastic decrease in dendritic arbor complexity, axon length, number of dendritic spines and a substantial reduction in the number of functional synapses. The lower synapse density also leads to lower mEPSC frequencies in knockdown neurons (Alvarez-Baron et al., 2013).

Furthermore, a role of RIM3 in signaling between synapses and the nucleus has been proposed (Michel, 2015). Synapse-to-nucleus signaling is assumed to be essential for long-term plastic changes in response to neuronal activity. While there are several ways synapses can signal to the nucleus, such as through regenerative intracellular calcium waves or signaling endosomes, another way is through synaptic, soluble molecules being transported to the nucleus, where they activate specific transcriptional programs (Ch'ng and Martin, 2011; Lim et al., 2017). RIM3 contains a nuclear localization signal (NLS) and a nuclear export signal (NES) (Michel, 2015). These sequences govern the translocation of a molecule in and out of the nucleus (Lange et al., 2007). Additionally, RIM3 has been shown to interact with several members of the importin family (Michel, 2015), which bind to the NLS and by this mediate the transport to the nucleus (Lange et al., 2007).

The results of these studies suggest that RIM3 might have additional functions, which are different from α-RIMs. Whether these observed changes have functional implications on neuronal network activity remains to be elucidated.

1.4.2.2 RIM3 in neuronal pathologies

Synapses are the interconnections that link single neurons into functional circuits and networks. Therefore, it is not surprising that dysregulation of neuronal activity due to inappropriate changes in synapse number and function are believed to play an important role in the pathogenesis of neurological and neuropsychiatric conditions, such as epilepsy, schizophrenia and Parkinson's disease (Lima Caldeira et al., 2019; Obi-Nagata et al., 2019).

Interestingly, a study analyzing postmortem brains of patients with schizophrenia discovered an upregulation of RIM3 gene transcripts in the amygdala (Weidenhofer et al., 2009). Another study showed upregulation of RIM3 in the prefrontal cortices of schizophrenic patients (Hakak et al., 2001). Schizophrenia (SCZ) is a complex neuropsychiatric condition, characterized by severely altered perception, delusions, hallucinations, inadequate or reduced emotional responses, cognitive impairment, and social withdrawal, often associated with considerable psychological strain for those affected (Mueser and McGurk, 2004; Nucifora et al., 2019). Since the exact etiology is still unknown and treatment is often insufficient, it is of great relevance to achieve a better understanding of the underlying pathogenic mechanisms. Furthermore, mutations of the *Rims3* gene have been reported in individuals with autism (Kumar et al., 2010), a neurodevelopmental diversity which shows altered processing of sensory inputs and atypical social behavior and is believed to have a shared etiology with schizophrenia (Rzhetsky et al., 2007).

Association of RIM3 with both schizophrenia and autism suggest that RIM3 might play an important role in information processing, possibly mediated by cortical interneuron function. Based on the beforementioned studies, presynaptic functions in Ca^{2+} signaling and plasticity, as well as neuronal development and connectivity might play a role, with implications for the maintenance of an appropriate E-I balance in neuronal networks.

1.5 Aims of the project

While the neuronal functions of α-RIMs have been extensively studied, only little is known about RIM3. In the few studies that have attempted to shed light on its functions, RIM3 was investigated in non-neuronal cells or using a knock-down strategy. The generation of constitutive and conditional RIM3 KO mouse lines in our lab enables us to unveil potential functions of RIM3 in a more physiological and comprehensive background. This study serves as a first functional characterization and addresses the following aims:

Firstly (1), we want to assess how the deletion of RIM3 influences gene and protein expression in thalamus and cortex tissue, by means of RNA-sequencing, mass spectrometry and subsequent bioinformatic analysis. Transcriptomics and proteomics can help to unravel possible functions and processes RIM3 might be involved in.

The second aim of this project (2) is the establishment and optimization of multielectrode arrays (MEA) in our lab to examine the role of RIM3 in neuronal network activity. We will optimize the recording conditions and determine the influence of culture density on neuronal network activity. Additionally, we aim to establish different approaches with this method, such as the chemical induction of homeostatic plasticity, as well as investigate the role of GABAergic signaling in our networks.

In the third aim (3), we want to characterize the functional consequences of RIM3 loss on activity and excitability of cultured neuronal networks, using MEA. Here, we are particularly interested in how RIM3 KO affects homeostatic plasticity on the network level. Furthermore, we will investigate the effects of RIM3 deletion on spontaneous network activity and firing patterns at different developmental stages and under different network conditions, such as different culture density. Thereby, we aim to assess potential alterations of the E-I balance upon RIM3 deletion, possibly due to defects in synaptic transmission and/or neuronal development and connectivity.

As a fourth goal (4), we further want to analyze the specific functions of RIM3 in glutamatergic and GABAergic neurons. To this end, cell-type specific knock-outs will be generated and similarly subjected to MEA recordings and analysis. In contrast to ubiquitous gene knockout, this will enable us to attribute possible phenotypes to a

particular cell type or transmitter system. Here, we are especially interested in how RIM3 contributes to cortical interneuron function.

Taken together, this study will provide new insights into the neuronal processes RIM3 might be involved in and which downstream targets it might affect, as well as the functional role of RIM3 in the development of spontaneous neuronal network activity, homeostatic network plasticity, and excitatory vs. inhibitory neuronal function.

2 Materials and methods

Chemicals were purchased from Sigma-Aldrich (Taufkirchen, Germany) or from the manufacturers and resellers indicated in the methods description. Used materials are mentioned in the text if necessary.

2.1 Animal models

Constitutive and conditional RIM3 knock-out (KO) mice were used in this study. The first RIM3 KO allele was generated utilizing embryonic stem (ES) cells produced by the Knockout Mouse Project (KOMP) consortium. JM8A3.N1 ES cells carrying the RIM3 targeting vector (Rims3tm1a(KOMP)Wtsi; ES cell line JM8A3.N1; targeting project CSD34392) were injected into the blastocysts of Balb/c mice. After germ line transmission, the splice acceptor lacZ gene trap cassette inserted between exons 3 and 4 lead to splicing of RIM3 after exon 3, which disrupted the endogenous RIM3 transcript (Michel, 2015; Picher et al., 2017). Recombination with a FLP-recombinase expressing mouse line (Dymecki, 1996) resulted in the excision of the gene trap cassette to generate $RIM3^{flox/flox}$ mice (conditional knock-out). $RIM3^{flox/flox}$ mice should express wild-type levels of RIM3 but can be converted to a KO by excision of exon 4 through Cre-mediated recombination (Michel, 2015). Constitutive RIM3 KO mice were generated by crossing $RIM3^{flox/flox}$ mice with transgenic mice that express Cre-recombinase ubiquitously under the PGK promoter (Lallemand et al., 1998), leading to disruption of RIM3 expression in the whole organism. Conditional KO of RIM3 was achieved by virally delivering Cre-expression into cultured $RIM3^{flox/flox}$ neurons (pLenti-NLS-Cre-EGFP), with an inactive form of Cre recombinase (ΔCre) as control. For cell-type specific KO, Cre-expressing viruses under control of cell-type specific promoters were used (see Section 2.9.6).

The following primers were used for genotyping of each mouse line. Const. RIM3 KO line: 5’-GGACCACACTGCAATGCTAA-3’ and 5’-GTGAGTAATGGGAGGCAGGA-3’, product size 472 base pairs (bp) for KO band. 5’-GGACCACACTGCAATGCTAA-3’ and 5’-ACCAGACTCCAAAGCCCTCT- 3’, product size 324 bp for wildtype band. RIM3flox line: 5’-GGACCACACTGCAATGCTAA-3’ and 5’-ACCAGACTCCAAAGCCCTCT- 3’, product size 485 bp for floxed gene band, product size 324 bp for wildtype band. 5’-GGACCACACTGCAATGCTAA-3’ and 5’-GTGAGTAATGGGAGGCAGGA-3’, product

size 1288 bp for floxed gene band, product size 1000 bp for wildtype band. Expression of the Cre recombinase was detected using 5'-CATTTGGGCCAGCTAAACAT-3' and 5'-CCCGGCAAAACAGGTAGTTA-3', product size 454 bp. DNA was sampled from the tails of mice. Genotyping was performed by Eva Schönhense, Nesrine Melliti, Pia Scheidt and Shayne Gilgenbach.

The constitutive KO was used for transcriptomics and proteomics experiments. For all other KO experiments, the conditional KO was used.

2.2 RNA Sequencing and transcriptomics approach

Sample preparation

Cortex and thalamus sections of five RIM3 wildtype and five constitutive RIM3 knockout mice were freshly dissected, frozen in liquid nitrogen and kept at -80 °C before RNA extraction. For isolation of RNA the RNeasy Midi Kit (Qiagen) was used, following the manufacturer's instructions and evaluated using a NanoDrop1000 spectrophotometer (Thermo Scientific, Waltham, USA).

RNA Sequencing

For RNA sequencing (RNA Seq) experiments, library preparation was performed using the QuantSeq 3´-mRNA-Seq Library Prep kit (Lexogen). The library was sequenced on a HiSeq 2500 sequencer (Illumina) with 1x50 bp single-end reads and a coverage of 10.000 reads per sample. Quality control was performed using a TapeStation System 4200 (Agilent) and RNA was quantified with a Qubit RNA Assay Kit (Thermo). RNA Sequencing was performed by the NGS Core Facility of the University of Bonn.

2.3 Mass spectrometry and proteomics approach

Sample preparation

Cortex and thalamus sections of five constitutive RIM3 wildtype and five constitutive RIM3 knockout mice were freshly prepared and kept in liquid nitrogen or frozen at

-80°C before protein purification. Lysis buffer, containing 50 mM Tris-HCl (pH = 7.4), 2 mM EGTA, 2 mM EDTA, 2 mM PMSF, 5 mM NaF and 2 mM Beta-Glycerophosphate was prepared. The lysis buffer was supplemented with PhosSTOP (1 tablet per 10 ml), as well as 20 µl of liquid phosphatase inhibitor. Brain sections were weighed, being kept in liquid nitrogen before and after. Depending on sample weight, the appropriate volume of lysis buffer was added, using 1 ml lysis buffer per 100 mg of brain tissue. Tissue was then being disrupted and homogenized using a homogenator and the solution was clarified by centrifugation for 5 min at 4°C and 14000 rpm. The supernatant was used for mass spectrometry.

Mass spectrometry

Mass spectrometry was performed by Marc Sylvester at the Mass Spectrometry Core Facility of the University of Bonn, as described in the following. All chemicals used were from Sigma unless noted otherwise.

Acetone precipitation

Protein lysates were brought to a volume of 200 µl with water and mixed with 800 µl chilled acetone. After 1 h at -20°C proteins were sedimented by centrifugation for 15 min at 14,000 rcf. The supernatant was discarded und pellets air-dried. Pellets were dissolved in 50 µl lysis buffer (iST-NHS kit, Preomics GmbH, Martinsried, Germany). An aliquot was used for a BCA protein assay.

Proteolysis, peptide labeling, and fractionation

Lysate containing 30 µg protein was mixed with 50 µl of DIGEST solution (iST-NHS kit) to digest proteins (3 h, 37 °C). 0.4 mg of TMT10plex isobaric Mass Tag Labeling reagent were added to each sample and incubated at room temperature for 1 h. 10 µl 5 % hydroxylamine were used to quench the reaction. The preparation procedure was continued according to the iST-NHS kit instructions. Pooled peptides were dried in a vacuum concentrator, dissolved in 5 % ammonium formate (pH=10) and fractionated by reversed phase chromatography at elevated pH with a Reprosil 100 C18 column (3 µm 125 x 4 mm, Dr. Maisch GmbH, Ammerbuch-Entringen, Germany). 60 fractions were combined into 12 pools per fractionation and dried in a vacuum concentrator.

LC-MS measurements

Before measurement, peptides were re-dissolved in 10 µL 0.1 % formic acid (FA) and separated on a Dionex Ultimate 3000 RSLC nano HPLC system (Dionex GmbH, Idstein, Germany). The autosampler was operated in µl-pickup mode. 1 µl was injected onto a C18 analytical column (self-packed 300 mm length, 75 µm inner diameter, ReproSil-Pur 120 C18-AQ, 1.9 µm, Dr. Maisch). Peptides were separated during a linear gradient from 5 % to 35 % solvent B (90 % acetonitrile, 0.1 % FA) at 300 nl/min. The nanoHPLC was coupled online to an Orbitrap Fusion Lumos mass spectrometer (ThermoFisher Scientific, Bremen, Germany).

Gradient length was 120 min. Peptide ions between 330 and 1500 m/z were scanned in the Orbitrap detector every 3.5 s with a resolution of 120,000 (maximum fill time 50 ms, AGC target 100 %). Polysiloxane (445.12002 Da) was used for internal calibration (typical mass error ≤1.5 ppm). In a top-speed method peptides were subjected to collision induced dissociation for identification (CID: 0.7 Da isolation, normalized energy 30 %) and fragments analyzed in the linear ion trap with target 10,000 and maximum fill time 35 ms, rapid mode. Fragmented peptide ions were excluded from repeat analysis for 25 s. Top 8 fragment ions were chosen for synchronous precursor selection and fragmented with higher energy CID (HCD: 3 Da MS2 isolation, 65 % collision energy) for detection of reporter ions in the Orbitrap analyzer (resolution 50,000, maximum fill time 86 ms, target 100,000).

Data analysis

Raw data processing and database search were performed with Proteome Discoverer software 2.5.0.400 (Thermo Fisher Scientific). Peptide identification was done with an in-house Mascot server version 2.6.1 (Matrix Science Ltd, London, UK). MS data were searched against *mus musculus* sequences from the SwissProt database including isoforms (access date: 2021/03; 17089+8277 murine sequences) and contaminants database (cRAP) (Mellacheruvu et al., 2013). Precursor Ion m/z tolerance was 10 ppm, fragment ion tolerance 0.5 Da (CID). Tryptic peptides with up to two missed cleavages were searched. C6H11NO-modification of cysteines (delta mass of 113.08406) and TMT on N-termini and lysines were set as static modifications. Oxidation was allowed as

dynamic modification of methionine. Mascot results were evaluated by the Percolator algorithm version 3.02.1 (The et al., 2016) as implemented in Proteome Discoverer. Spectra with identifications above 1 % q-value were sent to a second round of database search with semi tryptic enzyme specificity (one missed cleavage allowed). Protein N-terminal acetylation, methionine oxidation, TMT, and cysteine alkylation were then set as dynamic modifications. Actual FDR values were 0.6 % (peptide spectrum matches) and 1.0 % (peptides and proteins). Reporter ion intensities (most confident centroid) were extracted from the MS3 level, with SPS mass match > 65 %.

2.4 Bioinformatic analysis

Transcriptomics

After trimming of the Illumina Universal Adapter with cutadapt (Martin, 2011) reads have been aligned to the mouse genome (GRCm38) with STAR (Dobin et al., 2013). featureCounts (Liao et al., 2014) was used to assign reads to genes as defined by Ensembl. A read is counted if the read is uniquely mapped, the strand matches and overlaps with only one gene, i.e. the read is non-ambiguously assigned to a single gene. Statistical analysis was performed in the R environment (R Core Team, 2019) with the Bioconductor package DESeq2 (Huber et al., 2015; Love et al., 2014). The Benjamini-Hochberg method was used to calculate multiple testing adjusted p-values. An FDR threshold of 5 % was chosen to identify differentially expressed genes.

Bioinformatic analysis of RNA Seq data was performed by Andreas Buness at the Core Unit of Bioinformatic Analysis (CUBA) of the University of Bonn.

GO analysis

To interpret the biological function of the differentially expressed genes, Gene Ontology (GO) Enrichment analysis was performed using the genomic database Gorilla (Eden et al., 2009) (access date: 2021/08). All significantly differentially expressed genes were put as the target list, while all detected genes served as the background list. FDR corrected p-values of 0.05 were considered significant.

Proteomics

The statistical analysis of the peptide-spectrum match (PSM) level data was carried out in R environment (R version 4.1) (R Core Team, 2021) using an in-house developed workflow. Non-unique peptides and single-shot proteins (proteins identified/quantified by only one peptide) were filtered-out prior to the statistical analysis. From all available fractions, only those with the least number of missing values per PSM and maximum average intensity across all TMT channels were selected. The PSM-level data were then variance-stabilized and transformed using the VSN package (Huber et al., 2015) and then aggregated to protein-level by applying the Tukey's median polish method. The statistical analysis was performed using the R package limma (Ritchie et al., 2015). For each statistical contrast the resulting P-values were adjusted for multiple testing and the false discovery rates (FDR) were calculated by the Benjamini-Hochberg method. An FDR threshold of 5 % was chosen to identify differentially expressed proteins, and a threshold of 20 % for possible candidate proteins. The PCA plot was generated using the FactoMineR (Lê et al., 2008) package.

Bioinformatic analysis of mass spectrometry data was performed by Farhad Shakeri at the Core Unit of Bioinformatic Analysis (CUBA) of the University of Bonn.

2.5 Cell culture

2.5.1 Human embryonic kidney (HEK293T) cells

HEK293T cells were used for the production of viral particles in this study. HEK293T cells were cultured in T75 flasks or on 10 cm petri dishes up to 80 % confluency in Dulbecco's modifed eagle medium (DMEM, Cat.No.: 41966, Life technologies, Van Allen, USA) containing 10 % FCS and 1 % Penicillin/Streptavidin. For lentiviral production, HEK293T cells were cultured in DMEM + Glutamax (Cat. No. 32430, Life Technologies) and 10 % FCS, supplemented with 300 µg/ml G418 (Invitrogen, San Diego, USA) to select cells for SV40 largeT antigen (expressed on plasmid with Neo-Cassette). This is important to yield a high virus titer. Before transfection, these cells were seeded on 10 cm dishes and G418 was removed, to avoid toxicity for cells without Neo-cassette (i.e. neurons) in later experiments. When reaching 80 % confluency in flasks, HEK2913T cells were passaged

by trypsination. For this, washed cells were incubated with Trypsin-EDTA (Thermo Fisher) for 5 min to digest extracellular parts of adhesion proteins. Afterwards, cells were seeded in a ratio of 1:6 in a new flask. For production of lenti-viral particles and recombinant adenovirus-associated viral particles (AAV), HEK293T cells were transfected with GeneJet transfection reagent (Signagen, Rockville, USA) or calcium-phosphate, respectively (see sections 2.6.1 and 2.6.2).

2.5.2 Primary neuron culture

Primary cortical neurons were isolated and cultured by Sabine Opitz. Isolation of neurons from mouse brains was described before (Woitecki et al., 2016) as summarized in the following: primary neurons were isolated from mouse embryos at E16 – E19. Embryos were decapitated in ice-cold HBSS (Cat. No. 14170, Life Technology) supplemented with 20 % FCS. The meninges were removed from the brain and cortices were isolated. Tissue was then dissected and washed 3 times in HBSS (with 20 % FCS), followed by incubation with 2.5 % trypsin (Thermo Fisher) at 37 °C for 20 min. After washing 3 times in HBSS (with 20 % FCS), 200 µl DnaseI (Sigma-Aldrich, Taufkirchen) was added and tissue was further dissociated by tituration until the solution was homogenous. Finally, pre-warmed BME (Cat. No. 41010, Life Technology) was added, cells were counted and plated on poly-D-Lysine (Sigma-Aldrich) coated coverslips, with 25000 – 30000 cells seeded on each coverslip. After 24 h medium was replaced to fresh BME and cells were kept in the same medium until use in experiments.

2.6 Virus preparation

2.6.1 Lenti-viral particles

Lenti-viral particles were produced and isolated by Anna Dorißen and Katrin Krischer, as described before (van Loo et al., 2019). Briefly, 3 x 10^6 HEK293T cells were seeded on a 10 cm cell culture dish and transfected 24 h later with GenJet transfection. Per dish, a transfection mix containing 3 ml DMEM + Glutamax, 40 µl GeneJet transfection reagent, 7.5 µg packaging plasmid (psPax2, Addgene), 5 µg VSV-G expressing envelope plasmid

(pMD2.G, Addgene) and 4 µg plasmid of interest (i.e. pLenti-NLS-Cre-EGFP and pLenti-NLS-ΔCre-EGFP) was added to the cells. Transfection medium was replaced after 12 h with DMEM containing Glutamax (Invitrogen), supplemented with 10 % FBS. After 72 h of incubation, the supernatant was collected and filtered through 0.45 µm PVDF membrane filters (GE Healthcare, Little Chalfont, UK) to remove cell debris and other aggregates. For virus purification, the filtered supernatant was layered on top of OptiPrep density gradient medium (Sigma-Aldrich) and centrifuged at 24000 rpm for 2 h at 4 °C using an SW-Ti32 swinging bucket (Beckman Coulter, Brea, USA). The upper layer was discarded. The Opti-Prep-Layer, containing the viral particles at its upper boundary, was mixed with TBS-5 buffer (containing in mM: 50 Tris-HCl, 130 NaCl, 10 KCl, 5 $MgCl_2$). Thereafter, viral particles were pelleted by centrifugation at 24,000 rpm for 2 h at 4 °C and resuspended in TBS-5 buffer. Lentiviral particles were aliquoted and stored at −80 °C until use.

2.6.2 Recombinant Adenovirus-associated viral particles (rAAV)

For production of rAAV viral crude extract and purified rAAV, HEK293T cells were transfected as described previously (van Loo et al., 2012). Briefly, 1.5 x10^6 HEK293T cells were plated on a 10 cm dish in Dulbecco's Modified Eagle's Medium (DMEM) and transfected 24 h later, using the calcium phosphate method. In addition to the adeno-associated virus (AAV) plasmid of interest, helper plasmids encoding rep and cap genes (pRV1 and pH21) and adenoviral helper pFΔ6 (Stratagene, La Jolla, USA) were co-transfected. 3-4 h prior to transfection, medium was changed to Iscove's Modified Dulbecco's Medium (IMDM) with 5 % Fetal Bovine Serum (FBS). A transfection mix (containing: 1 ml ddH2O, 145 µl CaCl2 2.5 M, 5.5 µg AAV plasmid of interest, 2.64 µg pRV1, 2.64 µg pH21, 11µg pFΔ6) was prepared and 1.2 ml 2xHeBS was added dropwise while vortexing at 1400 rpm, to allow the formation of a CaPO4 precipitate containing the DNA. After continuing vortexing for 30 s and incubating for 2 min, the mixture was added to the culture medium. After 24 h, culture medium was replaced with fresh DMEM, containing 5 % FBS and 1 % Penicillin/Streptomycin.

To prepare rAAV viral crude extract, cells were harvested 48 – 72 h after transfection by scraping them from the culture dish into a fresh tube and subjected to three cycles of

freezing at -80 °C and thawing at 37 °C. The suspension was centrifuged for 1 min at 10.000 rpm to clear from cell debris. After that, the supernatant could be collected and used as viral crude extract. To generate purified rAAV, cells were harvested and pelleted by centrifugation. Virus cell pellets were then lysed in lysis buffer (50 ml PBS, 50 mM, 150 mM NaCl, 1 % Triton-X 100, 1 protease inhibitor tablet, pH = 7.4) supplemented with 0.5 % sodium deoxycholate (Sigma-Aldrich) and 50 units/ml Benzonase endonuclease (Sigma-Aldrich). HiTrapTM heparin columns (GE Healthcare) were used to purify rAAV viral particles from the cell lysate. The suspension was concentrated using Amicon ultra centrifugal filters (Millipore) to a final stock volume of 500 µl. Coomassie blue staining of SDS-polyacrylamide gels was performed to validate virus purity. Purified rAAV were produced by Anna Dorißen and Katrin Krischer. Both viral crude extract and purified viruses were stored at 4 °C until use.

2.6.3 Assessment of cell-type specificity and transduction efficiency

Cell-type specificity and transduction efficiency of the viruses were validated with immunocytochemistry as described in Section 2.7. Neurons were labeled with an anti-NeuN antibody (abcam, Cambridge, UK; diluted 1:500) while GABAergic neurons were labeled with anti-GAD67 antibody (Merck-Millipore, Burlington, USA; diluted 1:1000). Glutamatergic neurons were defined as GAD67-negative, but NeuN-positive cells. For the Dlx-Cre/-ΔCre viruses transduction efficiency was defined as GAD+ transduced/total GAD+, while cell-type specificity was counted as GAD+ transduced/total transduced. In contrast, for the VGLUT2-Cre/-ΔCre viruses transduction efficiency was defined as GAD– transduced/total GAD– and cell-type specificity as GAD– transduced/total transduced neurons.

2.7 Immunocytochemistry

Primary cortical neurons were fixed with 4% PFA for 10 min at room temperature while shaking. After washing the cells three times with PBS, they were permeabilized with 0.3% Triton X-100 (Merck, Darmstadt) in PBS for 10 min at room temperature. Following the

permeabilization step, cells were incubated with a solution containing primary antibodies in 0.1% Triton X-100 PBS overnight at 4°C. After three washes with PBS, secondary antibodies labeled with a fluorochrome and diluted in 0.1% Triton X-100 PBS were applied and incubated for 1 h at room temperature, protected from light. Finally, cells were washed three times with PBS and mounted with Mowiol (Roth, Karlsruhe).

2.8 Cell viability assay

Primary cortical neurons were washed one time with dPBS to remove residues of medium and then incubated with 500 µl of 50 µg/ml Propidium iodide for 5 min. Incubation was performed in the dark to reduce bleaching and on ice to reduce unspecific cytosolic staining. Then cells were washed two times with dPBS and fixed with 4% PFA for 10 min at room temperature while shaking. After washing the cells three times with PBS, they were permeabilized with 0.3 % Triton X-100 in PBS for 10 min at room temperature. Following the permeabilization step, cells were incubated with a solution containing DAPI (Life Technologies) in 0.1 % Triton X-100 PBS for 1 h at room temperature, protected from light. Finally, cells were washed three times with PBS and mounted with Mowiol. Non-viable cells were identified by nuclear red fluorescent propidium iodide staining. Percentage of viable cells was counted as DAPI-labeled, propidium-iodide-negative cells out of all DAPI-labeled cells.

2.9 Multi-electrode arrays (MEA)

Multielectrode arrays (MEA) are extracellular, non-invasive recordings of whole neuronal networks. Multiple embedded electrodes with neurons growing and forming connections around them enable the recording of neuronal activity on the network level. Furthermore, with this technique cells are not being damaged by recording and enable long-term investigations of the same cells and monitoring of network development.

2.9.1 Plates and seeding

All MEA recordings were acquired with a Maestro Edge multi-well MEA recorder (Axion Biosystems, Atlanta, USA).

To record spontaneous neuronal network activity, primary cortical neurons were seeded on an Axion Biosystems Cytoview MEA plate, that consisted of 24 individual wells. Each well had 16 recording electrodes embedded in the bottom surface, allowing recordings of neuronal network activity (Figure 2.1 B). Electrodes were 50 µm in diameter and spaced 350 µm apart.

Plate preparing and neuron seeding was performed by Sabine Opitz. The electrode area at the bottom of each well was coated with 5 µl Poly-D-Lysin and left to dry for 30 min. Then, wells were washed 2 x with sterile ddH_2O. Primary cortical neurons were isolated as described in Section 2.5.2 and counted. A droplet containing the appropriate number of cells was placed on the electrode area and plates were subsequently kept in the incubator for 1 h, allowing the cells to distribute and settle down. Afterwards, wells were filled up with 600 µl of BME. Medium was changed to fresh BME after 24 h and cells were kept in the same medium until use in experiments.

2.9.2 Recording

After a 10 min acclimatization period in the MEA recorder, neurons were recorded for 10 min, while conditions were maintained at a constant level of 37 °C and 5 % CO_2. A single electrode records continuous voltage data from multiple neurons growing in proximity (Figure 2.1 C). Continuous voltage data was acquired with a sampling frequency of 12.5 kHz, a Gain of 1000x and a bandwidth of 200 – 4000 Hz. Additionally, butterworth filters were applied to the data while recording to reduce noise, using 3 kHz Kaiser Window as low pass filter and 200 Hz IIR as high pass filter. Spontaneously generated action potentials (spikes) were detected when the recorded voltage exceeded a certain threshold, here set at 6 SD of the root mean square of the background voltage (Figure 2.1 D). Data was further analyzed using the Axis Navigator Software (Axion Biosystems, version 2.0.2.5), unless noted otherwise.

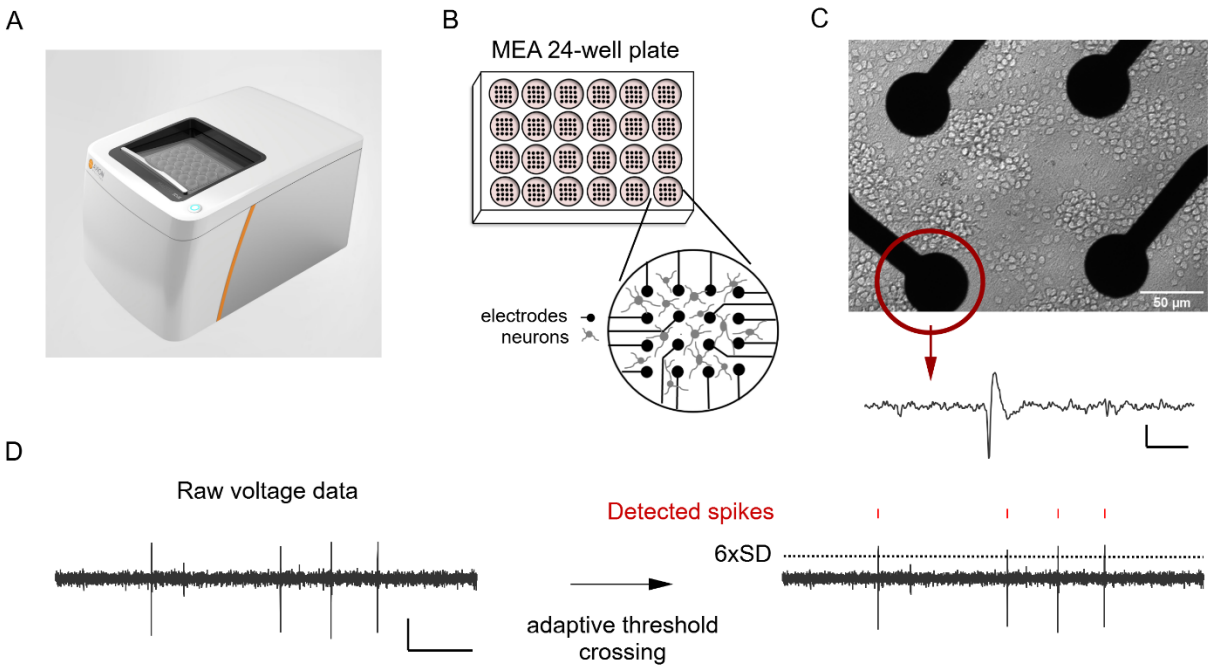

Figure 2.1: Extracellular long-term recordings of in vitro neuronal networks with MEA. (A) Maestro Edge MEA recorder by Axion Biosystems. **(B)** Schematic image of 24-well MEA CytoView plate with each well containing 16 recording electrodes (black dots), 50 µm in diameter and spaced 350 µm apart. **(C)** Representative image of primary cortical neurons growing on MEA plate on DIV14 with example trace of recorded action potential. Scale bar 10 µV, 5 ms **(D)** Spikes are detected from raw voltage data through adaptive threshold crossing, using 6xSD of background noise. Detection threshold indicated as dashed line. Detected spikes indicated as red ticks. Scale bar 10 µV, 200 ms.

2.9.3 Analysis

Detected spikes on one electrode were counted and divided by the recording time to assess the mean firing rate (spikes/s) per electrode. For calculation of the well-wide mean firing rate, electrode mean firing rate values were averaged. Silent or inactive electrodes were excluded from the analysis, with an electrode considered as active at ≥ 5 spikes/min. This also serves for all parameters discussed in the following.

Apart from spiking, different forms of neuronal activity can be observed with MEA (Figure 2.2). A common type of activity is bursting, or burst firing, where neurons fire at a high frequency for a short time interval, followed by a period of quiescence (Figure 2.2 A).

Bursting on one electrode was defined by a minimum number of 5 spikes, spaced apart by a max. inter-spike-interval (ISI) of 100 ms. The total number of bursts in a recording was divided by the recording time to calculate the burst frequency (bursts/min). Additionally, other burst features can be characterized (Figure 2.2 B). Burst duration was measured as the time from first to last spike within an average burst. An inter-burst-interval (IBI) was calculated as the average time from last spike of a burst to the first spike of the following burst. Burst irregularity was assessed as the coefficient of variation of the average IBI.

Inter-spike-intervals (ISIs) were calculated as the average time between two spikes occurring on one electrode (Figure 2.2 B). The distribution of inter-spike-intervals (ISI) conveys information about the firing pattern, e.g., if spikes occur randomly and isolated or are mostly organized in bursts. This parameter and the corresponding histograms shown in this study were generated with Igor Pro, analysis was established by Hyuntae Kim.

Bursting can not only be observed on the single electrode level but also as simultaneous bursting on multiple electrodes in a synchronized manner, called network bursting (Figure 2.2 B). Network bursts were defined by a minimum number of 50 spikes, spaced apart by a max. ISI of 100 ms, with at least 35% of the electrodes participating in the event. The total number of network bursts in a recording was divided by the recording time to calculate the network burst frequency (network bursts/min). Inter-network-burst-intervals (INBI) were calculated as the average time from last spike of a network burst to the first spike of the following one, and the INBI coefficient of variation was used as a measure for network burst irregularity. Network burst percentage quantifies the number of spikes organized in network bursts out of total spikes.

Coordinated or simultaneous firing between electrodes throughout the well is referred to as the network's synchronicity. This parameter was quantified using a cross-correlogram (Figure 2.2 C). The cross-correlogram assesses the probable time lag of a spike occurring on one electrode relative to a given spike on another electrode. This probability is calculated from the time lags of all spikes occurring on the two electrodes. For a well-wide assessment of the network's synchronicity and not only between two electrodes, a pooled cross-correlogram is computed, pooling all possible pairs of combinations of electrodes. The Axis Navigator software uses frequency domain methods as constituted by Halliday,

Rosenberg, Breeze & Conway (Halliday et al., 2006) to compute pooled cross-correlograms. To reduce the effect of high firing rates that would artificially increase synchronicity, autocorrelations of electrodes were being removed by normalization of each electrode's activity to itself, resulting in a normalized cross-correlogram.

To quantify each well's synchronicity, the area under the normalized cross-correlogram around zero was being measured. For this, a synchronicity time window of 20 ms was chosen.

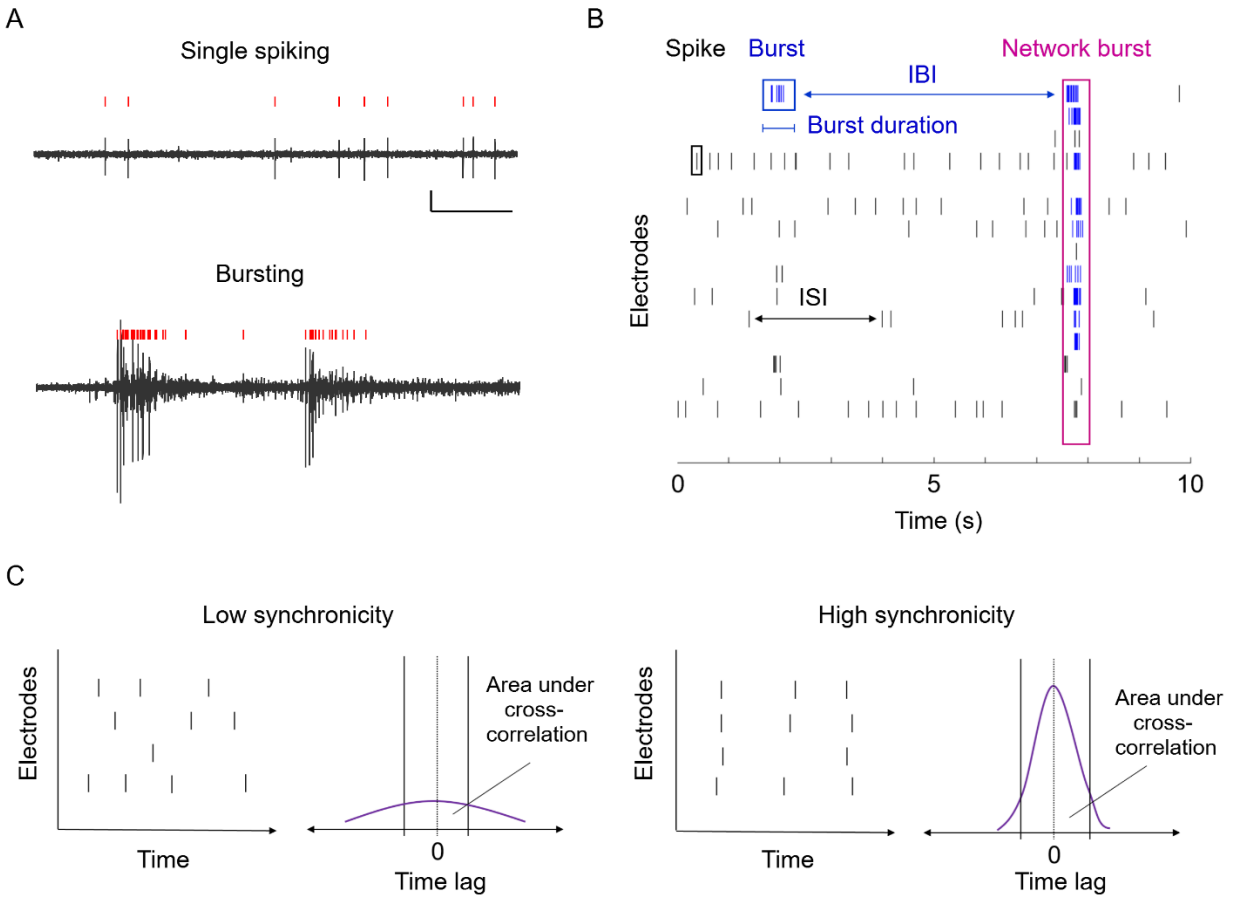

Figure 2.2: Characterizing different forms of neuronal activity on MEA. (A) Example traces of random spiking activity *(upper panel)* and spikes organized in bursts *(lower panel)*. Detected spikes are indicated as red ticks. Scale bar: 20 µV, 500 ms. **(B)** Spike raster plot of a 10 s interval, illustrating the degree and pattern of neuronal activity. Each row depicts one electrode in a representative MEA well, with each tick representing one spike. IBI = inter-burst-interval, ISI = inter-spike-interval. **(C)** Schematic image of the area under cross-correlation as a measure for synchronicity. Activity with low synchronicity exhibits a bigger time lag between spikes occurring on different electrodes, resulting in a smaller area under cross-correlation in the defined time

window around zero. Highly synchronous activity shows less time lag, therefore the area under cross-correlation is bigger in the defined time window around zero.

For the MEA experiments shown and discussed in this study, the means of all wells per group were calculated and used for analysis. Groups consisted of at least three wells per condition and were assigned randomly. Representative well-wide raster plots were created using the Neural Metric Tool software (Axion Biosystems, version 2.5.1).

2.9.4 Culture density

For assessment of optimal recording conditions and influences of culture density on neuronal activity, different densities were tested on MEA. Cells were seeded at 2500, 4000, 6000, 10000, 16000, 20000 and 40000 cells per well as described in Section 1.9.1, on an area of approximately 5 mm², resulting in seeding densities of approximately 500, 800, 1200, 2000, 3200, 4000 and 8000 cells/mm². Electrophysiological activity was recorded from DIV14 to DIV18.

To assess if cell densities are sufficient to form neuronal networks and achieve reliable responses on MEA, the percentage of responding electrodes within a well was measured for each density. A responding electrode was defined as firing ≥ 5 spikes/min, consistently from DIV16 – DIV18.

2.9.5 Homeostatic plasticity

TTX

To examine if homeostatic plasticity could be chemically induced at a culture density of 2000 cells/mm², primary neurons were being silenced with the voltage-gated sodium channel blocker TTX (Tocris, Bristol, UK). Recordings were performed on DIV16 and DIV18.

TTX was prediluted in sterile water. Experiments were performed at DIV16 and were started with 10 min baseline recordings, before TTX was added to the culture medium at

a concentration of 1 µM. Control groups were sham treated with the same volume of sterile water. After an incubation period of 48 h, cells were washed four times with warm BME to remove the reagents, followed by a 15-min resting period in the incubator to reduce mechanical stress effects of the washout. Subsequently, 10 min washout recordings were performed to assess possible plasticity effects.

The analysis consisted of two steps. First, activities of TTX and control wells after washout were expressed as a percentage of their baseline activity (percentage-of-baseline, %BL). Percentage-of-baseline values per well were then averaged for each group. The post-silencing effect of TTX was then assessed by normalizing the averaged percentage-of-baseline of the TTX group to the averaged percentage-of-baseline of the control group. In this way, a possible TTX effect can be depicted, while reducing effects of different baseline activities as well as maturation effects between DIVs.

TTX experiments with WT and RIM3 cKO at 8000 cells/mm² were performed on DIV12 (baseline + TTX application) and DIV14 (washout).

Gabazine

Another approach to test for homeostatic plasticity is the treatment of primary neurons with the $GABA_A$ receptor antagonist Gabazine. Recordings were performed on DIV17 and DIV18.

Gabazine was prediluted in sterile water. Experiments were performed at DIV17 and started with 10 min baseline recordings, before Gabazine was added to the culture medium at a concentration of 1 µM. Control groups were sham treated with the same amount of sterile water. 20 min after application 10 min recordings were obtained to assess immediate effects of Gabazine. Recordings were repeated after 24 h for long-term effects. Afterwards cells were washed four times with warm BME to remove the reagents, followed by a 15-min resting period in the incubator to reduce stress effects of the washout. Subsequently, 10-min washout recordings were performed to assess possible plasticity effects.

For analysis, the activity of each well at every treatment timepoint (20 min, 24 h, washout) was normalized to its baseline, for both Gabazine and control treatment. Resulting values per well were then averaged for each group, and different treatment timepoints were compared between Gabazine and control.

2.9.6 Ubiquitous and cell-type specific RIM3 cKO experiments

To observe the effects of RIM3 deficiency on MEA, cortical RIM3$^{flox/flox}$ primary neurons were treated on DIV4-5 with 1µl pLenti-NLS-Cre-EGFP or pLenti-NLS-ΔCre-EGFP viruses to achieve ubiquitous conditional RIM3 KO (cKO) and corresponding wildtype cells (WT), respectively. MEA experiments with ubiquitous RIM3 cKO were performed with culture densities of 2000 cells/mm² and 8000 cells/mm². To induce RIM3 deficiency exclusively in glutamatergic neurons, cells were instead treated with 1 µl AAV-VGLUT2-mCherry-Cre and 2 µl AAV-VGLUT2-mCherry-ΔCre viruses for cKO and WT, respectively. For RIM3 cKO and WT in GABAergic neurons, cells were treated with 1 µl AAV-mDlx-Cherry-2A-Cre and 2µl AAV-mDlx-Cherry-2A-ΔCre viral crudes, respectively. MEA experiments with cell-type specific cKO were performed with a culture density of 2000 cells/mm².

Recordings were performed on DIV14 as an earlier stage of development, as well as in a mature state from DIV18 to DIV20. The cKO group means were normalized to WT group means for each time point.

2.10 Statistics and data presentation

Statistical analysis and graphs were performed with Graphpad Prism 8.0 (Graphpad Software Inc.; La Jolla, USA) and Igor Pro 7.0 (Wavemetrics, Lake Oswega, USA), respectively. Statistical tests were used as indicated. Differences between conditions were assumed significant at p-values < 0.05. If not stated otherwise, results are plotted as means ± SEM and p-values were indicated as * $p < 0.05$.

3 Results

3.1 RIM3 deficiency influences cortical and thalamic gene expression

The transcriptome of a cell or certain brain area assesses the total amount of RNA transcripts and offers valuable information about gene activity and regulation. As a first step in elucidating the function of RIM3, we wanted to investigate how RIM3 deletion affected gene expression in the thalamus and cortex, as these brain areas exhibit the highest RIM3 abundance. Characterizing these expression profiles can give important insights into possible processes and pathways RIM3 might be involved in. To this end, RNA Seq and subsequent bioinformatic analysis were performed with thalami and cortices of RIM3 WT and constitutive KO mice. Differentially expressed genes (DEGs) were defined as up- or down-regulated genes in KO vs. WT with an adjusted p-value (FDR) < 0.05.

3.1.1 RIM3 KO leads to differential expression of many synapse-related genes in the thalamus

RNA-seq analysis found 17,107 genes to be expressed in the thalami of RIM3 KO and WT mice. Of these, the expression of a total of 1028 genes was determined to be changed significantly (Figure 3.1 A), including 375 up-regulated genes and 653 down-regulated genes (Figure 3.1 B).

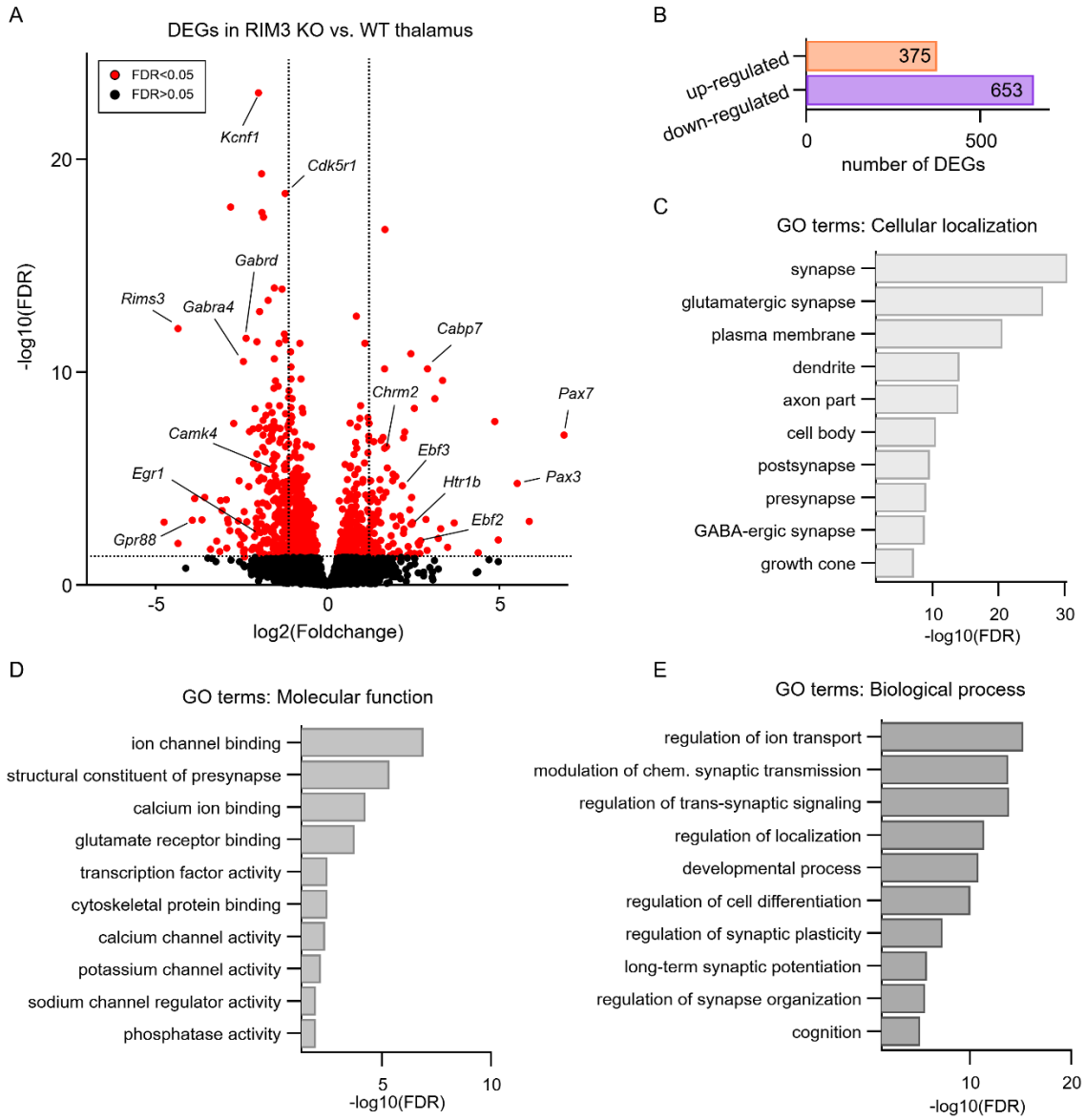

Figure 3.1: Differentially expressed genes in RIM3 KO vs. WT in the thalamus. **(A**) Volcano plot showing differentially expressed genes (DEGs) in RIM3 KO (n=5) compared to WT (n=4). X-axis represents Foldchange (FC) of gene expression levels in RIM3 KO vs. WT, shown as log2 Foldchange. Y-axis represents level of significance, shown as -log10 adjusted p-value (FDR). Each gene is color based on the -log10(FDR). Red dots represent FDR <0.05, black dots represent FDR > 0.05. Interesting candidate genes among the most up-/down-regulated DEGs were marked and named. **(B)** A total of 1028 DEGs was identified, including 365 up-regulated (orange) and 653 down-regulated (violet) genes. **(C-E)** GO analysis: significantly enriched GO-terms in the categories cellular localization **(C)**, molecular function **(D)** and biological process **(E).** X-axis represents GO-terms.

Among the DEGs with the strongest downregulation, there were several interesting candidates involved in the regulation of neuronal excitability. Two genes that showed a strong down-regulation were *Gabrd* (log2FC = - 2.4), encoding the δ-subunit of $GABA_A$-receptors, and *Gabra4* (log2FC = - 2.4), encoding the α4-subunit. While the α4-subunit can be part of synaptic as well as extrasynaptic $GABA_A$-receptors (Smith et al., 2007), $GABA_A$ receptors containing the δ-subunit are found to be exclusively peri- or extrasynaptic (Arslan, 2021). In contrast to synaptic $GABA_A$ receptors that exert phasic inhibition, they respond to much lower GABA concentrations, resulting in a persistent, tonic inhibition that is important for regulating neuronal excitability (Lee and Maguire, 2013; Whissell et al., 2015). Other downregulated genes with a major influence on membrane excitability and action potential dynamics were those of several voltage-dependent potassium channel subunits, including *Kcnf1* (logFC = - 2.0), *Kcne4* (log2FC = - 2.0), *Kcnab* (log2FC = - 1.6) and *Kcnc2* (log2FC = - 1.5). Additionally, we found a strong downregulation of the transcriptional regulator *Egr1* (log2FC = - 2.1), which is activated by changes in neuronal activity and regulates neuronal excitability through the subsequent induction of LTP (Duclot and Kabbaj, 2017). Two other downregulated genes involved in similar processes were *Bdnf* (log2FC = - 1.3) (Leal et al., 2014; Panja and Bramham, 2014) and *Camk4* (log2FC = - 1.6) (Kasahara et al., 2001; Tokuda et al., 1997).

Furthermore, we found several candidates involved in neuronal development among the DEGs with the highest differential expression. The gene exhibiting the strongest upregulation after RIM3 deletion was *Pax7* (log2FC = 6.9), a transcription factor which plays an important role in neuronal differentiation and regionalization (Fedtsova et al., 2008; Lin et al., 2016), together with its likewise upregulated paralogue *Pax3* (log2FC = 5.5) (Gard et al., 2017; Huo et al., 2021). Other DEGs associated with neuronal development that were either up- or downregulated, were *Ebf2* (log2FC = 2.6), *Ebf3* (log2FC = 2.2), *Socs2* (log2FC = - 1.9), *Cdk5r1* (log2FC = - 1.2) and *Gpr88* (log2FC = - 3.7) which are involved in neuronal migration, differentiation, morphogenesis, neurite outgrowth, axon targeting and network connectivity (Arefin et al., 2017; Basrai et al., 2017; Chae et al., 1997; Chuang et al., 2012; Dhavan and Tsai, 2001; Goldshmit et al., 2004; ben Hamida et al., 2018; Iwai et al., 2018).

Additionally, we observed a significant upregulation of important regulators of acetylcholine and monoamine signaling. *Chrm2* (log2FC = 1.7) encodes the presynaptic mACh autoreceptor M_2 which exerts feedback inhibition on acetylcholine release, while *Slc29a4* (log2FC = 1.4) encodes the plasma membrane monoamine transporter PMAT, a protein responsible for removing monoamines from the synaptic cleft (Adamsen et al., 2014; Jeon et al., 2015; Volpicelli and Levey, 2004). *Htr1b* (log2FC = 2.5) encodes the serotonin receptor 1B, which can exert excitatory or inhibitory functions, depending on the neuronal subtype, and is associated with a variety of neuropsychiatric conditions (Drago et al., 2010; Moret and Briley, 2000).

GO analysis

To give further insight into the functions and processes involving RIM3, thalamic DEGs were subjected to a Gene ontology (GO) analysis (Figure 3.1 C-E).

A GO analysis in the cellular localization category (Figure 3.1 C) revealed that DEGs showed a significant association with the GO term synapse (GO:0045202). More specifically, RIM3 seemed to affect genes which are active in glutamatergic synapses (GO:0098978), and colocalize to the plasma membrane (GO:0005886), the postsynapse (GO:0098794) and presynapse (GO:0098793), but also the cell body (GO:0044297). To a lesser extent, DEGs were also associated with GABAergic synapses (GO:0098982).

Regarding the molecular function of the DEGs (Figure 3.1 D), we found a significant association with the terms ion channel binding (GO:0044325) and structural constituent of the presynapse (GO:0099181). Apart from additional functions in different ion channels, it became apparent that many DEGs seem to function as transcription factors (GO:0098531).

In the category biological process (Figure 3.1 E), thalamic DEGs showed a highly significant association with synaptic processes. The GO terms regulation of ion transport (GO:0043269), modulation of chemical synaptic transmission (GO:0050804) and regulation of trans-synaptic signaling (GO:0099177) showed highly significant enrichment. Additionally, RIM3 seems to affect genes that are involved in the regulation of synaptic plasticity (GO:0048167), long-term synaptic potentiation (GO:0060291) and synapse

organization (GO:0050807). Furthermore, DEGs seemed to play a role in developmental processes (GO:0032502).

Expression levels of pre- and postsynaptic components

Since the large RIM isoforms RIM1/2 are well-known to interact with multiple presynaptic proteins (Mittelstaedt et al., 2010) and the GO analysis of RIM3 KO induced DEGs indicated synaptic down-stream targets (Figure 3.1 C-E), we were particularly interested in how RIM3 KO affected gene expression levels of presynaptic components, including scaffolding proteins, synaptic vesicle (SV) release machinery, cell adhesion molecules and Ca^{2+} channels (Figure 3.1 A-B). Furthermore, the GO analysis pointed to an additional role of RIM3 in the postsynapse. Therefore, we also studied gene expression levels of important postsynaptic scaffolding and cell adhesion molecules (Figure 3.2 C) as well as glutamate and GABA receptor subtypes (Figure 3.2 D-E).

In the presynaptic compartment (Figure 3.2 A), we observed a reduced expression of several genes: apart from the downregulation of the large RIM isoform encoding genes *Rims1* and *Rims2*, we found *Ppfia2, Bsn, Pclo, Erc2, Syt-1, Vamp2, Snap25* and *Nrxn-1* to be significantly downregulated, coding for the AZ proteins Liprin-α2, Bassoon, Piccolo, ELKS2 and Synaptotagmin-1, the SNARE-proteins Synaptobrevin and SNAP25, as well as the presynaptic cell adhesion molecule Neurexin-1, respectively. Analyzing gene expression levels of voltage-gated calcium channels (VGCC) (Figure 3.2 B) showed downregulation (*Cacna1c, Cacna2d1*, *Cacna2d3, Cacn4b* and *Cacng5)* as well as upregulation (*Cacna1h*, *Cacna2d2)* of several subunits.

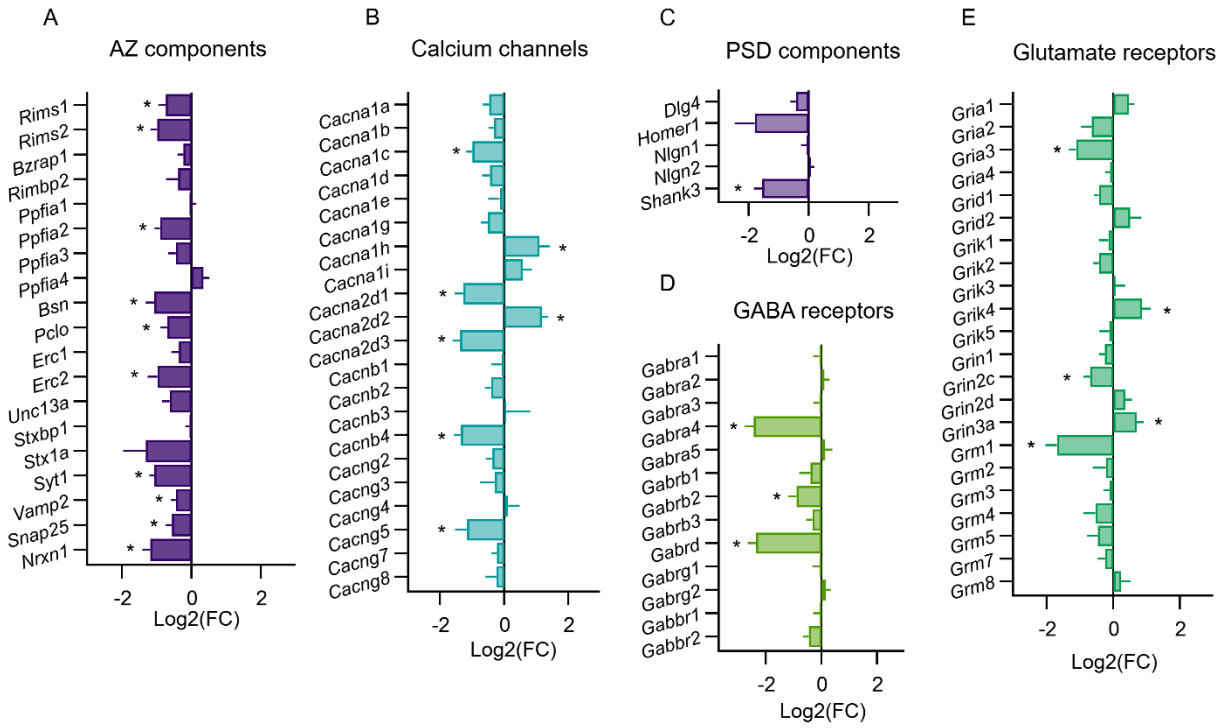

Figure 3.2: RIM3 KO induces differential expression of several synapse-related genes in the thalamus. (A-E) Relative gene expression levels of different presynaptic active zone components **(A)** and calcium channels **(B)**, postsynaptic density components **(C)**, GABA receptors **(D)** and glutamate receptol**(E)** in RIM3 KO vs. WT thalamus tissue. Expression levels are indicated as Log2(FoldChange RIM3 KO vs. WT), X-axis represents genes. FC = FoldChange. Data are shown as mean ± SEM. * = FDR<0.05.

In the postsynaptic compartment (Figure 3.2 C), we observed transcriptional downregulation of *Shank3*. The eponymous gene product is a key scaffolding protein at the PSD of excitatory synapses, where it connects different postsynaptic membrane and scaffolding proteins with the cytoskeleton, and has been frequently associated with autism (Boeckers et al., 2002; Monteiro and Feng, 2017; Uchino and Waga, 2013). Among GABAergic receptors (Figure 3.2 D), we found *Gabrb2* to be significantly downregulated, additionally to the already mentioned subunits *Gabra4* and *Gabrd*. Furthermore, RIM3 seemed to affect the gene expression of different glutamate receptor subtypes (*Gria3, Grik4, Grin2c, Grin3a, Grm1*) (Figure 3.2 E).

Taken together, several genes were affected by RIM3 KO that are involved in regulating neuronal excitability and therefore maintenance of an appropriate excitation-inhibition balance in neuronal networks.

3.1.2 Changes in the cortical transcriptome are less distinct than in the thalamus, but show association with activity-dependent gene transcription

RNA-sequencing identified 10,148 genes to be expressed in the cortices of RIM3 KO and WT mice (Figure 3.3 A). Of these, a total of 63 DEGs were determined, including 50 up-regulated genes and 13 down-regulated genes (Figure 3.3 B).

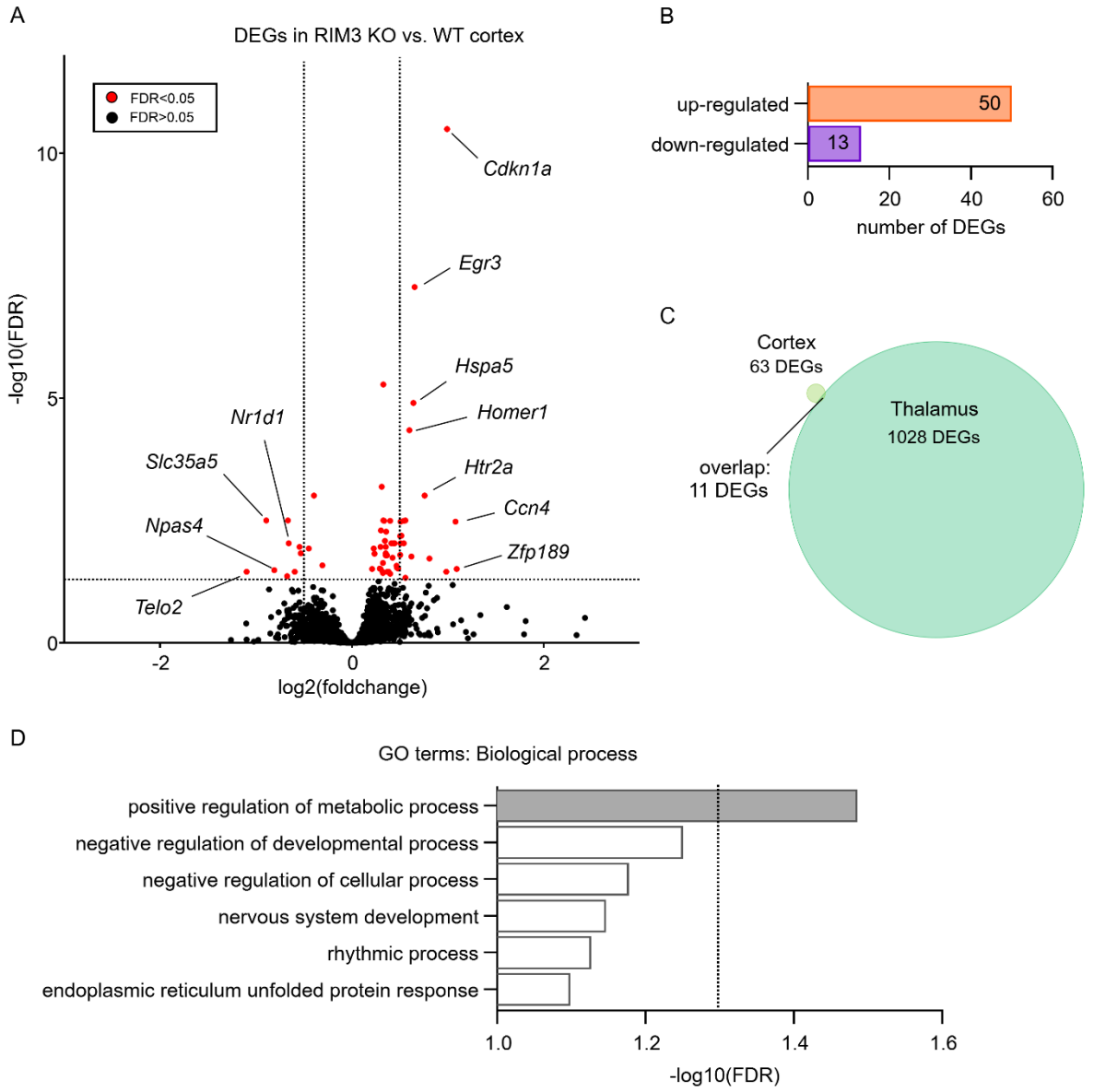

Figure 3.3: Differentially expressed genes in RIM3 KO vs. WT in the cortex. (A) Volcano plot showing differentially expressed genes (DEGs) in cortical tissue of RIM3 KO (n=5) compared to WT (n=5) mice. X-axis represents Foldchange (FC) of gene expression levels in RIM3 KO vs. WT, shown as log2 Foldchange. Y-axis represents level of significance, shown as -log10 adjusted p-value (FDR). Each gene is color based on the -log10(FDR). Red dots represent FDR <0.05, black dots represent FDR > 0.05. Interesting candidate genes among the most up-/down-regulated

DEGs were marked and named. **(B)** A total of 63 DEGs was identified, including 50 up-regulated (orange) and 13 down-regulated (violet) genes. **(C)** Venn diagram showing overlap between cortical (63) and thalamic (1028) DEGs, consisting of 11 genes. **(D)** GO analysis: significantly enriched GO-terms in the category biological process. Color of bars is based on the -log10(FDR). Grey bars indicate FDR < 0.05, white bars indicate FDR > 0.05. Dashed line indicates FDR = 0.05. X-axis represents GO-terms.

GO analysis (Figure 3.3 D) revealed that cortical DEGs showed significant enrichment only in the GO term positive regulation of metabolic process (GO:0009893). Other GO terms found for biological processes did not reach significance but were still listed as potential candidates pointing towards possible functions. In the categories cellular localization and molecular function there were no significantly enriched GO terms.

Investigating the function of the most prominent DEGs using literature research, it became apparent that RIM3 KO in the cortex lead to less specific transcriptomic changes than in the thalamus, also with generally lower fold-changes. The DEGs with the highest differential expression indicate participation of RIM3 in a variety of neuronal processes.

Two interesting candidates were the transcriptional regulators *Egr3* (log2FC = 0.7) and *Npas4* (log2FC = - 0.8), both of which are activated by changes in neuronal activity. *Egr3,* which was upregulated, plays a role in hippocampal LTP (Li et al., 2007), while *Npas4*, which was downregulated, has been shown to initiate the formation of inhibitory synapses onto excitatory neurons, in response to excitatory synaptic activity (Spiegel et al., 2014).

Furthermore, *Telo2,* which displayed the strongest downregulation (log2FC = - 1.1), as well as the strongly upregulated genes *Zfp189*, *Ccn4*, *Cdkn1a* and *Hspa5* (log2FC = 1.1, 1.1, 1.0 and 0.6, respectively) are associated with regulation of cell cycle, stress response and cell survival (Feng et al., 2016; Lorsch et al., 2019; Manu et al., 2019; Wang et al., 2012; Wang et al., 2017).

Another finding was the strong upregulation of the serotonin receptor 2A gene *Htr2a* (log2FC = 0.8), which, consistent with the findings of RIM3 KO in the thalamus (Figure 3.1), points towards function of RIM3 in various transmitter systems. Additionally, the downregulated gene *Nr1d1* (log2FC = - 0.7), encoding the nuclear receptor Rev-ERB-α, plays an important role in cortical development (Goto et al., 2017), but is also a key

element of circadian rhythm, together with *Dbp* (not shown, log2FC = - 0.6) and already mentioned transcription factor *Npas4* (Rijo-Ferreira and Takahashi, 2019; Xu et al., 2021).

As shown in the Venn diagram (Figure 3.3 C), DEGs of thalamus and cortex showed an overlap of 11 genes (*Npas4, Usp2, Sox9, Nr2f1*, *Rock2, Klf9, Gfod1, Ptpn1, Galnt9, Kdm7a, Pdp1*).

Gene expression levels of pre- and postsynaptic components in RIM3 KO

In the cortex, none of the synapse-associated genes that were differentially expressed in the thalamus were significantly up- or down-regulated after KO of RIM3 (Figure 3.4).

Homer1, however, showed a significant upregulation upon RIM3 deletion (FC = 1.52, Figure 3.4 B). *Homer1* encodes the postsynaptic scaffolding protein Homer1, which is a key player at the PSD and is able to modulate mGluR and AMPA-R surface expression in response to changes in synaptic activity (Shan et al., 2018; Ulrich, 2002).

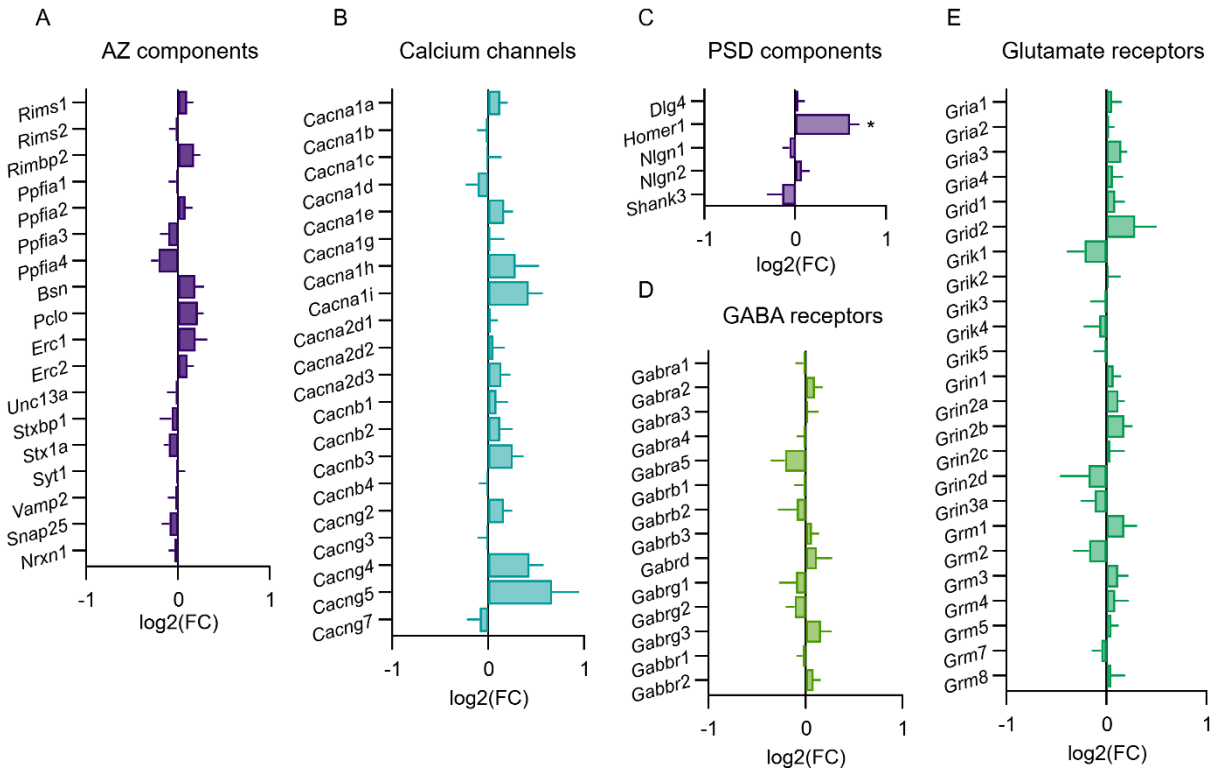

Figure 3.4: RIM3 KO in the cortex enhances *Homer1* expression but does not affect mRNA levels of other synapse-related genes. (A-E) Relative gene expression levels of different presynaptic active zone components **(A)** and calcium channels **(B)**, postsynaptic density components **(C)**, GABA receptors **(D)** and glutamate receIrs **(E)** in in RIM3 KO vs WT cortex

tissue. Expression levels are indicated as Log2(FoldChange RIM3 KO vs. WT), X-axis represents genes. FC = FoldChange. Data are shown as mean ± SEM. * = FDR<0.05.

Apart from upregulation of *Homer1*, we did not detect differential expression in any of the listed presynaptic (Figure 3.4 A) and postsynaptic genes (Figure 3.4 C), nor in genes encoding calcium channels, glutamate receptors or GABA receptors (Figure 3.4 B, D-E).

3.2 Protein expression is not affected by deletion of RIM3

To assess if the transcriptional changes we observed after RIM3 deletion correlated with protein expression, we performed mass spectrometry with thalami and cortices from RIM3 WT and KO mice (Figure 3.5). Mass spectrometry identified and quantified a total of 3,576 and 3,584 proteins in thalamus and cortex samples, respectively.

A PCA plot of RIM3 WT and KO mass spectrometry data showed a clear separation of cortex and thalamus tissue, but no visible clustering of WT and KO samples within each brain area (Figure 3.5 A). This indicates that WT and KO do not present different protein expression profiles. Accordingly, we detected no significantly altered protein levels between RIM3 WT and KO, as shown in volcano plots (Figure 3.5 B-C).

Although not significantly changed, the most promising candidate for differential expression after RIM3 KO in the thalamus appeared to be Myelin basic protein (Mbp) (FDR = 0.063; log2FC = 0.8; Figure 3.5 B), which is not only essential for myelin sheath integrity but also has possible functions in cytoskeleton anchoring and Ca^{2+} signaling (Boggs, 2006). In the cortex, however, upregulation of Immunoglobulin γ-2A chain C region (Igh-1a) nearly reached significance (FDR = 0.051; log2FC = 1.1; Figure 3.5 C). Igh-1a is part of the IgG antibody heavy chain and plays a role in immunological responses (Parsons et al., 1983).

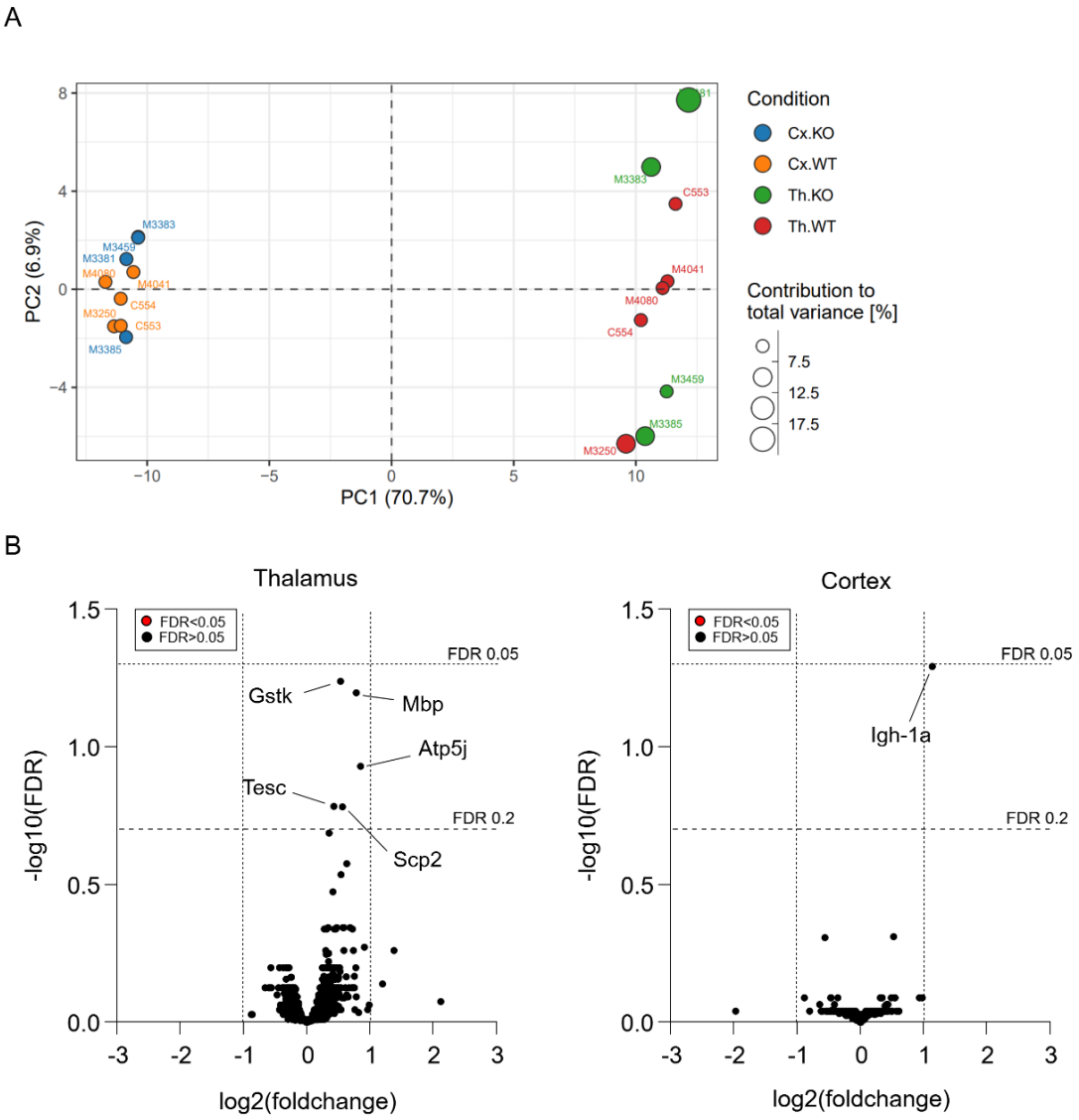

Figure 3.5: RIM3 deletion has no effect on protein expression levels. (A) PCA plot of RIM3 KO and WT mass spectrometry data; thalamus (KO n=4; WT n=5) and cortex (KO n=5; WT n=5). **(B-C)** Volcano plots showing no differentially expressed proteins in thalamic **(B)** and cortical **(C)** tissue of RIM3 KO compared to WT mice. X-axis represents Foldchange (FC) of protein levels in RIM3 KO vs. WT, shown as log2 Foldchange. Y-axis represents level of significance, shown as -log10 adjusted p-value (FDR). Each protein is color based on the -log10(FDR). Red dots represent FDR <0.05, black dots represent FDR > 0.05.

Taken together, we found that the observed changes in the transcriptome of RIM3 KO mice did not lead to corresponding changes in the proteome.

3.3 Multielectrode arrays to investigate neuronal network activity

One of the main aims of this study was to investigate whether RIM3 deletion affects neuronal network function. Since morphological and developmental changes have been described in RIM3 knockdown neurons *in vitro* and *in vivo* (Alvarez-Baron et al., 2013), we were particularly interested in the contribution of RIM3 to network connectivity and development, but also to homeostatic plasticity, with implications for the maintenance of an appropriate excitation-inhibition balance. We used multielectrode arrays (MEA) to study this. In the following, control and optimization experiments are described that verify the use of multielectrode arrays in this study.

3.3.1 Assessment of appropriate cell density for sufficient network formation

In order to reliably achieve neuronal growth and reproducible recordings on MEAs, an appropriate seeding density of cells had to be established that allows network formation and the recording of electrophysiological responses. Cells were seeded at 2500, 4000, 6000, 10000, 16000, 20000 and 40000 cells/well on an area of approximately 5 mm², resulting in seeding densities of approximately 500, 800, 1200, 2000, 3200, 4000 and 8000 cells/mm², and recorded as described above (Materials & Methods, Section 2.9.2) from DIV16 to DIV18. To test whether neurons grow sufficiently to produce reliable responses throughout the network, the percentage of active electrodes per well was assessed for each density.

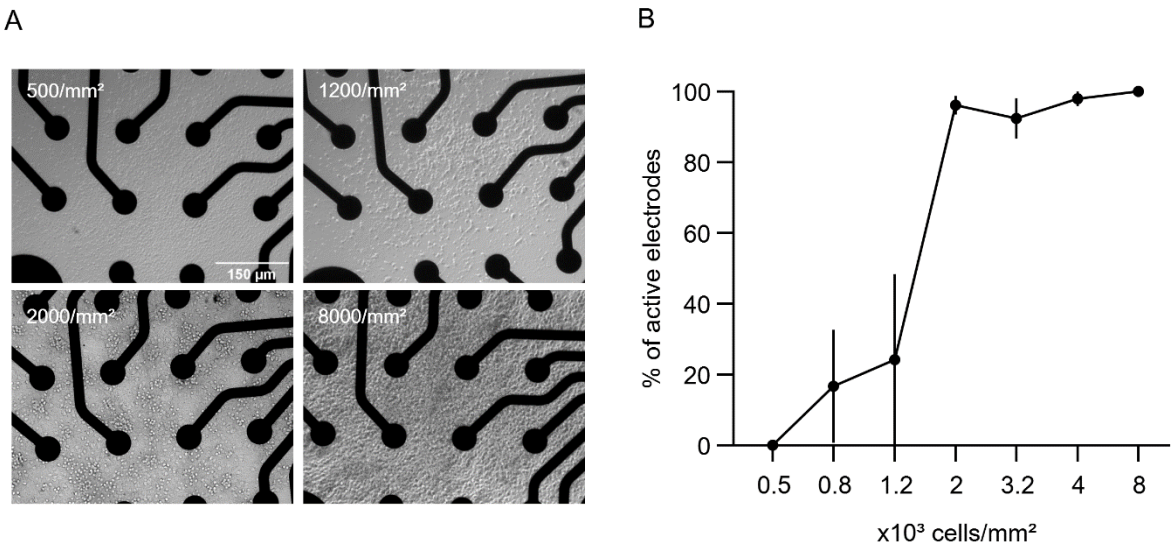

Figure 3.6: Sufficient neuronal growth for recording activity on MEA is achieved at a seeding density of 2000 cells/mm². **(A)** Representative images of cortical cultures on DIV14, grown on MEA at different seeding densities. **(B)** Assessment of electrophysiological response on MEA for different cell densities, measured in percentage of active electrodes per well. Active electrodes are defined by exhibiting a mean firing rate of > 5 spikes/min in recordings of three subsequent days, fr–m DIV16 - DIV18. Data are shown as mean ± SEM. For each culture, percentage of active electrodes was averaged across all wells belonging to one density. Mean ± SEM were calculated from the resulting group averages per culture. N (cultures) and n (wells) for each density: N=3, n=2 (500 cells/mm^2); N=4, n=3-12 (800 cells/mm^2); N=3, n=4-12 (1200 cells/mm^2); N=7, n=3-6 (2000 cells/mm^2); N=3, n=2-3 (3200 cells/mm^2); N=3, n=3 (4000 cells/mm^2); N=3, n=2 (8000 cells/mm^2).

As shown in brightfield images of MEA wells (Figure 3.6 A), cultures seeded at 500 and 1200 cells/mm² (800 cells/mm² not shown) displayed no to very few surviving neurons, while extensive survival started at a density of 2000 cells/mm². Consistent with these observations, assessment of electrophysiological responses (Figure 3.6 B) revealed that at low densities, i.e. 500, 800 and 1200 cells/mm², the majority of electrodes remained inactive. There could be a clear change observed between 1200 cells/mm² and 2000 cells/mm², with the percentage of responding electrodes increasing from 24.2 ± 24.2 % to 96.1 ± 2.6 %, therefore identifying 2000 cells/mm² as the lowest cell density to achieve sufficient neuronal growth on MEA. Higher densities only increased the responsiveness slightly, with the highest density tested, 8000 cells/mm², reaching 100% of active electrodes. At this density, cells appeared extremely dense (Figure 3.6 A), making it impossible to identify single neurons. At 2000 cells/mm², in contrast, cells were growing extensively and reliably but were mostly still distinguishable and appeared to grow planar.

3.3.2 Culture density influences maturation and spontaneous network behavior

To observe neuronal activity and its development under different conditions, the spontaneous activities of the lowest cell density at which neurons survived to a large extent (2000 cells/mm²) and the highest density (8000 cells/mm²) tested in the prior experiments (Figure 3.6) were measured and compared. Recordings were obtained from DIV14 to DIV18 and analyzed regarding quantitative features of overall activity such as mean firing rate, as well as characterization of the firing patterns, e.g. network burst percentage and synchronicity. In the following, the tested densities 2000 cells/mm² and 8000 cells/mm² are referred to as low-density and high-density, respectively.

Analysis of electrophysiological recordings revealed that there is a clear difference between neuronal networks with seeding densities of 2000 cells/mm² and 8000 cells/mm², regarding the overall neuronal activity (Figure 3.7). Mean firing rates of low-density networks were significantly lower compared to high-density networks, with reductions of 71.1 ± 6.3 %, 69.0 ± 10.6 %, 63.3 ± 10.8 % and 43.6 ± 15.1 % on DIV14, DIV15, DIV16 and DIV18, respectively. This difference in general firing frequency is reflected by representative raw traces of both densities on the first and last day of recording (Figure 3.7 B). Mean firing rates were 1.62 ± 0.06 Hz (DIV14), 2.39 ± 0.89 Hz (DIV15), 2.84 ± 0.91 Hz (DIV16), 3.55 ± 1.78 Hz (DIV17) and 2.92 ± 0.09 Hz (DIV18) in low-density cultures and 6.67 ± 1.67 Hz (DIV14), 7.44 ± 0.42 Hz (DIV15), 7.66 ± 0.22 Hz (DIV16), 6.66 ± 0.73 Hz (DIV17) and 6.18 ± 1.23 Hz (DIV18) in high-density cultures.

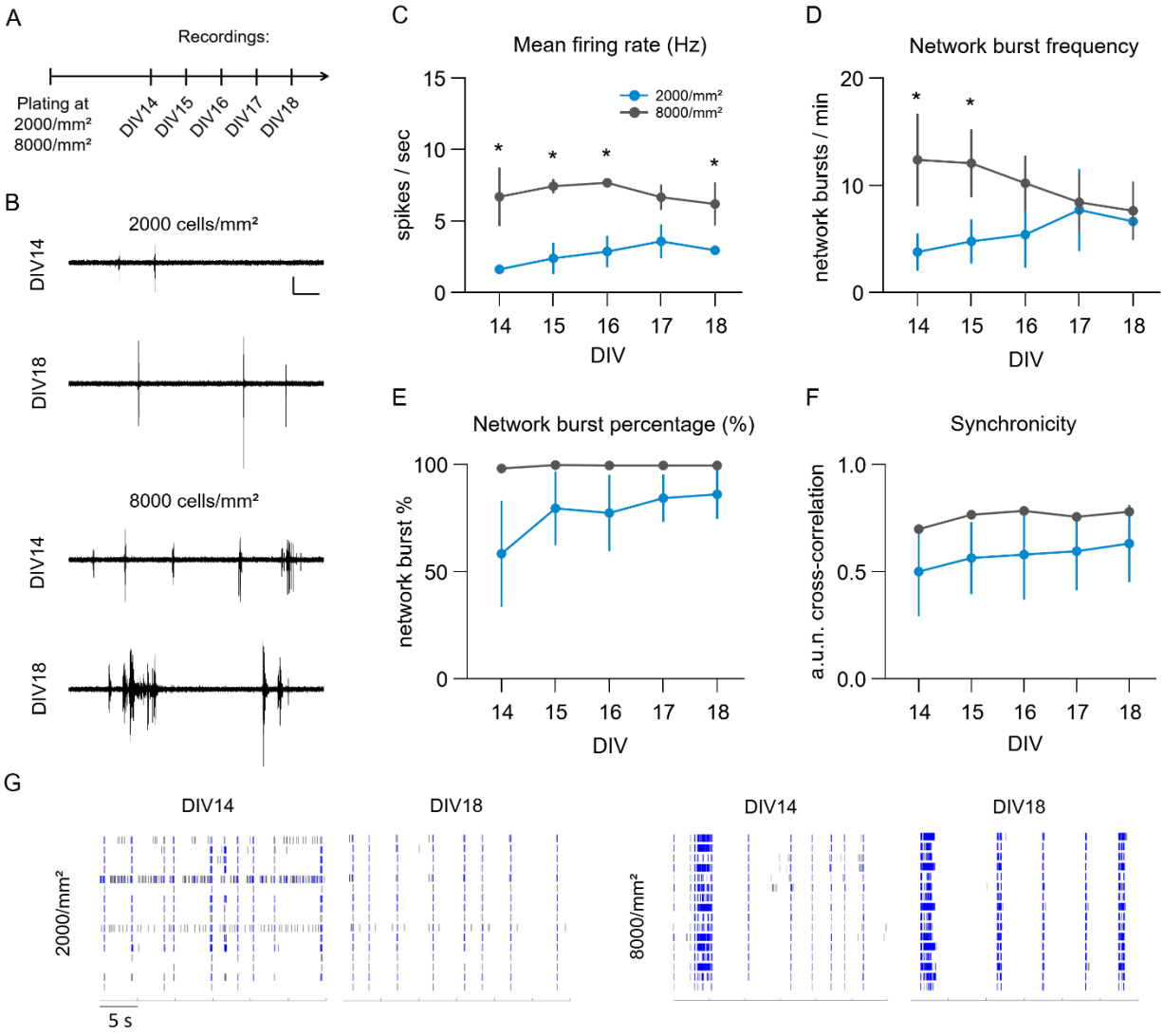

Figure 3.7: Development of spontaneous neuronal activity in cultures of different density. **(A)** Experimental workflow: primary cortical neurons were seeded at densities of 2000 and 8000 cells/mm² and recorded from DIV14 – DIV18. **(B)** Representative raw traces of 2000 cells/mm² and 8000 cells/mm² on DIV14 and DIV18. Scale bar 25 µV, 1 s. **(C-D)** Mean firing rates (Hz) and network burst frequencies (network bursts/min) of 2000 and 8000 cells/mm², measured from DIV14 – DIV18, showed significantly higher activity in high density cultures, compared to low density cultures. **(E-F)** Network burst percentage and synchronicity, measured in area under norm. cross-correlation, of both densities from DIV14 – DIV18. Data are expressed as mean ± SEM. N=3 cultures, n=4 wells each. For each culture, activity was averaged across all wells belonging to one density. Mean ± SEM were calculated from the resulting group averages per culture. Statistical significance was assessed with repeated measures two-way ANOVA, followed by Holm-Sidak's post-hoc test for multiple comparisons (* $p < 0.05$). **(G)** Representative raster plots of MEAs with 2000 and 8000 cells/mm², showing 30 s of neuronal activity at DIV14 and DIV18.

While the mean firing rate is a quite general parameter for overall activity, the frequency of network bursts can give more insights into network activity and development of cultures. Low-density cultures displayed significantly lower network burst frequencies than high-density cultures in earlier stages (Figure 3.7 D), reduced by 74.1 ± 7.5 % on DIV14 (network bursts/min: low-density 37.7 ± 14.4, and high-density 123.5 ± 35.3) and 63.2 ± 6.3 % on DIV15 (network bursts/min: low-density 47.4 ± 16.7, and high-density 120.3 ± 26.0). In later stages (DIV16 – DIV18), network burst frequencies of the two densities seemed to converge.

Another feature characterizing the temporal clustering of spikes into network bursts, is the network burst percentage. From the beginning of the recording on DIV14 almost all spikes in high-density cultures were organized in network bursts (DIV14: 98.07 ± 0.72 %, DIV15: 99.53 ± 0.08 %, DIV16: 99.35 ± 0.21 %, DIV17: 99.49 ± 0.21 %, DIV18: 99.5 ± 0.30 %). In low-density cultures the network burst percentage appeared to be lower and more variable (DIV14: 58.16 ± 20.28 %, DIV15: 79.45 ± 14.11 %, DIV16: 77.19 ± 14.61 %, DIV17: 84.24 ± 9.13 %, DIV18: 85.98 ± 9.39 %) but the difference did not reach significance (Figure 3.7 E). These observations are underlined by representative raster plots of both densities, where low-density cultures display a higher degree of tonic, single-electrode firing, especially in early stages, which is mostly absent in high-density cultures (Figure 3.7 G).

Synchronicity showed no significant differences between both densities, but similar to network burst percentage, low-density cultures displayed a much higher degree of variability in synchronicity compared to high density cultures, as can be seen by the error bars (Figure 3.7 F). Though frequencies might differ, high-density cultures exhibited a very high inter-experiment-stability, regarding the firing pattern.

Additionally, network burst frequency, network burst percentage and synchronicity in low-density cultures showed a tendency towards increasing values from DIV14 to DIV18, whereas in high-density cultures the parameters seemed to already have reached a plateau and stayed relatively stable throughout the days. This was also reflected in representative raster plots of both densities on the first and last day of recording (Figure 3.7 G).

Taken together, cultures seeded at 2000 cells/mm² and 8000 cells/mm² show different types of network activity. As will be elaborated in the Discussion Section 4.2, low-density cultures appeared to be more suited for our experiments and were thus used for the MEA experiments in this thesis, unless stated otherwise.

3.3.3 Induction of homeostatic plasticity with TTX

Silencing with Tetrodotoxin (TTX) is a widely used approach to chemically induce homeostatic plasticity in cultured neurons (Turrigiano et al., 1998). Since TTX is a blocker of voltage-gated sodium channels which are required for action potential firing, it abolishes all neuronal activity (Turrigiano et al., 1998). We wanted to test whether homeostatic plasticity can be induced in MEA cultures with the before tested density of 2000 cells/mm².

Therefore, we silenced cultured cortical neurons with TTX for 48 h, followed by washout (Figure 3.8 A). Recordings and analysis of post-silencing effects were performed as described in Methods Section 2.9.5.

Mean firing rates after washout were 92.3 ± 22.1 % of baseline activity in control (ctrl) and 119.1 ± 23.5 % of baseline activity in the TTX group (Figure 3.8 E). As shown in Figure 3.8 F, the resulting post-silencing effect on mean firing rates was an increase of 40.0 ± 24.9 % compared to control that was not significant.

While the frequency of bursting remained unchanged (burst frequency, %-of-baseline after treatment: 107.3 ± 29.4 % in control and 98.2 ± 31.5 % in TTX, Figure 3.8 G), bursts showed a tendency towards longer durations after TTX treatment, with an increase of 93.1 ± 41.1 % compared to control (burst duration, %-of-baseline after treatment: 84.7 ± 9.0 % in control and 159.3 ± 30.9 % in TTX, Figure 3.8 H). Despite the burst durations being consistently increased throughout the replicates, the difference did not reach significance ($p = 0.107$). Network burst frequency (%-of-baseline after treatment: 156.2 ± -48.0 % in control and 116.7 ± 54.0 % in TTX) and synchronicity (area under norm. cross-correlation, %-of-baseline after treatment: 107.0 ± 1.6 % in control and 113.3 ± 15.4 % in TTX) showed no significant differences (Figure 3.8 I-J).

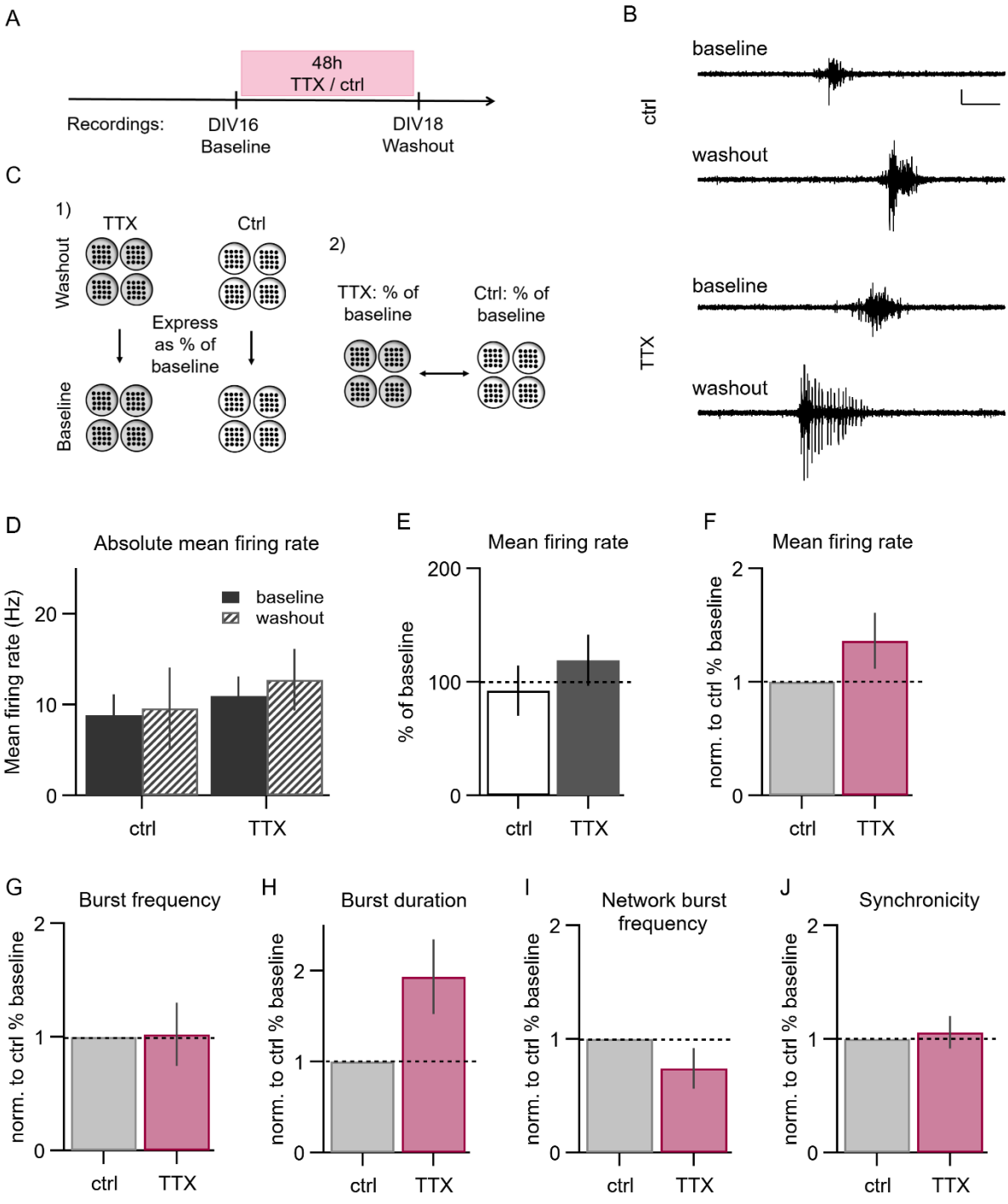

Figure 3.8: TTX induces a trend towards prolonged burst durations in cortical neuronal networks *in vitro*. **(A)** Experimental workflow: primary cortical neurons were seeded at 2000 cells/mm²; baseline recording was performed on DIV16 and neurons were then incubated for 48 h with 1 µM TTX or water as control treatment (ctrl), followed by washout and subsequent recording. **(B)** Representative raw traces of spontaneous firing before application of TTX/ctrl, as well as after washout, indicating prolonged bursting after TTX treatment. Scale bar 20 µV, 250 ms. **(C)** Data analysis. First (1), activities of TTX and ctrl wells after washout were expressed as a

percentage of their baseline. In the second step (2) the percentage-of-baseline TTX values for each well were averaged and normalized to the averaged percentage-of-baseline ctrl values. **(D)** Absolute mean firing rates of the ctrl and TTX groups before treatment and after washout. N=4 cultures, n=3-Iells. **(E)** Mean firing rates of TTX and ctrl after washout expressed as %-of-baseline activity. Baseline indicated as dashed line. **(F)** Post-silencing effect on mean firing rate**:** TTX %-of-baseline normalized to control %-of-baseline. Control %-of-baseline indicated by dashed line. **(G-J)** Post-silencing effects of TTX on burst frequency **(G)**, burst duration **(H)**, network burst frequency **(I)** and synchronicity (area under norm. cross-correlation) **(J)**. TTX %-of-baseline normalized to ctrl %-of-baseline. N=4 cultures, n=3-4 wells. Data in bar graphs show mean ± SEM. Statistical significance was assessed using paired t-test (* $p < 0.05$).

Although not significant, the consistently increased burst durations we observed after TTX treatment suggest that through blocking neuronal activity, TTX might have induced a homeostatic adjustment of the network.

3.3.4 Gabazine induces network synchronization as an immediate effect but no homeostatic plasticity in cortical neurons on MEA

Another approach to test for chemically induced homeostatic plasticity, is the treatment with the highly specific $GABA_A$ receptor antagonist Gabazine. By blockade of GABA-mediated hyperpolarization through influx of negatively charged chloride into the neuron, Gabazine disrupts GABAergic inhibition (Figure 3.9 A), thus leading to hyperexcitability of the network (Ahtiainen et al., 2021; Fan et al., 2019). Since chronic activity elevations have been shown to induce down-scaling of synaptic strength in whole-cell patch clamp recordings (Turrigiano et al., 1998), we wanted to test how Gabazine directly affects neuronal network activity and whether homeostatic modulations can be observed via MEA recordings and analysis.

To this end, we treated primary cortical neurons with Gabazine (Gbz) or water as control treatment (ctrl) and recorded electrophysiological activity at baseline, at an early timepoint (20 min of incubation), at a late timepoint (24 h of incubation) and after subsequent washout (Figure 3.9 B).

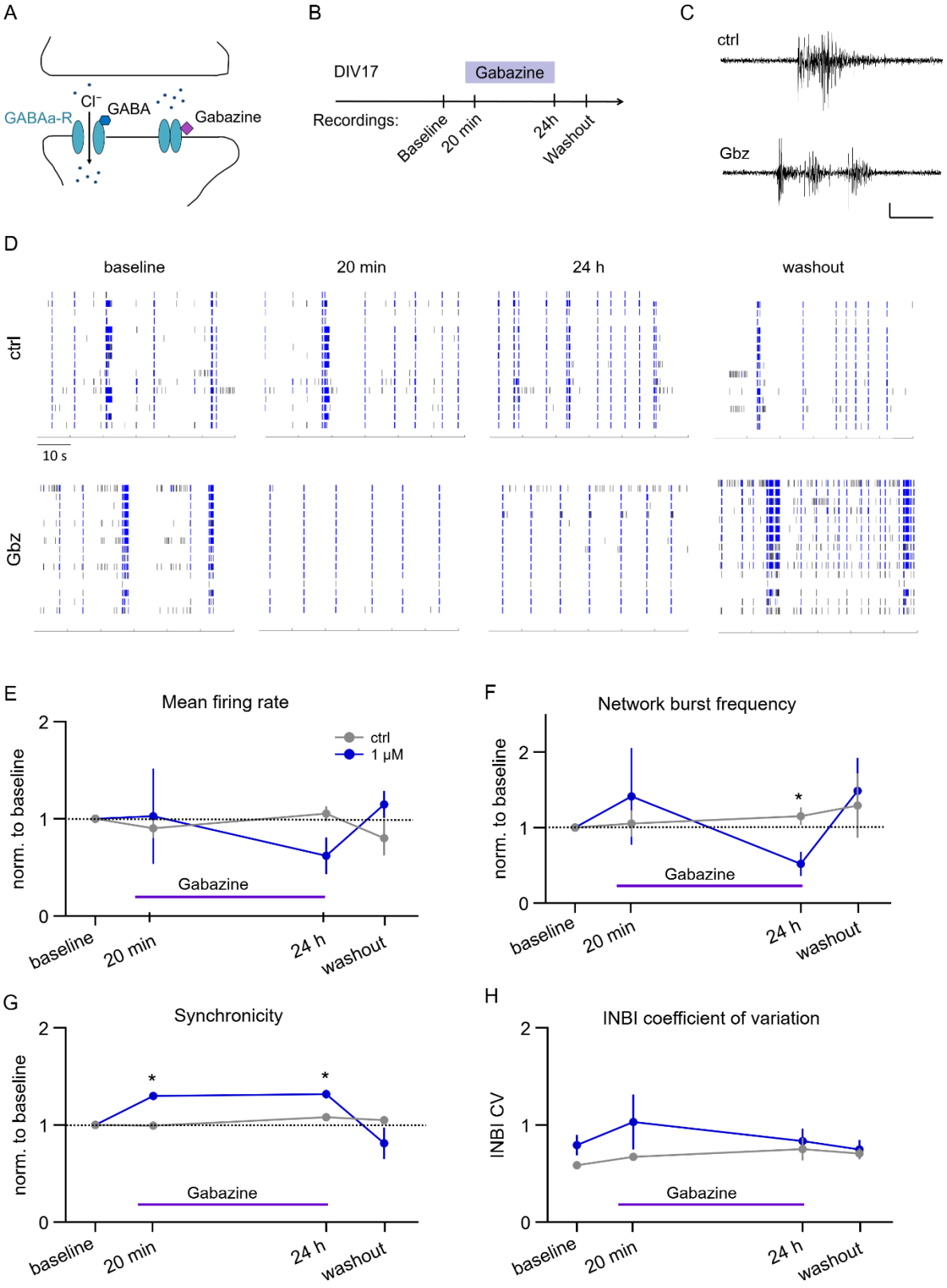

Figure 3.9: Gabazine induces network synchronization as an immediate effect but no homeostatic plasticity. (A) Schematic image of Gabazine (Gbz) mechanism. Binding of GABA

to the $GABA_A$ receptor causes hyperpolarization via influx of chloride ions and thus inhibition of the postsynaptic neuron. Gbz acts as an antagonist of the $GABA_A$ receptor, therefore disrupting inhibition. **(B)** Experimental workflow. Primary cortical neurons were seeded at 2000 cells/mm² and incubated with 1 µM Gbz or water as control treatment (ctrl) on DIV17 for 24 h, followed by washout. MEA recordings were performed before Gbz application (baseline), 20 min after application, 24 h after application and after washout. **(C)** Representative raw traces of Gbz and ctrl neurons showing burst structure 20 min after application. Scale bar: 20 µV, 100 ms. **(D)** Representative raster plots of Gbz and ctrl neurons showing 60 s of neuronal activity over the experimental tl course. **(E)** Mean firing rates of Gbz and ctrl neurons, normalized to their baseline, over the experimental time course. **(F)** Network burst frequencies of Gbz and ctrl, norm. to baseline, showed a significant reduction 24 h after Gbz application. **(G)** Synchronicity, measured as area under norm. cross-correlation, of Gbz and ctrl neurons, norm. to baseline, was highly increased 20 min and 24 h after Gbz application **(H)** INBI coefficient of variation of Gbz and ctrl neurons. N=5 cultures, n=3 wells. Data are expressed as mean ± SEM. For each well, activity at different timepoints was normalized to its baseline. Within each culture, these normalized values were averaged across all wells belonging to one group. Mean + SEM were calculated from the resulting group averages per culture. INBI = Inter-network-burst-interval. Statistical significance was assessed with repeated measures two-way ANOVA, followed by Holm-Sidak's post-hoc test for multiple comparisons (* $p < 0.05$).

Primarily, Gabazine induced highly synchronous activity 20 min after application (Figure 3.9 G), with a significant increase in synchronicity by ~30 % compared to control (area under norm. cross-correlation, normalized to baseline: 1.30 ± 0.02 and 0.99 ± 0.02 in Gbz and ctrl, respectively). 24 h later, synchronicity was still ~22 % higher than in control (area under norm. cross-correlation; normalized to baseline: 1.32 ± 0.04 and 1.08 ± 0.03 in Gbz and ctrl, respectively). After washout, however, synchronicity was lower but not significantly different from control (area under norm. cross-correlation; normalized to baseline: 0.81 ± 0.16 and 1.05 ± 0.03 in Gbz and ctrl, respectively).

In our experiments, Gabazine did not elevate the overall activity as an immediate effect (Figure 3.9 E). While there was no change in mean firing rates 20 min after application, after 24 h the mean firing rate appeared to be reduced compared to control, but was not significantly different (mean firing rate, norm. to baseline: 0.62 ± 0.19 and 1.05 ± 0.08 in Gbz and ctrl, respectively).

Network burst frequencies showed a significant reduction by ~55 % compared to control after 24 h of incubation (network bursts/min, norm. to baseline: 0.52 ± 0.16 and 1.14 ± 0.11 in Gbz and ctrl, respectively, Figure 3.9 F). However, this observed network burst suppression did not lead to a homeostatic upregulation, as network burst frequencies increased but did not differ from control after removal of Gabazine (network bursts/min,

norm. to baseline: 1.48 ± 0.44 and 1.29 ± 0.43 in Gbz and ctrl, respectively). Given the fact that the reduction in network burst frequency did not occur immediately, but after 24 h, it can be discussed whether this alteration itself might be a product of homeostatic mechanisms. Inter-network-burst-interval (INBI) coefficient of variation, a measure of network burst irregularity, did not differ between Gabazine and control at any timepoint (Figure 3.9 H). As shown in representative raw traces (Figure 3.9 C), another effect observed 20 min after application of Gabazine was the induction of a triphasic burst structure which does not present itself under control conditions.

Taken together, Gabazine induces an immediate and persisting network synchronization, as well as a delayed appearing network burst suppression. After washout, the alterations vanished as would be expected after the removal of a drug but showed no further opposing effects in the sense of a homeostatic response.

3.4 Functional role of RIM3 in neuronal micro-networks

One of the aims of this study was to characterize RIM3-deficient neurons on the functional level, using MEA recordings and analysis. We focused on the investigation of homeostatic plasticity effects in RIM3 KO and WT, as well as spontaneous network activity and excitability at different developmental stages. Additionally, we wanted to assess how the network's density and connectivity influences effects of RIM3-deficiency.

For the following experiments, cultured cortical RIM3flox neurons were transduced with lentiviruses expressing active or inactive mutant Cre-recombinase (Cre or ΔCre) to yield RIM3 conditional knockout and corresponding wild-type cells (referred to as RIM3 cKO and WT), respectively.

3.4.1 RIM3 deletion has no effect on homeostatic plasticity

Homeostatic plasticity has been proven to play a major role in maintaining neuronal network function and stability. Since large RIM isoforms are known to be highly involved in homeostatic plasticity mechanisms (Müller et al., 2012; Lazarevic et al., 2011), we wanted to investigate whether RIM3 exerts similar functions in neuronal networks. To test

if deletion of RIM3 leads to any alterations in the induction of homeostatic plasticity on MEAs, RIM3 cKO and WT neurons were silenced with TTX and analyzed as established in prior experiments (Figure 3.8). Here, we found that there were no significant differences in responses to TTX between WT and cKO neuronal networks (Figure 3.10 D-G).

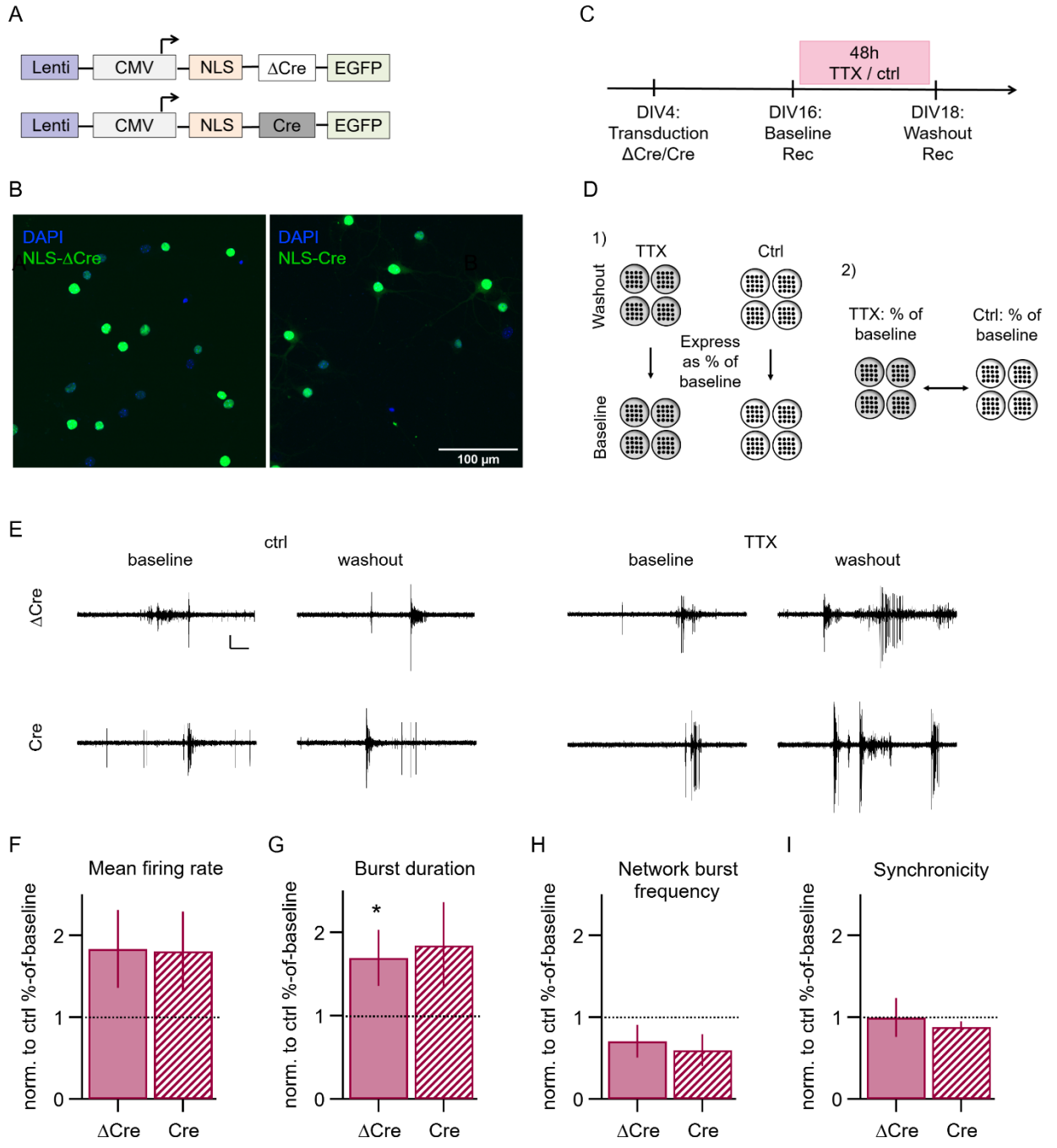

Figure 3.10: Absence of RIM3 does not affect homeostatic response to TTX. (A) Cartoon of lentiviral vectors expressing ubiquitous ΔCre and Cre, which were used to yield WT and RIM3

cKO cells, respectively. **(B)** Representative confocal images of lenti-virally delivered ΔCre and Cre expression in cortical primary neurons. **(C)** Experimental workflow. Primary RIM3flox cortical neurons were seeded at a density of 2000 cells/mm² and transduced with ΔCre or Cre on DIV4 to yield WT and cKO cells, respectively. 1 µM TTX or water as control treatment (ctrl) were applied for 48 h, followed by washout. MEA recordings were performed before application (baseline) and 20 min after washout. **(D)** Data analysis. First, (1) activities of TTX and ctrl after washout were converted to the percentage-of-baseline for each well. In the second step (2) the percentage-of-baseline TTX values for each well were averaged and normalized to the averaged percentage-of-baselinItrl values. **(E)** Representative raw traces of spontaneous firing before application of TTX/ctrl, as well as after washout, for both WT and cKO. Scale bar 20 µV, 500 ms. **(F-I)** Post-silencing effect of TTX on mean firing rate **(F)**, burst duration **(G)**, network burst frequency **(H)** and synchronicity (area under norm. cross-correlation) **(I)** for both RIM3 WT and cKO. TTX %-of-baseline normalized to ctrl %-of-baseline. N=4 cultures, n=3-5 wells. Data in bar graphs show mean ± SEM. Statistical significance was assessed using paired t-test (* $p < 0.05$).

Mean firing rates as well as burst durations appeared equivalently increased in both groups after TTX treatment (mean firing rate: 83.1 ± 47.8 % and 80.3 ± 48.6 % increase in WT and cKO, respectively; burst duration: 69.0 ± 33.6 % and 84.2 ± 51.7 % increase in WT and cKO, respectively; Figure 3.10 F-G). Prolonged bursting after silencing in both WT and cKO neurons is shown by representative raw traces in Figure 3.10 E. This response to silencing with TTX is consistent with our earlier TTX experiments on WT neurons (Figure 3.8). It should be stated though, that in the current experiments performed with WT and cKO, only burst duration in the WT condition displayed a significant post-silencing effect (Figure 3.10 G). Network burst frequency showed an unsignificant reduction in both groups (29.5 ± 19.9 % and 40.0 ± 20.0 % decrease in WT and cKO, respectively; Figure 3.10 H). Synchronicity remained unchanged in both groups (Figure 3.10 I).

Taken together, post-silencing effects of TTX on cortical MEA networks were not altered by the absence of RIM3.

3.4.2 Cell density determines effects of RIM3 on spontaneous network activity

In a next step we wanted to assess the effects of RIM3 deletion on spontaneous network activity and excitability in different types of neuronal networks. Since earlier experiments showed the influence of culture density on network connectivity and electrophysiological properties (Figure 3.7), we wanted to investigate effects of RIM3-deficiency on network

activity in low-density as well as high-density networks, and at different developmental stages.

To this end, WT and RIM3 cKO neurons were seeded at either 2000 or 8000 cells/mm² (referred to as low-density and high-density, respectively) and recorded on DIV14, as an earlier stage of development, and from DIV18 to DIV20 to assess effects at a later stage of development (Figure 3.11 A-B). Within each density, activity of WT wells was averaged and compared to averaged cKO activity for each DIV (Figure 3.11 D-E).

Interestingly, effects of the RIM3 cKO were substantially different between low-density and high-density cultures. In low-density networks, no significant alterations in firing, bursting or network bursting frequencies were observed in the RIM3 cKO at any timepoint (Figure 3.11 F-H). However, the network's synchronicity was significantly elevated in the low-density cKO compared to WT (Figure 3.11 I). On DIV18, a significant increase by 20.5 ± 3.4 % could be observed (area under norm. cross-correlation: 0.39 ± 0.05 and 0.48 ± 0.07 in RIM3 WT and cKO, respectively). Although activity appeared to be generally more synchronous in the RIM3 cKO, differences at other timepoints were not significant ($p = 0.065$ on DIV19; $p = 0.161$ on DIV20).

In contrast, absence of RIM3 in high-density networks significantly reduced neuronal excitability, regarding several parameters. RIM3 cKO displayed a reduction in mean firing rate by 37.3 ± 11.5 % on DIV19 (6.32 ± 1.23 Hz and 4.12 ± 1.36 Hz in RIM3 WT and KO, respectively) and 30.1 ± 6.6 % on DIV20 (6.72 ± 1.76 Hz and 4.96 ± 1.59 Hz in RIM3 WT and KO, respectively, Figure 3.11 F). Figure 3.11 G demonstrates that the burst frequency in high-density RIM3 cKO was likewise reduced by 48.0 ± 8.9 % compared to WT on DIV19 (bursts/min: 142.9 ± 25.4 and 79.1 ± 27.3 in WT and cKO, respectively) and 41.6 ± 5.9 % on DIV20 (bursts/min: 131.2 ± 44.7 and 84.3 ± 34.5 in WT and cKO, respectively).

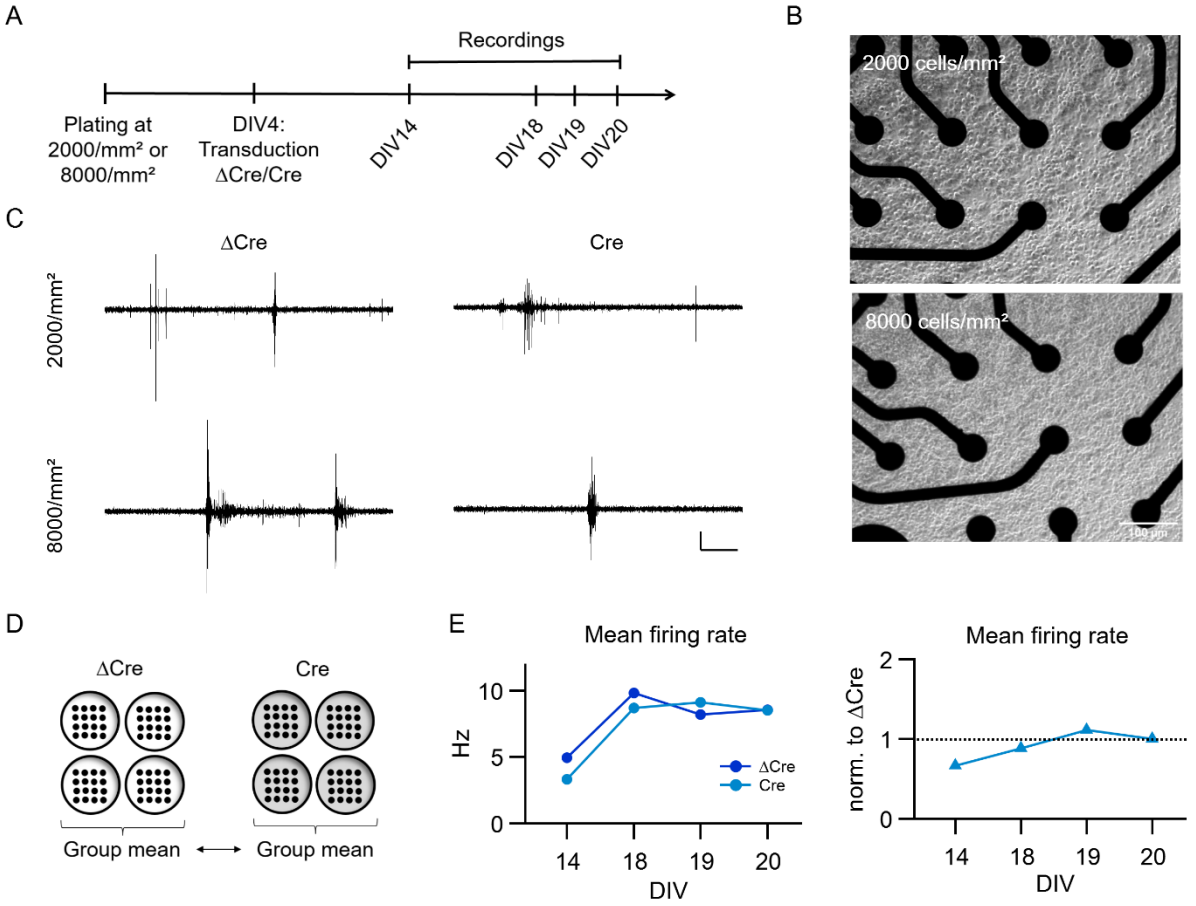
A
Recordings
Plating at 2000/mm² or 8000/mm²
DIV4: Transduction ΔCre/Cre
DIV14
DIV18
DIV19
DIV20
B
2000 cells/mm²
8000 cells/mm²
C
ΔCre
Cre
2000/mm²
8000/mm²
D
ΔCre
Cre
Group mean
Group mean
E
Mean firing rate
Hz
ΔCre
Cre
DIV
Mean firing rate
norm. to ΔCre
DIV
F
Mean firing rate
2000/mm²
8000/mm²
norm. to ΔCre
DIV
G
Burst frequency
norm. to ΔCre
DIV
H
Network burst frequency
norm. to ΔCre
DIV
I
Synchronicity
norm. to ΔCre
DIV

Figure 3.11: RIM3 deletion leads to reduced network excitability at high culture density, but not in low density networks. (A) Experimental workflow. Primary cortical RIM3flox neurons were seeded at a density of 2000 or 8000 cells/mm² and transduced with Δ*Cre* or *Cre* on DIV4 to induce WT and RIM3 cKO, respectively. MEA recordings were obtained on DIV14 and from DIV18-20. **(B)** Representative images of *Cre* treated neurons at low and high density on DIV14. **(C)** Representative raw traces of RIM3 WT and cKO neurons seeded at 2000 cells/mm² and 8000 cells/mm², recorded on DIV19. Scale bar: 25 µV, 250 ms. **(D)** For each density, activities of all wells belonging to one group were averaged and group means of WT and clwere compared. **(E)** Data from a single experiment with 2000 cells/mm²: *Left panel* Absolute mean firing rate of WT and cKO, in Hz. *Right panel* Mean firing rate of cKO was normalized to WT. WT indicated as dashed line. **(F-I)** Mean firing rate **(F)**, burst frequency **(G)**, network burst frequency **(H)** and synchronicity (area under norm. cross-correlation) **(I)** of both densities, shown as RIM3 cKO normalized to WT. N= 6-7 cultures, n=3-4 wells. Data in bar graphs show mean ± SEM. Statistical significance was assessed using repeated measures two-way ANOVA followed by Holm-Sidak's post-hoc test for multiple comparisons. (* $p < 0.05$).

The most prominent effect of RIM3 cKO in high-density networks was a decrease in network burst frequency on DIV19 and DIV20, with a significant reduction by 50.5 ± 7.8 % (network bursts/min: 6.48 ± 0.90 in WT and 3.14 ± 0.62 in KO) and 47.7 ± 4.0 % (network bursts/min: 5.721 ± 1.671 in WT and 3.195 ± 1.105 in KO, Figure 3.11 H), respectively.

Additionally, we observed that alterations of neuronal activity in both densities appear at the end of the third week in vitro (DIV18-DIV20) but are not yet present at DIV14 (Figure 3.11 I). The different effects of RIM3 deletion on neuronal activity become visible in representative raster plots of WT and RIM3 cKO networks of both densities, over the experimental time course (Figure 3.12).

In low-density cultures, activity of WT and RIM3 cKO neurons seemed to develop in a similar way throughout the DIVs (Figure 3.12 A). In contrast, the strong reduction in neuronal activity in high-density cKO cultures was clearly visible: while the activity of WT networks seemed to increase over the recorded time, activity of RIM3 cKO networks appeared to stagnate at DIV18 (Figure 3.12 B).

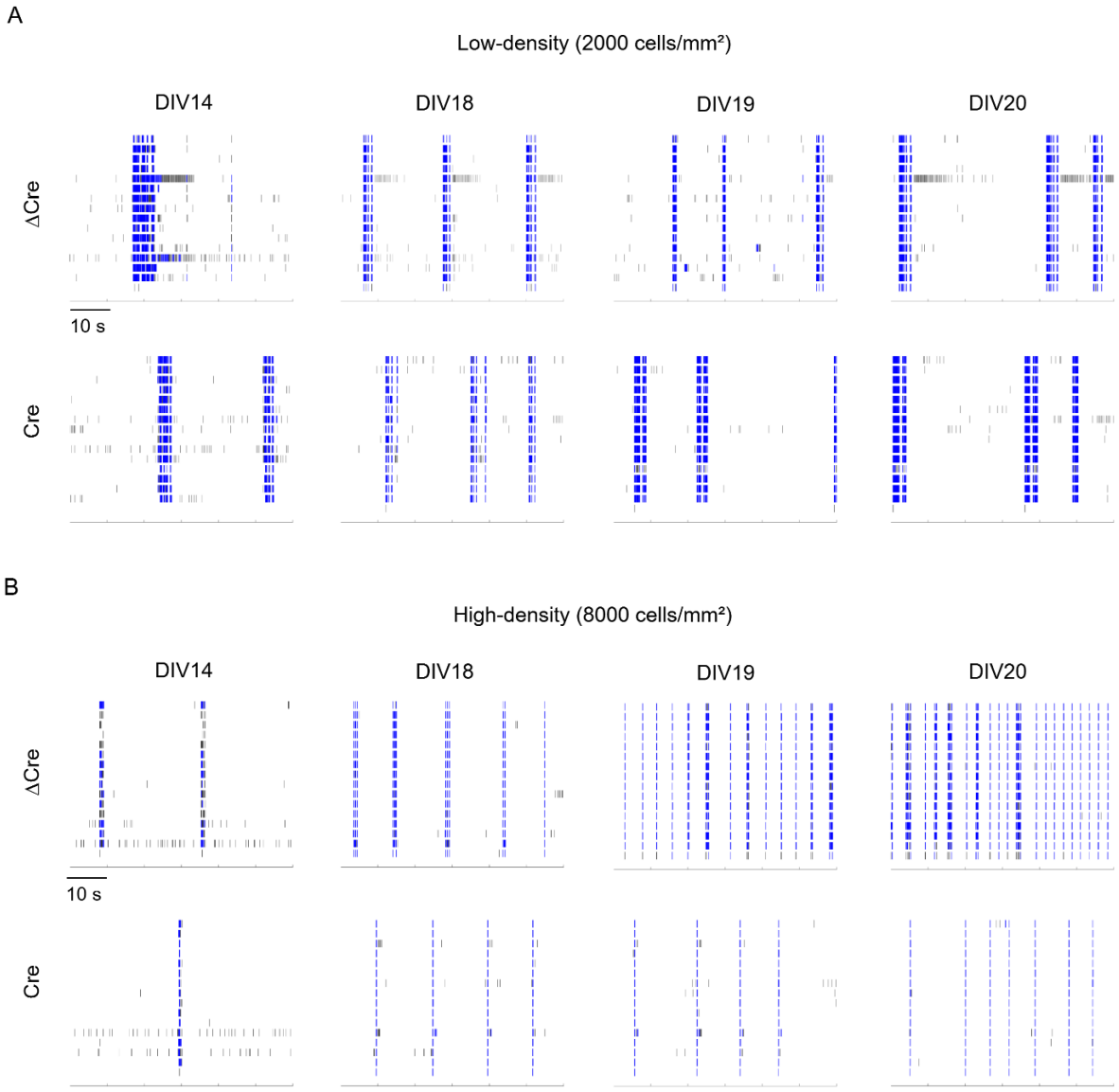

Figure 3.12: Differences in well-wide neuronal activity between RIM3 cKO and WT in low and high culture density. **(A**) Representative raster plots showing 60 s of network activity in WT and cKO neurons seeded at 2000 cells/mm², on DIV14, DIV18, DIV19 and DIV20. **(B)** Representative raster plots showing 60 s of network activity in WT and cKO neurons seeded at 8000 cells/mm², on DIV14, DIV18, DIV19 and DIV20.

What also becomes evident in raster plots of high-density networks is that although firing frequencies were heavily decreased, RIM3 cKO did not disrupt the firing pattern typical for WT networks. Validating this observation, the networks' synchronicity (area under norm. cross-correlation, Figure 3.11 I) remained unaffected by RIM3 cKO.

Taken together, deletion of RIM3 massively reduced network excitability in high-density cultures on MEA, while RIM3 cKO at low-density displayed moderately elevated synchronicity.

3.4.3 Cell survival is not impaired in RIM3 cKO neurons

Although not reflected on the protein level, transcriptomics of RIM3 KO cortical tissue point towards a role of RIM3 in cell survival (Figure 3.3). Therefore, we wanted to test whether earlier cell death, possibly due to dysregulation of survival mechanisms, could be a source for the alterations in neuronal activity we observed in the absence of RIM3 (Figure 3.11).

To this end, cell viability assays of RIM3 cKO and WT cultures seeded on coverslips were carried out at DIV14, DIV18 and DIV20, using the pre-fixation propidium iodide method (Figure 3.13 A). Since propidium iodide is a DNA-intercalating dye that is not permeant to living cells, non-viable cells were identified by nuclear red fluorescent staining (Figure 3.13 B).

Cell viability did not differ between RIM3 WT and cKO neurons (Figure 3.13 D). WT cultures exhibited a percentage of viable cells of 75.15 ± 4.2 %, 72.25 ± 5.45 % and 63.53 ± 10.57 % on DIV14, DIV18 and DIV20, respectively, while cell viability in cKO cultures was 70.67 ± 7.37 %, 60.11 ± 12.88 % and 48.88 ± 6.22 %. These results confirm that the alterations in neuronal activity observed after the cKO of RIM3 are not a result of increased cell death.

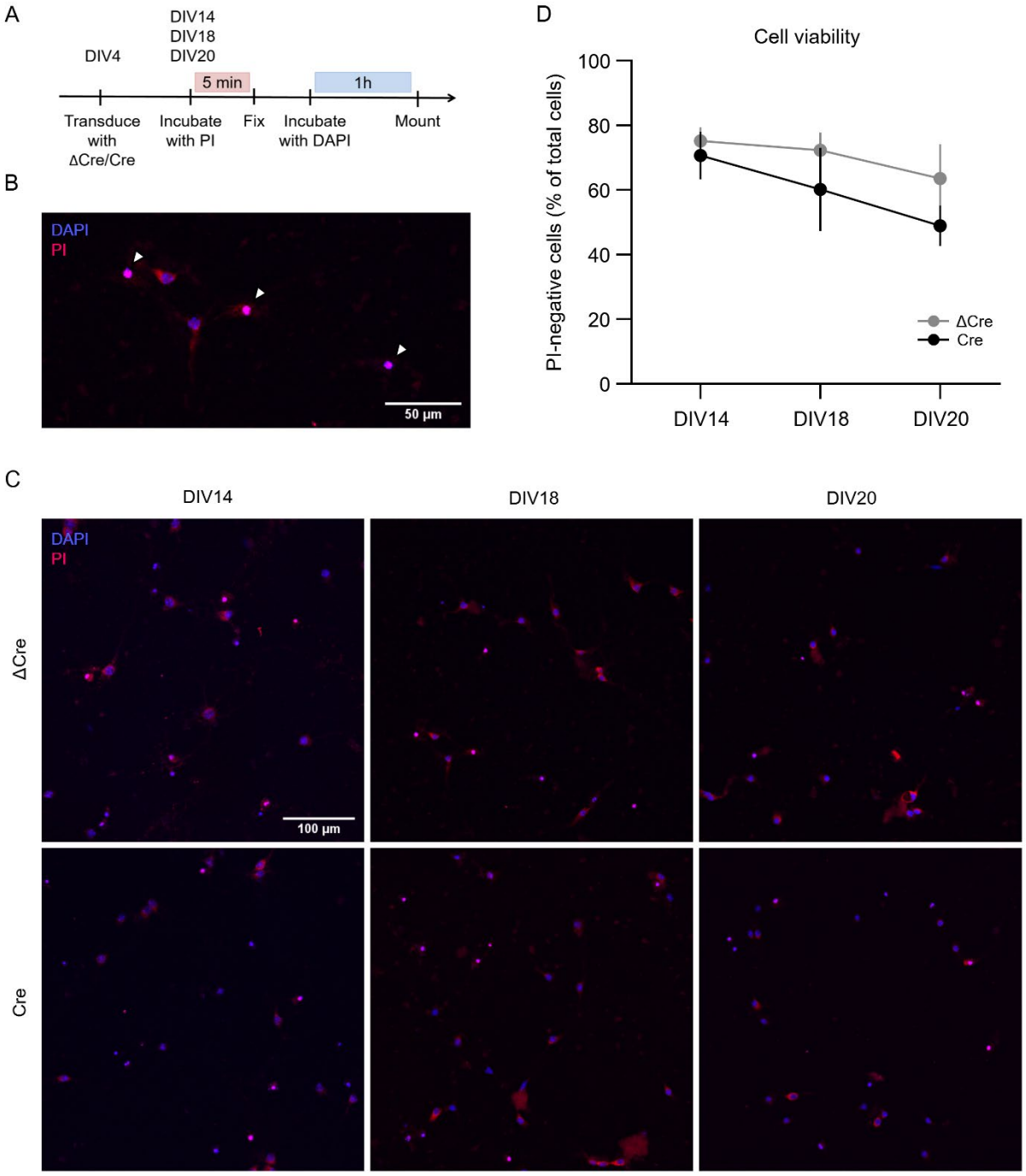

Figure 3.13: Cell survival is not impaired in RIM3 cKO neurons. (A) Experimental workflow of cell viability assay. Cortical Rim3flox neurons were seeded on coverslips and transduced with ΔCre/Cre-expressing viruses on DIV4, to yield RIM3 WT and cKO cells, respectively. On DIV14, DIV18 and DIV20, neurons were incubated with 50 µg/ml propidium iodide (PI) for 5 min, washed, fixed and co-stained with DAPI. **(B)** Representative confocal image of cell viability assay: nuclear staining with propidium iodide (red) was used to identify non-viable cells (white arrows), while the total amount of cells was assessed with DAPI (blue). (**C)** Confocal images of cell viability assays with RIM3 WT and cKO neurons on DIV14, DIV18 and DIV20. **(D)** Cell viability of WT and cKO, measured as percentage of viable cells (PI-negative, DAPI-positive cells divided by total DAPI-positive cells). N=4 cultures, n=3 coverslips each. Graph shows mean ± SEM. For each culture,

percentage of viable cells was averaged across all coverslips belonging to one group. Mean ± SEM were calculated from the resulting group averages per replicate for both WT and cKO. PI = propidium iodide. Statistical significance was assessed using repeated measures two-way ANOVA followed by Holm-Sidak's post-hoc test for multiple comparisons.

3.5 Specific functions of RIM3 in excitatory and inhibitory neurons

Neurons form intricate networks of excitatory (glutamatergic) and inhibitory (GABAergic) subpopulations, whose fine-tuned interactions are essential to regulate neuronal excitability and therefore network function. Since gene expression database mousebrain.org showed that RIM3 is strongly expressed in inhibitory interneurons in the cortex, we were particularly interested in how RIM3 contributes to inhibitory neuronal function. Additionally, we wanted to screen for possible functions of RIM3 in excitatory neurons. In a ubiquitous KO, possible effects in excitatory and inhibitory neurons can outbalance each other – therefore, it was a reasonable next step to separately investigate how RIM3 deletion in both types of neurons affected neuronal network activity and the E-I balance. To this end, we produced cell-type specific conditional knockouts, using viruses which delivered ΔCre/Cre expression under promoters specific to excitatory as well as inhibitory neurons. VGLUT2 (vesicular glutamate transporter 2) served as a glutamatergic promoter (Fremeau et al., 2001), while Dlx (distal-less homeobox) was used as a GABAergic promoter (Dimidschstein et al., 2016).

3.5.1 RIM3 cKO in excitatory neurons enhances network excitability

To reliably yield RIM3 cKO specifically in glutamatergic neurons, we assessed cell-type specificity of the viruses, using immunocytochemistry (Figure 3.14 B). Immunocytochemistry revealed that VGLUT2-ΔCre and -Cre transduced glutamatergic neurons with a specificity of 76.8 ± 7.6 % and 88.2 ± 1.8 %, respectively. These results validate the use of mentioned viruses as a reliable tool to induce RIM3 cKO in glutamatergic neurons.

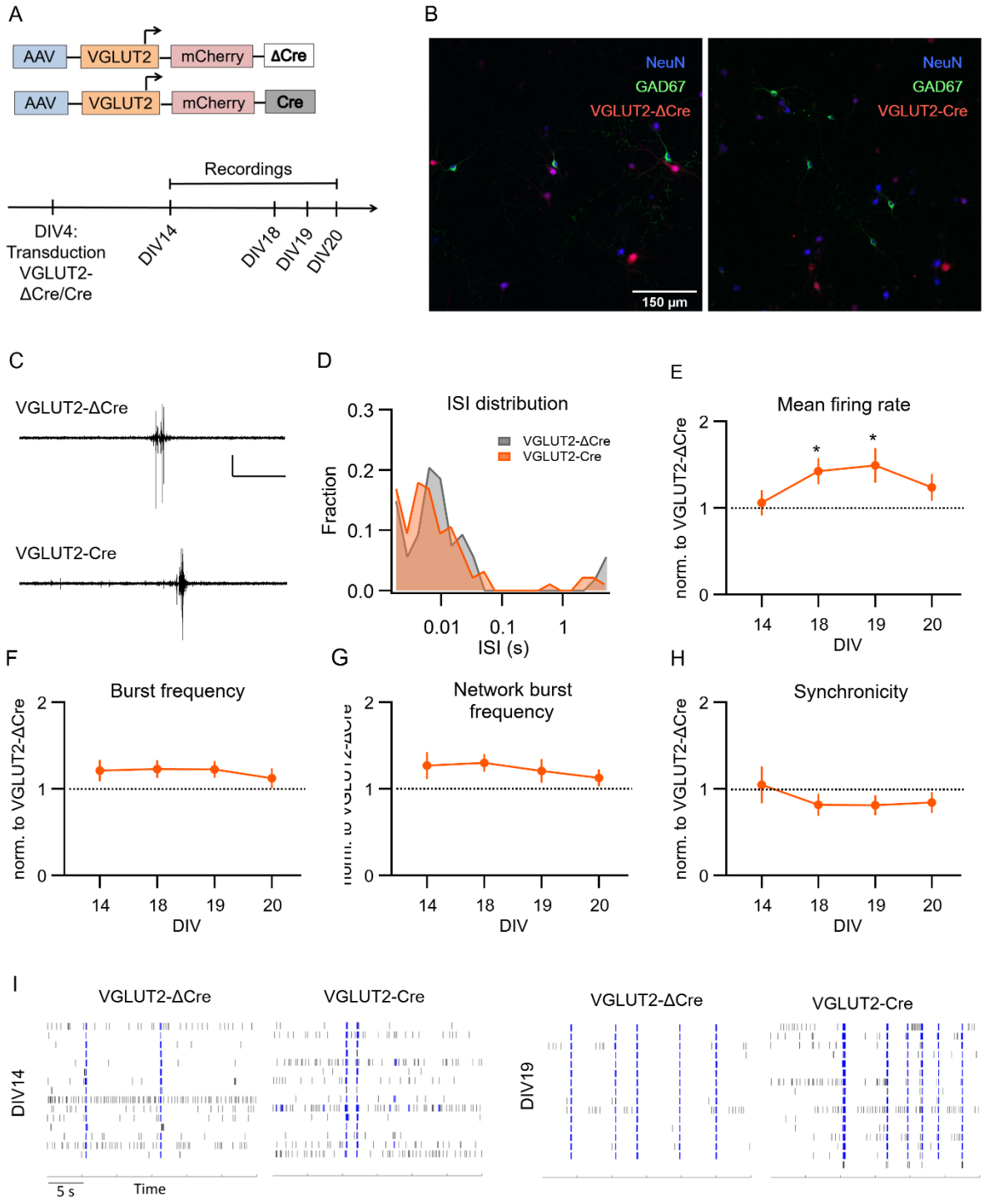

Figure 3.14: Deletion of RIM3 in excitatory neurons increases network excitability. (A) Lentiviral vectors expressing ΔCre and Cre under excitatory-specific VGLUT2-promoter. RIM3flox cortical neurons were seeded at 2000 cells/mm² and transduced on DIV4 with VGLUT2-ΔCre/Cre viruses to yield WT and cKO in glutamatergic neurons, respectively. MEA recordings were performed on DIV14 and DIV18-20. **(B)** Representative confocal images of lenti-virally delivered ΔCre and Cre expression (red) in glutamatergic primary neurons, specifically. Gad67 (green) labels GABAergic neurons, NeuN (blue) labels all neurons. Specificity was assessed by dividing Gad67-negative transduced neurons by the total amount of transduced neurons. N=3 cultures,

n=3 coverslips each. **(C)** Representative raw traces of WT and VGLUT2-specific cKO neurons on DIV19. Scale bar: 50 µV, 500 ms. **(D)** Representative ISI histogram expressing identical ISI distributions of WT and VGLUT2-cKO neurons. Bimodality indicates temporal clustering into bursts. **(EI** Mean firing rate **(E)**, burst frequency **(F)**, network burst frequency **(G)** and synchronicity (area under norm. cross-correlation) **(H)** of VGLUT2-specific cKO normalized to WT. N= 6 cultures, n=3-4 wells. Data in bar graphs show mean ± SEM. For each culture, data of all wells belonging to one group were averaged and group means of VGLUT2-specific cKO were normalized to their corresponding WT group means. Mean + SEM were calculated from the resulting normalized values per culture. Statistical significance was assessed using repeated measures two-way ANOVA followed by Holm-Sidak's post-hoc test for multiple comparisons. (* $p < 0.05$). **(I)** Representative raster plots showing 30 s of well-wide neuronal activity of WT and VGLUT2-specific cKO on DIV14 and DIV19.

Cortical RIM3flox neurons were treated with VGLUT2-Cre and VGLUT2-ΔCre to yield excitatory-specific RIM3 cKO and corresponding WT cells, respectively. Recordings were performed on DIV14 and from DIV18-20 to investigate network properties at different stages of development (Figure 3.14 A).

VGLUT2-specific cKO of RIM3 resulted in a significantly increased mean firing rate, compared to WT (Figure 3.14 E). The mean firing rate was increased by 42.2 ± 15.1 % on DIV18 (4.83 ± 0.38 Hz and 6.62 ± 0.65 Hz in WT and KO, respectively) and 49.0 ± 20.0 % on DIV19 (5.14 ± 0.29 Hz and 7.53 ± 0.98 Hz in WT and KO, respectively). As shown in representative raw traces and ISI histograms from DIV19 (Figure 3.14 C-D), however, firing patterns on the single electrode level appeared quite similar between WT and cKO. Bimodal distribution of ISIs in both groups indicate neuronal activity dominated by bursting (Figure 3.14 D).

Other parameters like burst and network burst frequency (Figure 3.14 F-G) appeared only slightly elevated throughout the recorded DIVs but were not significant. Synchronicity remained unchanged by RIM3 cKO in glutamatergic neurons (Figure 3.14 H). Representative raster plots of well-wide activity underline that while WT and cKO appear similar on DIV14, firing seems to be enhanced in cKO networks on DIV19 (Figure 3.14 I).

Taken together, cKO of RIM3 in glutamatergic neurons results in increased firing rates but unchanged synchronicity.

3.5.2 Deletion of RIM3 in inhibitory neurons leads to disrupted network synchronization

First, cell-type specificity of the virally delivered gene expression was assessed, using immunocytochemistry (Figure 3.15 B). Immunocytochemistry revealed that AAV-Dlx-mCherry-ΔCre and AAV-Dlx-mCherry-Cre viruses transduced GABAergic neurons with a specificity of 81.6 ± 5.5 % and 79.6 ± 4.4 %, respectively. The results confirm that these viruses serve as a reliable tool for induction of RIM3 cKO and corresponding WT in GABAergic neurons.

Cortical RIM3flox neurons were treated with the before tested Dlx-Cre and Dlx-ΔCre viruses to yield inhibitory-specific RIM3 KO and corresponding WT cells. Recordings were performed on DIV14 and from DIV18-20 to investigate network properties at different stages of development (Figure 3.15 A).

Upon deletion of RIM3 in inhibitory neurons, we found a strong transformation of neuronal activity from synchronized network bursting to mostly asynchronized tonic firing. This difference becomes evident in exemplary raw traces of GABAergic WT and cKO neurons (Figure 3.15 C) as well as representative ISI histograms. The bimodal ISI distribution typical for activity dominated by bursts could only be observed in WT; KO neurons displayed a quite different, even distribution of ISIs, representing a high degree of tonic firing (Figure 3.15 D).

RIM3 ablation in GABAergic neurons significantly reduced the networks' synchronicity by 48.3 ± 7.9 % compared to WT on DIV14 (area under norm. cross-correlation: 0.47 ± 0.06 and 0.25 ± 0.06 in WT and KO, respectively, Figure 3.15 F). On the other DIVs synchronicity was consistently decreased by ~30 – 40 %, but the difference was not significant.

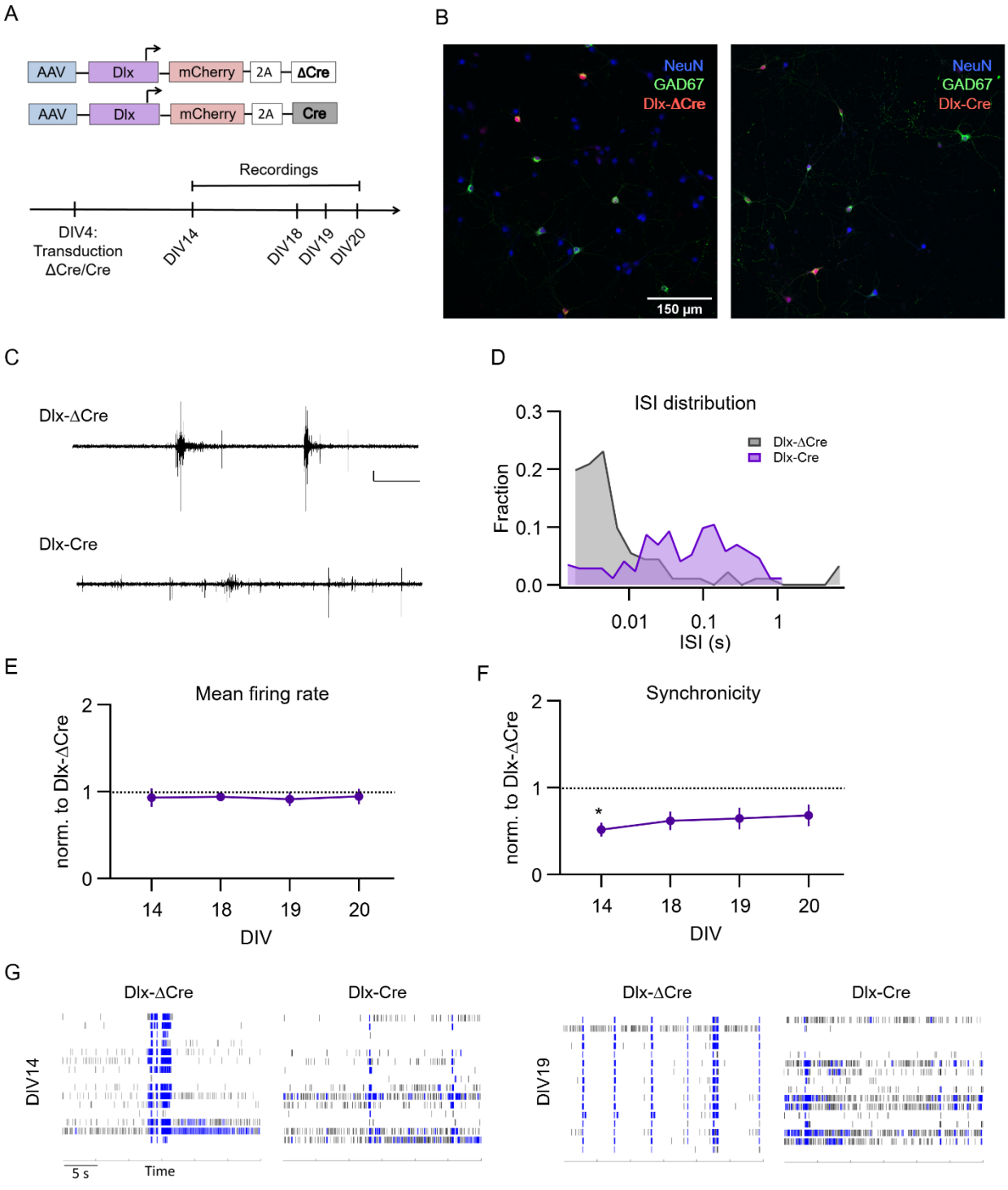

Figure 3.15: RIM3 cKO in inhibitory neurons disrupts network synchronization at low density. (A) Lentiviral vectors expressing ΔCre and Cre under inhibitory-specific Dlx-promoter. RIM3flox cortical neurons were seeded at 2000 cells/mm² and transduced on DIV4 with Dlx-ΔCre/Cre viruses to yield WT and cKO in GABAergic neurons, respectively. MEA recordings were performed on DIV14 and DIV18-20. **(B)** Representative confocal images of lenti-virally delivered ΔCre and Cre expression (red) in GABAergic primary neurons, specifically. Gad67 (green) labels GABAergic neurons, NeuN (blue) labels all neurons. Specificity was assessed by dividing Gad67-

positive transduced neurons by the total amount of transduced neurons. N=3 cultures, n=3 coverslips each. **(C)** Representative raw traces of WT and Dlx-specific cKO neurons on DIV19. Scale bar: 50 µV, 500 ms. **(D)** Representative ISI histogram expressing differential ISI distributions of WT and Dlx-specific cKO neurons. Bimodality indicates temporal clustering into bursts.I**-F)** Mean firing rate **(E)** and synchronicity (area under norm. cross-correlation) **(F)** of Dlx-specific cKO normalized to WT. N= 5 cultures, n=3-4 wells. Data in bar graphs show mean ± SEM. For each culture, data of all wells belonging to one group were averaged and group means of Dlx-specific cKO were normalized to their corresponding WT group means. Mean + SEM were calculated from the resulting normalized values per culture. Statistical significance was assessed using repeated measures two-way ANOVA followed by Holm-Sidak's post-hoc test for multiple comparisons. (* $p < 0.05$). **(G)** Representative raster plots showing 30 s of well-wide neuronal activity of WT and Dlx-specific cKO on DIV14 and DIV19.

Raster plots of well-wide activity from DIV14 and DIV19 underline the substantial difference in network firing pattern between Dlx-specific KO and WT (Figure 3.15 G), with a high degree of frequent, tonic, unsynchronized firing instead of predominance of synchronized network events, which are followed by periods of quiescence. This atypical firing pattern led to inaccurate burst and network burst discrimination by the detection algorithm, therefore data for these parameters are not shown here. Mean firing rates remained unchanged by cKO of RIM3 (Figure 3.15 E).

Taken together, neuronal networks displayed less synchronous firing after knocking out RIM3 in inhibitory neurons.

4 Discussion

4.1 Transcriptomics indicate role of RIM3 in synaptic processes, plasticity and development, without altering protein expression

Transcriptomics of RIM3 KO tissue revealed a variety of genes to be significantly differentially expressed in the thalamus and cortex. In the thalamus, we primarily found genes associated with synaptic transmission, regulation of ion channels, synapse structure and synaptic plasticity. This indicates that RIM3 might be involved in similar processes as α-RIMs.

When taking a closer look at the differentially regulated synaptic genes, we found that various active zone molecules were downregulated upon RIM3 KO. Interestingly, the genes of the large RIM isoforms *Rims1* and *Rims2* showed a significant downregulation, indicating that RIM3 might play a role in promoting α-RIM expression. Moreover, the genes coding for the AZ scaffolding proteins Liprin-α2, Bassoon, Piccolo and ELKS2, the calcium sensor Synaptotagmin-1, as well as SNARE-complex members Synaptobrevin and SNAP-25 showed reduced expression upon RIM3 KO. Many of the mentioned molecules have been described as RIM1/2 binding partners (Mittelstaedt et al., 2010; Ohtsuka et al., 2002; Schoch et al., 2002; Shibasaki et al., 2004; Takao-Rikitsu et al., 2004), which may suggest similar interaction patterns between RIM3 and α-RIMs. Additionally, we found different subunits of voltage-gated calcium channels (VGCC) to be differentially expressed, including VGCC β4-subunit, which has been described as a binding partner of the α-RIM C2B-domain (Mittelstaedt et al., 2010). Therefore, it might be possible that RIM3 is involved in regulating presynaptic function and neurotransmitter release through modulation of α-RIM function by interaction with its binding partners and/or through positive regulation of their expression. This would be consistent with earlier mentioned studies using HEK293T cells and PC12 cells, suggesting a role of RIM3 in promoting VGCC trafficking to the plasma membrane (Picher et al., 2017), altering VGCC kinetics, regulating neurotransmitter release and the number of docked synaptic vesicles at the AZ (Uriu et al., 2010).

However, the spectrum of differentially regulated genes after RIM3 deletion was not limited to AZ components. The additional differential expression of PSD molecule *Shank3*, different potassium channel subunits, GABA receptors and glutamate receptors indicates additional postsynaptic functions of RIM3, which is consistent with previous studies (Liang et al., 2007).

Another significantly downregulated synaptic gene was *Neurexin1,* a presynaptic cell adhesion molecule highly relevant for synaptogenesis and synapse stability during plasticity and development (Dean and Dresbach, 2006; Südhof, 2008). Among the genes with the strongest differential expression, we found several other DEGs involved in developmental processes, such as neuronal migration and differentiation, neurite outgrowth, axon targeting and synaptogenesis. Many of those genes were transcription factors (*Pax7, Pax3, Socs2, Ebf3, Ebf2*). These observations are underlined by the GO analysis showing a significant association with transcription factor activity and developmental processes. These results might point in the direction of the neuronal growth deficits described by Alvarez-Baron et al. (2013) and might offer possible explanations for the observed effects.

In the cortex however, the number of DEGs was substantially lower than in the thalamus (63 vs. 1028 DEGs), changes in the transcriptome were less specific and differences in expression were generally lower. This is probably due to the fact that RIM3 is expressed in fewer cells in the cortex compared to the thalamus (see Introduction). The low number of DEGs might also be a possible reason why GO analysis only detected one significantly enriched GO term. The downregulation of AZ molecules in the thalamic transcriptome was similarly not reflected in the cortex, nor did we find other differentially regulated synaptic genes, apart from upregulated *Homer1*, encoding a postsynaptic scaffolding protein at excitatory synapses (Ulrich, 2002).

Instead, we observed differential expression of several genes that function as so-called immediate early genes in activity-dependent regulation of synaptic strength. Long-term adaptations of synaptic properties in response to neuronal activity are partly mediated by changes in gene transcription, to enable the synthesis of new proteins carrying out structural and functional synaptic modifications (Yap and Greenberg, 2018). Immediate early genes (IEG) are genes that get rapidly activated in the nucleus upon external stimuli.

Most of them encode transcription factors that then induce the expression of specific clusters of downstream targets, so-called late response genes. These targets can be other transcriptional regulators or cell-type specific effector molecules, that regulate cellular processes at synaptic sites such as postsynaptic receptor expression, dendritic spine formation, synaptogenesis, etc.. Many IEGs and their downstream targets have been shown to be involved in memory formation, learning, developmental processes, regulation of the E-I balance and different forms of neuronal plasticity (Marballi and Gallitano, 2018; West and Greenberg, 2011; Kim et al., 2018b; Yap and Greenberg, 2018). In the cortex we observed differential expression of the well-established IEGs *Npas4* and *Egr3* upon RIM3 KO. Downregulated *Npas4* has been shown to be involved in the homeostatic regulation of synapse number and function to decrease excitability (Fu et al., 2020; Spiegel et al., 2014; Kim et al., 2018b; Shan et al., 2018), while the upregulation of *Egr3* plays a role in the induction of hippocampal LTP and LTD, learning and memory (O'Donovan et al., 1999; Li et al., 2007; Marballi et al., 2022). Abovementioned upregulated *Homer1* encodes an excitatory scaffolding protein that links postsynaptic mGluR activation to intracellular responses. Its splicing variant Homer1a, however, is also considered an IEG since it is rapidly activated by neuronal activity and subsequently exerts homeostatic downregulation of excitatory synapse function (Heavner et al., 2021; Hu et al., 2010; Ulrich, 2002). Interaction between *Npas4* and *Homer1a* has been described by Shan et al. (2018). In the thalamus, downregulation of *Egr1* was prominent, another IEG of the Egr-family, which is involved in the maintenance of LTP and the induction of Arc, PSD-95 and AMPA-receptors upon neuronal stimulation (Duclot and Kabbaj, 2017). This indicates that RIM3 might play a role in plasticity mechanisms through activation of IEGs. As gene transcription takes place in the nucleus, rapid communication between synapses and the nucleus is required for these plasticity-related changes (Lim et al., 2017; Parra-Damas and Saura, 2019). A role of RIM3 in this activity-dependent synapse-to-nucleus signaling has been proposed by Michel in 2015, since RIM3 is present in synapses and the nucleus, exhibits a nuclear localization signal and nuclear export signal, and has been shown to interact with several importins (Michel, 2015), which are relevant for active transport to the nucleus (Lange et al., 2007). These previous findings in combination with the differential expression of many IEGs and the beforementioned transcription factors suggest that RIM3 could be involved in linking changes in synaptic

activity to the resulting adjustments of synaptic strength, by synapse-to-nucleus signaling and the induction of specific transcriptional programs.

Other interesting findings were the high representation of genes involved in the cell cycle oxidative ER stress and cell survival among the most differentially regulated genes, especially in the cortex (*Ccn4, Hspa5, Cdkn1a, Telo2, Dact2*), suggesting a possible role for RIM3 in neuroprotective processes. The already mentioned transcription factor *Npas4* has also been shown to mediate neuroprotection in response to excessive synaptic activity via induction of Synaptotagmin-10 (Woitecki et al., 2016). Regarding the cell type, data from mousebrain.org showed that RIM3 is predominantly expressed in inhibitory interneurons in the cortex, and in excitatory neurons in the thalamus. Consistent with this, GO analysis of the thalamic transcriptome showed a strong association with glutamatergic synapses, while GABAergic synapses were associated to a lesser extent. However, we also observed differential gene expression of a muscarinic acetylcholine receptor (*Chrm2*), serotonin receptor 1B (*Htr1b*), and a monoamine transporter (*Slc29a*) in the thalamus, and upregulation of serotonin receptor 2A (*Htr2a*) in the cortex. These results suggest that RIM3 might have functions in different transmitter systems.

Although we found several interesting candidate genes using transcriptomics, we found no corresponding differential expression on the protein level. Poor mRNA to protein correlation has been reported in multiple studies (Buccitelli and Selbach, 2020; Maier et al., 2009; Perl et al., 2017; Vogel and Marcotte, 2012), many of them describing that changes in the transcriptome resulted in considerably smaller changes on the protein level (Perl et al., 2017; Wang et al., 2014). This is believed to partly result from the fact that protein levels do not solely depend on gene transcription: several biological factors have been proposed to influence the proteome, including mRNA structure, regulation of translation, translation efficiency, ribosomal density and occupancy, post-translational modifications, intrinsic protein stability and protein degradation (Maier et al., 2009). Therefore, it is possible that RIM3 only acts on the transcriptional level without affecting protein abundances. Other possible explanations for mRNA-protein-mismatch have been suggested to result from technical limitations and measurement errors of mass spectrometry: mass spectrometry has been reported to be much more sensitive to noise than RNA Seq and to require higher expression levels, since it does not include

amplification of the molecules and the number of peptides matched to a protein is limited. This results in a suboptimal detection of low-abundance proteins, especially in complex biological samples (Gygi et al., 2002; Kim et al., 2018a; Perl et al., 2017; Wang et al., 2014). Since RIM3 is not expressed in all cells of the analyzed tissue and the proteome of a whole brain area creates a highly complex background, possible changes in downstream targets of RIM3 might be below the detection threshold of mass spectrometry or might require a much higher number of biological replicates, resulting in the lack of differentially expressed proteins in our samples. Protein degradation during sample preparation or sample processing might also play a role.

Whether the lack of differentially expressed proteins in our experiments is a result of biological mechanisms, such as post-translational modifications, or methodological limitations remains unclear.

4.2 MEA culture density influences functional network maturation and connectivity

To assess functional consequences of RIM3 loss on electrophysiological network activity, we first had to establish and optimize plating and recording conditions for multi-electrode arrays (MEA). In our MEA optimization experiments, we showed that cells begin to adhere and form networks at a minimum seeding density of 2000 cells/mm². Furthermore, we found that the electrophysiological properties of neuronal networks formed by neurons seeded at low density (2000 cells/mm²) and high density (8000 cells/mm²) differ regarding firing frequencies, firing patterns and synchronicity suggesting that neuronal density may play a role in functional network maturation.

The higher firing frequencies we observed in high-density cultures on MEA might be a result of increased activity in individual neurons but are more likely to originate from technical limitations: MEA electrodes record action potentials from neurons growing in their proximity, therefore a higher neuronal density can lead to the recording of action potentials from a larger number of neurons, resulting in higher firing frequencies. Therefore, the mean firing rate in the context of culture density should be viewed critically.

The firing pattern, however, can give more valuable information about the structure and development of a neuronal network. Several studies have described that cultured neurons exhibit different patterns of activity as they undergo developmental changes (Chiappalone et al., 2006; Fuchs et al., 2007; Muramoto et al., 1993; van Pelt et al., 2004). In MEA recordings with cultured cortical neurons, activity has been shown to change from sparse, isolated or tonic firing during the first week *in vitro* to more synchronized bursting around DIV14, and a further synchronization towards the end of the third week *in vitro* with a higher percentage of involved electrodes (Chiappalone et al., 2006; van Pelt et al., 2004). Although our recordings were performed in shorter time periods, the described network development including the transition from spiking to bursting over time becomes visible in the low-density networks. In high-density networks, activity was organized exclusively in highly synchronized network bursts from the beginning of the recording (from DIV14 on) and network bursts were more frequent than in low-density. This indicates that high-density networks might mature faster than networks grown at lower densities. A correlation between culture density and the time course of bursting behavior has been described by Wagenaar et al. in 2006. The study reported that synchronized bursting in cultures grown at 600 cells/mm² was established later than in cultures grown at 2500 cells/mm². This functional network maturation has been shown to correlate with increasing synapse density: synapse number is very low during the first week *in vitro* but rapidly increases until the end of the third week *in vitro*, after which synapse number starts to decrease again (Cullen et al., 2010; Ichikawa et al., 1993; Muramoto et al., 1993). Especially the increase in glutamatergic interconnections has been suggested to mediate emerging synchronicity (Chiappalone et al., 2006; Scharfman, 2007). Therefore, it is likely that the observed early and complete synchronization in our high-density networks is caused by an extreme number of synaptic connections in these cultures. This is supported by studies reporting that synaptogenesis, dendritic spine formation, neurite outgrowth and dendritic tree complexity positively correlate with culture density (Banker and Cowan, 1977; Cullen et al., 2010; Ivenshitz and Segal, 2010; van den Pol et al., 1998). From our results we can therefore conclude, that increasing network synchronization over time serves as a functional read-out for connectivity and network development in our experiments.

It should be noted that in studies comparing effects of cell densities, much lower densities are referred to as “low-density” than in our experiments (100 - 500 cells/mm²) and that a

density of 2000 cells/mm² is often rather considered medium or even high (Cullen et al., 2010; Ito et al., 2010; Wagenaar et al., 2006). Also, for most studies working with MEA experiments, plating densities ranging from 100 – 2500 cells/mm² were used (Ito et al., 2010; Mossink et al., 2021; Serra et al., 2010; Wagenaar et al., 2006). In our study, however, neurons seeded at densities below 2000 cells/mm² did not adhere to the surface and did not allow for network formation and recording of extracellular MEA signals. Therefore, 2000 cells/mm² marked the lowest sufficient density for our experiments. This may originate from plating and culturing conditions, such as plate type and architecture, preparations, cell type, as well as size of the coated area and coating material. Especially the use of different culture medium might have played a role, since serum-free media have been shown to increase survival at low densities (Brewer et al., 1993).

The better comparability with other studies using MEA was one reason for us to focus on 2000 cells/mm² instead of higher densities for the MEA experiments in our study. Apart from this, the hypersynchronized network activity observed at 8000 cells/mm² seemed to be marking an endpoint in connectivity with no opportunities for further development. The evocation of a global response upon every action potential in high-density cultures makes it difficult to see fine changes in firing patterns or contribution of single groups of neurons to network activity. Another disadvantage when considering high-density netwIrks is, that it is nearly impossible to monitor visually the health state of the network prior to or between recordings. On the other hand, recordings of high-density networks exhibit very low variability across experiments (within cultures as well as between cultures). Since we assume our high-density networks to be oversaturated with synapses, plating might always result in the same network structure, leading to very stable firing patterns. Low-density cultures, in contrast, exhibited much more variability in firing patterns as well as visually determinable cell density and network structure. This may result in higher variability in outcomes, leading to the suggestion that higher numbers of experiments are required for reliable MEA experiments at this density. Another phenomenon observed in low-density but not in high-density cultures is that neurons often distribute unevenly, with neurons centering in the middle and growing sparsely around the outer electrodes. Inconsistency of both cell density and distribution has been described as a considerable source of variation in MEA recordings of human iPSC cultures (Mossink et al., 2021).

Therefore, it might be of interest to further optimize culturing conditions for more reliable cell distribution at lower densities.

Taken together, our observations allow us to use progressing network synchronization over time as a functional read-out for network development and connectivity. Furthermore, the characterization of networks at high and low density enables us to investigate RIM3 deletion under different network conditions, regarding firing patterns and connectivity.

4.3 Homeostatic network plasticity was inducible with TTX on MEA

Silencing with TTX has been shown to induce homeostatic plasticity in neurons in many studies (Burrone et al., 2002; Delvendahl and Müller, 2019; Ibata et al., 2008; Nakayama et al., 2005; Turrigiano et al., 1998). While most of these studies focused on changes in individual neurons using techniques such as patch-clamp, inducing homeostatic plasticity with TTX on MEA has been described in only a few studies and with different outcomes: Eposti et al., 2007 and Zhou et al., 2009 reported increased firing rates, network burst frequencies and synchronization following the removal of TTX. Others only observed a restoration of activity back to baseline after washout, but with no further effects (Negri et al., 2020; Xu et al., 2017). These diverging results probably stem from differences in the experimental design, especially regarding treatment duration and time between removal of the drug and recording.

In our experiments, we observed a tendency towards increased burst durations and mean firing rates after washout of TTX, but the differences were statistically not significant. This might be due to the high variability observed in MEA experiments, especially in low density cultures. Our analysis testing if homeostatic plasticity was altered in RIM3 KO vs. WT neurons revealed a significant increase in burst durations in the WT condition though, validating the effect of global silencing with TTX on burst duration. Mean firing rates, however, were not increased consistently. Prolonged bursting has not been described as an effect of TTX but appears reasonable as a result of homeostatic upregulation: Previous studies investigating the mechanisms behind burst generation and termination have suggested the depletion of presynaptic vesicle pools as a limiting factor of burst durations (Cohen and Segal, 2011; Staley et al., 1998), alongside with postsynaptic glutamate

receptor desensitization (Arai and Lynch, 1998) during ongoing bursting. Since homeostatic responses to silencing include increases of the release-ready vesicle pool (Delvendahl and Müller, 2019) as well as enhanced postsynaptic glutamate receptor expression (Ibata et al., 2008; Watt et al., 2000), delayed burst termination can be considered as a result of homeostatic upregulation.

Conversely to the studies of Eposti et al., 2007 and Zhou et al., 2009 who reported increased network burst frequency and synchronization after TTX treatment, both parameters were not significantly changed in our experiments. Interestingly, network burst frequency rather displayed a tendency towards decreased values after silencing. A possible explanation might be the inverse relationship of burst duration and burst frequency, that has been described in several studies (Boehler et al., 2012; Cohen and Segal, 2011; Wichmann and Soares, 2006). The sustained depolarization of prolonged bursting might lead to increased sodium channel inactivation in the network (Basarsky and French, 1991; Connors and Gutnick, 1990), which in turn prolongs the refractory post-burst period and therefore reduces burst frequencies. While single-electrode burst frequency was not influenced though, only the occurrence of synchronized bursts on the network level seemed to be affected. The density we used is comparable to the densities used in the mentioned studies, but other factors might have played a role in the unexpected reduction of network burst frequency, such as culture age, ratio of excitatory and inhibitory neurons or increased cell death upon TTX treatment. However, these diverging results underline the complexity of homeostatic plasticity on the network level and the need for further research.

Based on our results and the well-established effect of TTX in neurons, we interpret the increased burst durations as a result of homeostatic upregulation in our neuronal networks.

4.4 Effects of Gabazine treatment suggest that GABAergic activity opposes network synchronization

Additionally, we wanted to characterize the immediate and long-term effects of disruption of GABA-mediated inhibition on neuronal network activity, using the $GABA_A$ antagonist

Gabazine. Thereby, we wanted to indirectly investigate the role of GABAergic signaling in the firing patterns of our networks, as well as assess if Gabazine treatment was sufficient to chemically induce homeostatic plasticity.

The disruption of fast GABA-mediated inhibition with Gabazine or other $GABA_A$ antagonists (such as bicuculline or picrotoxin) has been shown to result in increased firing rates and synchronized, epileptiform activity in neuronal cultures, as described in several studies (Arnold et al., 2005; Ahtiainen et al., 2021; Jewett et al., 2018; Mapelli et al., 2016; Pegoraro et al., 2010). Additionally, the neuronal hyperactivity elicited by $GABA_A$ antagonists has been reported to induce homeostatic downregulation of activity (de Gois et al., 2005; Doyle et al., 2010; Turrigiano et al., 1998). Conversely to the existing literature, Gabazine did not lead to increased firing rates in our experiments. A possible reason might be the use of different concentrations: while most of the mentioned studies with Gabazine used 10 – 50 µM, we worked with 1 µM to induce finer, more physiological changes of the E-I balance, instead of blocking GABA transmission and functional inhibition completely. Low Gabazine concentrations, starting from 200 nM, have been shown to affect phasic GABA-mediated inhibition, while blockade of tonic inhibition required much higher concentrations (Stell and Mody, 2002). This dose-dependent effect on different receptor subtypes and modes of inhibition might explain why 1 µM, although used in studies and considered an active concentration (Fan et al., 2019; Gullo et al., 2009), did not lead to a distinct global increase in firing rates but predominantly changed firing patterns.

The most prominent finding in our experiments was an immediate and persisting network synchronization, which is consistent with the above-mentioned literature and therefore confirms the existence of a functional GABAergic system in our networks. The increased network synchronicity under $GABA_A$ blockade furthermore suggests that network synchronization is promoted by excitatory activity in our networks, and GABAergic signaling is an opposing force to said synchronization. Previous studies have similarly suggested increased synchronicity as a result of hyperexcitability (Iida et al., 2018; Pegoraro et al., 2010; Que et al., 2021), although the contribution of excitation and inhibition to the maintenance of neuronal synchronicity is not fully understood. *In vivo*, pathological synchronizations such as epileptic seizures are widely considered to stem

from hyperexcitability due to lack of GABAergic inhibition (Liu et al., 2014; Treiman, 2001; Scharfman, 2007). On the other hand, GABAergic interneurons are believed to mediate cortical oscillations, a physiological form of synchronicity, by targeting and hyperpolarizing whole groups of excitatory neurons at once (Cobb et al., 1995; Gonzalez-Burgos et al., 2010; Mann and Paulsen, 2007). This indicates that synchronicity can be mediated by different, interplaying mechanisms and that excitation and inhibition have no simple, direct relationship to this matter (Scharfman, 2007). It should be noted that $GABA_A$ blockade not only disinhibits glutamatergic neurons, but also blocks inhibition on GABAergic neurons and increases their activity, influencing the effect on network activity. Additionally, different modes of inhibition, ion gradients, feedback loops and the high complexity of local microcircuitry might add difficulty to interpreting synchronicity with respect to the E-I balance. Therefore, it should be stated that the role we ascribe to GABAergic signaling in synchronization of our networks is based on a simplified model.

The network synchronization persisted relatively unchanged during the 24 hours of treatment, and synchronicity did not significantly differ from control levels after washout, which indicates that the treatment did not lead to homeostatic downregulation in these experiments. Regarding network burst frequencies, however, we unexpectedly observed a significant network burst suppression 24 hours after Gabazine application, although immediate effects on network burst frequency were very variable and did not point in any specific direction. It is possible that this delayed reduction in network burst frequency might be a sign of homeostatic downregulation upon increased excitability in the form of hypersynchronized network activity. However, this seems to be unlikely because we would expect even lower values after removal of $GABA_A$ blockade, which is not the case. Another possibility is that repetitive activation of the whole network at once leads to more global refractory periods in which neurons are less sensitive to incoming inputs, therefore reducing the network burst frequency. Other factors influencing how cultured neurons respond to seizurogenic compounds have been proposed to be the ratio of excitatory and inhibitory subpopulations, determining baseline excitability and GABAergic receptor density, as well as the number of astrocytes in culture (Tukker et al., 2018).

Taken together, these results can give us valuable insights into the role of GABAergic signaling in our cultures and show that network synchronicity can be interpreted as a shift

toward excitation. Inducing homeostatic plasticity with Gabazine failed in our experiments and would possibly require the use of higher concentrations.

4.5 Homeostatic plasticity on the network level is not dependent on RIM3

Based on the well-established role of α-RIMs in different forms of synaptic plasticity (Castillo et al., 2002; Müller et al., 2012; Müller et al., 2022; Südhof, 2012), we were particularly interested in whether RIM3 plays a role in synaptic plasticity too, specifically homeostatic plasticity. Subjecting RIM3 WT and KO neurons to TTX treatment in the manner established earlier did not lead to changes in the induction of homeostatic plasticity. These results suggest that homeostatic plasticity on the network level is not dependent on RIM3.

In general, it should be stated that the rather low spatial resolution of MEAs allows for reliable investigation of action potentials, but subthreshold potentials at individual synapses are not detectable. Therefore, it is suited for a quite broad approach, assessing neuronal activity mainly on the network level. However, a considerable number of events in synaptic plasticity are linked to altered amplitudes of synaptic potentials, that are often not sufficient to induce action potential firing (Massobrio et al., 2015). Although our results suggest that RIM3 is unlikely to participate in homeostatic plasticity mechanisms, we cannot exclude the possibility that RIM3 deletion leads to more subtle changes in homeostatic regulation of synaptic properties than can be detected by MEA. The investigation of such would require different methods that focus on individual neurons or synapses and could therefore not be addressed in this study.

4.6 RIM3 exerts different functions in spontaneous activity, depending on network connectivity

When observing the development of spontaneous activity in RIM3 WT and KO neuronal networks at different culture densities, we found that the effects of RIM3 deletion differed between low-density and high-density cultures: while in low-density we only observed a slight increase in synchronicity in RIM3 KO, high-density cultures displayed a strongly

decreased network excitability with a reduction in firing, bursting and network bursting by approximately 40 – 50 %.

This poses not only the question why the strong reduction in network activity at high density is missing in low-density cultures, but further why the effects seem to point in opposite directions and affect different parameters. Our results suggest that RIM3, in the physiological condition, might get activated under specific circumstances and exert different functions, here apparently depending on network connectivity.

What constitutes the difference between our low-density and high-density cultures was mainly the degree of synchronized activity and the assumed number of synaptic connections. At a high level of synapse density and hypersynchronized activity, RIM3 apparently seems to function as a positive regulator of network activity, as the strong reduction in firing, bursting and network bursting upon RIM3 KO show. Conversely, in cultures exhibiting less synaptic connections and generally less synchronous firing, RIM3 seems to negatively regulate neuronal activity in the form of keeping synchronicity low, since we observed enhanced synchronicity in the absence of RIM3. However, this difference in the low-density condition was much less severe than the effects of RIM3 deletion in the high-density condition. The regulation of neuronal network activity is a finely adjusted process, in which mechanisms that potentiate neuronal excitability upon ongoing activity in a use-dependent way are balanced with opposing homeostatic mechanisms that serve to prevent hyperexcitability. Our results suggest, that RIM3 has activity-dependent functions and rather seems to reinforce or stabilize the mode of ongoing activity, than to homeostatically counterbalance it.

RIM3 has been proposed to exert regulatory functions in neuronal activity through synapse-to-nucleus signaling and subsequent activity-dependent gene transcription by Michel, 2015. Our transcriptomics results similarly hinted towards participation of RIM3 in activity-dependent induction of gene expression. Depending on the level of synapse density and the firing pattern, it is possible that RIM3 might induce diverging transcriptional programs, that lead to different long-term changes in the neuronal network. One possibility might be through adjustment of functional synapses, with RIM3 promoting the maintenance or formation of excitatory synapses at already high synapse density, while promoting synapse elimination at lower levels. Other possibly targeted mechanisms may

include the induction of increases or reductions in postsynaptic receptor expression, intracellular signaling efficiency or ratio of GABAergic vs glutamatergic firing. Since α-RIMs are well-known to regulate neuronal activity through modulation of neurotransmitter release (Calakos et al., 2004; Han et al., 2011; Schoch et al., 2002), and transcriptomics data pointed towards a similar presynaptic function of RIM3, it is possible that RIM3 influences gene expression or interacts with active zone components in an activity-dependent manner, thereby modulating their function.

Another interesting question in this context is how different activation of RIM3 in response to neuronal density and activity can be achieved. One way to induce the activation or deactivation of protein function upon external stimuli, is through post-translational modifications, especially phosphorylation (Nishi et al., 2011; Xin and Radivojac, 2012). Recently, it has been discovered that phosphorylation of RIM1 at different sites can potentiate neurotransmitter release and mediates RIM1-dependent homeostatic plasticity (Müller et al., 2022). A similar mechanism might enable activity-dependent activation of RIM3: CDK5 and CaMKII have been proposed to phosphorylate RIM3 (Michel, 2015), but the functional relevance has not been assessed.

Activity-dependent function of RIM3, influencing network excitability depending on the level of synchronized activity and connectivity, seemed to be the most reasonable explanation for our results, since it may account for the effects pointing in different directions. However, several other factors might have contributed to the density-dependent effects we observed upon RIM3 deletion. First of all, the occurrence of the strong reduction in network activity in high-density and the absence of it in low-density cultures might be a result of the high variability of low-density cultures. Possible effects of RIM3 deletion might be more consistent and therefore visible at high culture density, since the network structure, connectivity and firing pattern are more stable throughout and within the replicates.

Furthermore, Ito et al., (2010) discussed the possibility that neuronal networks can exhibit different ratios of excitatory and inhibitory subpopulations when seeded at different densities, and Serra et al., (2010) described density-dependent inhibitory regulation of glutamatergic signaling. These effects might have an influence on the consequences of RIM3 absence with respect to network excitability.

Another key feature of high-density vs. low-density cultures was the accelerated network maturation and development. Considering this, there might be a link between our observations and the axonal and dendritic growth deficits described by Alvarez-Baron et al. (2013). As already mentioned, plating neurons at high density has been shown to promote neurite outgrowth and synaptogenesis (Ivenshitz and Segal, 2010; van den Pol et al., 1998; Cullen et al., 2010), leading to fast network maturation. If RIM3 functions in as growth-promoting processes as proposed by Alvarez-Baron et al. (2013), a strong activation under high-density culturing conditions in the wildtype might make the deficits of RIM3 absence more visible or appear at an earlier timepoint. In this way, developmental deficits of RIM3 deletion might be promoted by higher culture density. However, what is questionable about this possibility is the time course: in our experiments, effects appear at DIV19, when the network is already in a mature state and most of the synaptic connections should already be formed. In the mentioned study, axonal and dendritic growth deficits were observed already 48 h after induction of RIM3 knockdown, and reduced synapse density was obtained 10 days after knockdown. Alvarez-Baron et al. (2013) proposed that RIM3 is required for the outgrowth and formation of neurites and synapses, rather than being essential for their maintenance.

Another possibility is that high culture density might pose a survival disadvantage and promote earlier cell death in KO neurons. Transcriptomics of cortical RIM3 KO tissue revealed several DEGs involved in cell survival, and although abundance changes were not reflected on the protein level, there might be a certain vulnerability where deficits only show under specific circumstances. For example, the downregulated transcription factor *Npas4* induces Synaptotagmin-10-mediated protection against neuronal death in response to excessive, epileptiform activity (Woitecki et al., 2016), which may resemble the activity observed in our high-density cultures. Synaptic activity is widely considered beneficial and even necessary for neuronal survival (Ghosh et al., 1994; Heck et al., 2008; Ruijter et al., 1991), but hyperactivity with excessive activation of glutamate receptors has been shown to lead to excitotoxicity and increased neuronal death (Oppenheim, 1991; Waxman and Lynch, 2005; Beal, 1992). Similarly, culture density is promoting cell survival up to a certain point by increasing the availability of neurotrophic factors (Watanabe et al., 1998; Brewer et al., 1993; van den Pol et al., 1998), but when a certain density is exceeded, viability decreases again, possibly by the abovementioned excitotoxicity,

accumulation of proteolytic enzymes or rapid depletion of nutrients in the culture medium (Young et al., 2000). Apart from this, programmed neuronal death partly serves the purpose of regulating neuron numbers (D'Mello, 1998; Oppenheim, 1991), so it is possible that apoptosis is enhanced at high culture density as a compensatory downregulation. As the density used in our high-density networks (8000 cells/mm^2) can be considered uncommonly high for this method it is likely that the abovementioned factors create a suboptimal culture environment, in which possible survival-promoting functions of RIM3 might be missing in the KO condition. Therefore, a possible tendency to lower viability in RIM3-deficient neurons may be potentiated under high-density culturing conditions, causing the reduction in network activity that is absent in low-density cultures. We have tried to rule out deficits in cell survival by subjecting RIM3 WT and KO cultured neurons to cell viability assays. Our experiments show a reduction of viable cells over time in both groups, but we found no significant differences in viability between WT and KO. Although our experiments can exclude a general tendency for impaired survival, this approach misses culture density as a determining factor: the experiments were carried out with a higher cell number but on cover slips (area approximately 114 mm²) instead of the spatially limited MEA electrode area (5 mm²), resulting in a single, much lower density of 200-300 cells/mm² and lacking the specific conditions of the MEA well. Therefore, the experiments are not completely comparable, and it is not possible to draw unequivocal conclusions with respect to the effects we observed with MEA.

Taken together, RIM3 seems to promote neuronal excitability in highly interconnected, synchronized networks and negatively regulates excitability in less interconnected and synchronized networks. While several factors might contribute to these observations, we propose that RIM3 functions in an activity-dependent way, rather reinforcing ongoing activity than homeostatically opposing it. Induction of activity-dependent gene transcription, presynaptic vesicle release and phosphorylation as a molecular switch might play a role. However, the exact cellular mechanisms and which types of neurons mediate these long-term effects remain unclear.

4.7 RIM3 might serve as a negative regulator of both excitatory and inhibitory neuronal function

In the cortex, RIM3 is predominantly expressed in inhibitory interneurons, based on single-cell RNA Seq data from mousebrain.org. Therefore, we were interested in investigating the function of RIM3 separately in excitatory and inhibitory neurons. Since high-density networks might constitute a suboptimal background for examination by MEA as described in Section 1.2 and 1.6, we focused on low-density networks for these experiments. We found an increase in mean firing rates in RIM3 KO cultures, specifically in excitatory neurons, and we observed disrupted synchronicity after inhibitory-specific RIM3 knock-out. The occurrence of effects in both knock-outs indicates that RIM3 plays a role in both types of neurons.

From the previous experiments we already drew the conclusion that RIM3 functions as a negative regulator of neuronal network activity, specifically synchronicity, in low-density cultures, but the contribution of excitatory and inhibitory neurons to this effect was still unclear. When investigating KO of RIM3 in glutamatergic neurons, we found no altered synchronicity, but increased firing rates, which can be interpreted as a shift toward network excitation. From this it can be concluded that RIM3 might function as a negative regulator in excitatory neurons, thereby contributing to the negatively regulating net effect RIM3 apparently has on network activity.

When knocking out RIM3 in GABAergic neurons, the most prominent effect was disrupted network synchronization, without alterations of firing rates. As can be seen in raster plots, activity did not display a typical burst structure, i.e. clustered high-frequency firing separated by periods of quiescence, but rather random, tonic firing at high frequencies. This altered firing pattern, especially the tonic, high-frequency firing, led to inaccurate burst and network burst discrimination by the detection algorithm due to short inter-spike-intervals. Therefore, these two parameters could not be used for this experiment.

In comparison to firing rates, synchronicity is more difficult to interpret in terms of the excitation-inhibition balance. Our earlier experiments with Gabazine, however, have shown that synchronization in our networks is rather mediated by excitatory activity and prevented by GABAergic signaling. The disrupted synchronization we observed under

RIM3 KO in GABAergic neurons might therefore be interpreted as elevated GABAergic activity and a shift toward inhibition, indicating that RIM3 also serves as a negative regulator in inhibitory neurons. It should be stated though that $GABA_A$ blockade is not exactly transferrable to GABAergic neuronal function, since the interplay of excitation and inhibition is highly complex, and it leaves slow, $GABA_B$-mediated inhibition relatively unaffected. However, previous studies using iPSC derived cortical and hippocampal cultures with alternating ratios of excitatory and inhibitory neurons showed that excitatory-rich cultures displayed highly synchronized activity, while inhibitory-rich cultures exhibited more asynchronous activity with a higher degree of random, tonic firing (Iida et al., 2018; Chen and Dzakpasu, 2010), the latter of which is similar to the activity observed in our experiments. It has been proposed that a higher level of GABAergic inhibition reduces the size of functional neuronal clusters, thus leading to the disrupted synchronicity (Chen and Dzakpasu, 2010). This supports the conclusion that RIM3 KO in inhibitory neurons enhances GABAergic activity and RIM3 therefore exerts negatively regulating functions in inhibitory neurons.

The effects of removing negative regulation in both excitatory and inhibitory neurons seem to partly outbalance each other in the ubiquitous KO, resulting in slightly increased network excitability, in the form of enhanced synchronicity. Since the net effect of ubiquitous RIM3 deletion is slightly shifted towards excitation, we might assume that the impact of the excitatory KO on network activity is stronger than the impact of the inhibitory KO, but given the fact that different parameters are affected, this is hard to evaluate. This also poses the question, why the different KO models lead to isolated changes in diverging parameters, suggesting participation in different network functions. From our experimental data we might assume that firing frequencies may be mainly driven by excitatory activity when inhibition is unaffected, while inhibitory activity controls firing patterns. However, the exact interplay of RIM3-mediated effects in excitatory and inhibitory neurons, as well as the relationship between firing frequencies and activity patterns in our experiments, remain unclear.

4.8 General limitations and conclusions

This study serves as a first functional characterization of RIM3 KO and many of the used methods function as screening techniques, rather than to give detailed insights into cellular mechanisms. The results presented here may therefore form a basis on which further research can be conducted.

In this study, we aimed to assess functional consequences of RIM3 inactivation on neuronal activity on the network level. Multielectrode arrays are a useful tool to investigate network activity, development and plasticity, making them highly suited for our approach, but they do not address the underlying mechanisms on the level of individual neurons or synapses. Therefore, it is still unclear through which mechanisms the changes observed under RIM3 KO are achieved. In accordance with α-RIM function, it is possible that the regulation of presynaptic neurotransmitter release plays a role. It would be interesting to investigate if RIM3 deletion alters presynaptic release probabilities of glutamatergic and GABAergic neurons, utilizing techniques such as FM dyes, iGluSnFR and its inhibitory equivalent, iGABASnFR. Other possibly affected mechanisms might include postsynaptic alterations, which can be addressed both morphologically and functionally with immunostainings of postsynaptic receptors and measurement of mEPSC amplitudes, respectively. Impaired dendritic arborization, changes in synapse density and a role in activity-dependent synapse-to-nucleus signaling should also be considered. For the investigation of these possibilities, further research and employment of different methods would be necessary.

Another interesting but yet unexplained observation is that most of the changes occurred on DIV19, at a rather late stage of development, where the majority of synaptic connections should already be formed. It is possible that synaptic pruning might play a role in the observed effects. For further research, it would be interesting to perform experiments with slices from RIM3 KO and WT animals at different ages to investigate the effects at different developmental stages *in vivo*. Furthermore, the underlying mechanisms by which culture density influences the effects of RIM3 deficiency is another question that needs to be addressed in further research.

What are the functional implications of our results? Previous studies have described an association of RIM3 with schizophrenia (Weidenhofer et al., 2006), as well as autism (Kumar et al., 2010), but the underlying mechanisms remain unclear. From our experiments, we concluded that RIM3 participates in maintaining the E-I balance in an activity-dependent manner and seems to have a role in mediating network synchronicity. Disturbances of the E-I balance have been proposed to underly neurodiversities such as schizophrenia and autism (Sohal and Rubenstein, 2019; Yizhar et al., 2011), and judging from our results it is possible that loss or mutations of RIM3 may lead to such imbalances *in vivo*. Additionally, in the human brain, physiological network synchronicity in the form of gamma-band oscillations is widely believed to play a major role in cognitive function, perception, learning and memory (Cabral-Calderin and Wilke, 2020; Mably and Colgin, 2018; Miller et al., 2018), and abnormal cortical gamma oscillations have been shown to be involved in the pathogenesis of schizophrenia symptoms (Guan et al., 2022; McNally and McCarley, 2016). Possible participation of RIM3 in the maintenance of an appropriate E-I balance and of cortical oscillatory activity might be a first step in elucidating the link between RIM3 and schizophrenia symptoms.

However, it should be noted that the majority of our experiments were performed with cultured neurons and need to be verified *in vivo*. Neuron cultures constitute a very useful, but simplified system, since it lacks the highly organized and controlled microcircuitry and inputs from other brain areas, as they are present *in vivo*. The much higher complexity makes it difficult to predict implications for living animals or humans and underlines the necessity for further research on this topic.

The brain areas exhibiting the highest RIM3 expression, i.e. cortex and thalamus, are highly involved in cognitive function, perception and information processing (Cassel et al., 2021; Friedman and Robbins, 2022; Saalmann and Kastner, 2009; Wang et al., 2008). To get deeper insights into the neuronal function of RIM3 in these brain areas, it would be interesting to examine which neuronal subpopulations express RIM3, to what extent and in which subcellular localizations. Double-immunostainings with cell-type specific markers in brain slices, as well as the generation of region-specific or cell-type specific knockouts could give valuable insights into the function of RIM3 in neuronal processes in the brain.

Taken together, this study was able to give insights into the function of RIM3 in neuronal networks and forms a basis for future experiments on this topic.

5 Summary

Neuronal networks are highly interconnected via specialized units called synapses. During the last years, the large isoforms of the Rab3 interacting molecule (RIM) family, RIM1/RIM2 have been recognized as key components of the presynaptic active zone that play a major role in neurotransmitter release and various forms of synaptic plasticity. However, only little is known about one of the smaller isoforms, RIM3. This study serves as a first functional characterization of a newly generated RIM3 KO mouse line and aims to investigate the role of RIM3 in synapse function, plasticity, spontaneous network activity and the regulation of excitability in neuronal networks.

In transcriptomics and proteomics experiments with thalami and cortices of RIM3 WT and KO mice, we could show that deletion of RIM3 led to various alterations on the mRNA level, without altering the proteome. Our results indicate a potential participation of RIM3 in several synapse-related processes like neurotransmitter release and synaptic plasticity, as well as neurodevelopmental processes. Several transcriptional alterations also point towards a role in synapse-to-nucleus signaling by influencing activity-dependent gene transcription. As protein levels remained unaltered, we assume that RIM3 operates mainly via transcriptional modulation.

To explore neuronal activity on the network level, multielectrode arrays (MEA) were established in our lab. While optimizing recording conditions, culture density emerged as a critical factor influencing network behavior and maturation. High-density cultures exhibited completely synchronized activity from early on, contrasting with the gradual synchronization observed in low-density cultures. Additionally, we established an approach for testing for homeostatic plasticity on the network level, using TTX. Treatment with $GABA_A$-blocker Gabazine did not induce homeostatic plasticity but led to highly synchronized neuronal activity, indicating a counteractive role of GABAergic activity in network synchronization.

Assessing the functional consequences of RIM3 deletion using MEA, we found no differences in the induction of homeostatic plasticity between RIM3 KO and WT cultures. These results indicate that homeostatic plasticity on the network level is not dependent on RIM3.

However, significant alterations in spontaneous network activity over time were observed at different culture densities, with RIM3 deletion strongly reducing network activity in high-density networks while enhancing synchronicity in low-density networks. This suggests a dual role of RIM3 with promoting excitability in highly synchronized networks and restraining it in less synchronized ones, possibly through activity-dependent transcriptional mechanisms.

To attribute possible effects on network activity to cellular subtypes, RIM3 KO was induced separately in glutamatergic and GABAergic neurons in low-density networks. Loss of RIM3 in glutamatergic neurons showed increased firing rates, while RIM3 deletion in GABAergic neurons led to disrupted network synchronization. Our findings indicate that at low densities, RIM3 might serve as a negative regulator of excitability in glutamatergic as well as GABAergic neurons.

Taken together, the results of this study provide new insights into the neuronal functions of RIM3 and form the basis for future studies on the precise understanding of RIM3's role in regulating network excitability, with possible implications for the pathogenesis of neurological conditions, such as epilepsy or schizophrenia.

6 List of Figures

7 References

Adamsen D, Ramaekers V, Ho HTB, Britschgi C, Rüfenacht V, Meili D, et al. Autism spectrum disorder associated with low serotonin in CSF and mutations in the SLC29A4 plasma membrane monoamine transporter (PMAT) gene. Mol Autism 2014; 5: 43–53

Ahtiainen A, Genocchi B, Tanskanen JMA, Barros MT, Hyttinen JAK, Lenk K. Astrocytes exhibit a protective role in neuronal firing patterns under chemically induced seizures in neuron–astrocyte co-cultures. Int J Mol Sci 2021; 22: 12770

Alvarez-Baron E, Michel K, Mittelstaedt T, Opitz T, Schmitz F, Beck H, et al. RIM3γ and RIM4γ are key regulators of neuronal arborization. J Neurosci 2013; 33: 824–839

Arai A, Lynch G. AMPA receptor desensitization modulates synaptic responses induced by repetitive afferent stimulation in hippocampal slices. Brain Res 1998; 799: 235–242

Arefin TM, Mechling AE, Meirsman AC, Bienert T, Hübner NS, Lee HL, et al. Remodeling of Sensorimotor Brain Connectivity in Gpr88-Deficient Mice. Brain Connect 2017; 7: 526–540

Arnold FJL, Hoffmann F, Bengtson CP, Wittmann M, Vanhoutte P, Bading H. Microelectrode array recordings of cultured hippocampal networks reveal a simple model for transcription and protein synthesis-dependent plasticity. J Physiol 2005; 564: 3–19

Arslan A. Extrasynaptic δ-subunit containing GABAA receptors. J Integr Neurosci 2021; 20: 173–184

Augustin I, Rosenmund C, Südhof TC, Brose N. Munc13-1 is essential for fusion competence of glutamatergic synaptic vesicles. Nature 1999; 400: 457–461

Banker GA, Cowan WM. Rat hippocampal neurons in dispersed cell culture. Brain Res 1977; 126: 397–425

Basarsky TA, French AS. Intracellular measurements from a rapidly adapting sensory neuron. J Neurophysiol 1991; 65: 49–56

Basrai HS, Turbic A, Christie KJ, Turnley AM. Suppressor of Cytokine Signalling 2 (SOCS2) Regulates Numbers of Mature Newborn Adult Hippocampal Neurons and Their Dendritic Spine Maturation. Cell Mol Neurobiol 2017; 37: 899–909

Beal MF. Role of excitotoxicity in human neurological disease. Curr Opin Neurobiol 1992; 2: 657–662

Becherer U, Rettig J. Vesicle pools, docking, priming, and release. Cell Tissue Res 2006; 326: 393–407

Boeckers TM, Bockmann J, Kreutz MR, Gundelfinger ED. ProSAP/Shank proteins - A family of higher order organizing molecules of the postsynaptic density with an emerging role in human neurological disease. J Neurochem 2002; 81: 903–910

Boehler MD, Leondopulos SS, Wheeler BC, Brewer GJ. Hippocampal networks on reliable patterned substrates. J Neurosci Methods 2012; 203: 344–353

Boggs JM. Myelin basic protein: A multifunctional protein. CMLS 2006; 63: 1945–1961

Brewer GJ, Torricelli JR, Evege EK, Price PJ. Optimized Survival of Hippocampal Neurons in B27-Supplemented Neurobasal, a New Serum-free Medium Combination. J Neurosci Res 1993; 35: 567–576

Brose N, Petrenko A, Südhof T, Jahn R. Synaptotagmin: a calcium sensor on the synaptic vesicle surface. Science (1979) 1992; 256: 1021–1025

Buccitelli C, Selbach M. mRNAs, proteins and the emerging principles of gene expression control. Nat Rev Genet 2020; 21: 630–644

Burrone J, O'Byrne M, Murthy VN. Multiple forms of synaptic plasticity triggered by selective suppression of activity in individual neurons. Nature 2002; 420: 414–418

Cabral-Calderin Y, Wilke M. Probing the Link Between Perception and Oscillations: Lessons from Transcranial Alternating Current Stimulation. Neuroscientist 2020; 26: 57–73

Calakos N, Schoch S, Sü TC, Malenka RC. Multiple Roles for the Active Zone Protein RIM1 in Late Stages of Neurotransmitter Release. Neuron 2004; 42: 889–896

Cao X, Tabuchi K. Functions of synapse adhesion molecules neurexin/neuroligins and neurodevelopmental disorders. Neurosci Res 2017; 116: 3–9

Cassel J-C, Ferraris M, Quilichini P, Cholvin T, Boch L, Stephan A, et al. The reuniens and rhomboid nuclei of the thalamus: A crossroads for cognition-relevant information processing? Neurosci Biobehav Rev 2021; 126: 338–360

Castillo PE. Presynaptic LTP and LTD of excitatory and inhibitory synapses. Cold Spring Harb Perspect Biol 2012; 4: a005728

Castillo PE, Schoch S, Schmitz F, Südhof TC, Malenka RC. RIM1a is required for presynaptic long-term potentiation. Nature 2002; 415: 327–330

Chae T, Kwon YT, Bronson R, Dikkes P, Li E, Tsai L-H. Mice Lacking p35, a Neuronal Specific Activator of Cdk5, Display Cortical Lamination Defects, Seizures, and Adult Lethality. Neuron 1997; 18: 29–42

Chagnac-Amitai Y, Connors BW. Horizontal spread of synchronized activity in neocortex and its control by GABA-mediated inhibition. J Neurophysiol 1989; 6: 747–758

Chang S, Trimbuch T, Rosenmund C. Synaptotagmin-1 drives synchronous Ca2+-triggered fusion by C2B-domain-mediated synaptic-vesicle-membrane attachment. Nat Neurosci 2018; 21: 33–40

Chen X, Dzakpasu R. Observed network dynamics from altering the balance between excitatory and inhibitory neurons in cultured networks. Phys Rev E Stat Nonlin Soft Matter Phys 2010; 82: 031907

Chevaleyre V, Heifets BD, Kaeser PS, Südhof TC, Castillo PE. Endocannabinoid-mediated long-term plasticity requires cAMP/PKA signaling and RIM1α. Neuron 2007; 54: 801–812

Chiappalone M, Bove M, Vato A, Tedesco M, Martinoia S. Dissociated cortical networks show spontaneously correlated activity patterns during in vitro development. Brain Res 2006; 1093: 41–53

Ch'ng TH, Martin KC. Synapse-to-nucleus signaling. Curr Opin Neurobiol 2011; 21: 345–352

Chuang SM, Wang Y, Wang Q, Liu KM, Shen Q. Ebf2 marks early cortical neurogenesis and regulates the generation of Cajal-Retzius neurons in the developing cerebral cortex. Dev Neurosci 2012; 33: 479–493

Citri A, Malenka RC. Synaptic plasticity: Multiple forms, functions, and mechanisms. Neuropsychopharmacology 2008; 33: 18–41

Cline H. Synaptogenesis: A balancing act between excitation and inhibition. Curr Biol 2005; 15: 203-205

Cobb SR, Buhl EH, Halasy K, Paulsen O, Somogyi P. Synchronization of neuronal activity in hippocampus by individual GABAergic interneurons. Nature 1995; 378: 75–78

Cohen D, Segal M. Network bursts in hippocampal microcultures are terminated by exhaustion of vesicle pools. J Neurophysiol 2011; 106: 2314–2321

Coleman WL, Bill CA, Simsek-Duran F, Lonart G, Samigullin D, Bykhovskaia M. Synapsin II and calcium regulate vesicle docking and the cross-talk between vesicle pools at the mouse motor terminals. J Physiol 2008; 586: 4649–4673

Connors BW, Gutnick MJ. Intrinsic firing patterns of diverse neocortical neurons. Trends Neurosci 1990; 13: 99–104

Cullen DK, Gilroy ME, Irons HR, Laplaca MC. Synapse-to-neuron ratio is inversely related to neuronal density in mature neuronal cultures. Brain Res 2010; 1359: 44–55

Culotta L, Penzes P. Exploring the mechanisms underlying excitation/inhibition imbalance in human iPSC-derived models of ASD. Mol Autism 2020; 11: 32

Davis GW. Homeostatic signaling and the stabilization of neural function. Neuron 2013; 80: 718–728

Dean C, Dresbach T. Neuroligins and neurexins: Linking cell adhesion, synapse formation and cognitive function. Trends Neurosci 2006; 29: 21–29

Delvendahl I, Müller M. Homeostatic plasticity—a presynaptic perspective. Curr Opin Neurobiol 2019; 54: 155–162

Deng L, Kaeser PS, Xu W, Südhof TC. RIM proteins activate vesicle priming by reversing autoinhibitory homodimerization of munc13. Neuron 2011; 69: 317–331

Dhavan R, Tsai L-H. A Decade of CDK5. Nat Rev Mol Cell Biol 2001; 10: 749–759

Dimidschstein J, Chen Q, Tremblay R, Rogers SL, Saldi GA, Guo L, et al. A viral strategy for targeting and manipulating interneurons across vertebrate species. Nat Neurosci 2016; 19: 1743–1749

D'Mello SR. Molecular Regulation of Neuronal Apoptosis. Curr Top Dev Biol 1998; 39: 187–213

Dobin A, Davis CA, Schlesinger F, Drenkow J, Zaleski C, Jha S, et al. STAR: Ultrafast universal RNA-seq aligner. Bioinformatics 2013; 29: 15–21

Doyle S, Pyndiah S, de Gois S, Erickson JD. Excitation-transcription coupling via calcium/calmodulindependent protein kinase/ERK1/2 signaling mediates the coordinate induction of VGLUT2 and Narp triggered by a prolonged increase in glutamatergic synaptic activity. J Biol Chem 2010; 285: 14366–14376

Drago A, Alboni S, Nicoletta B, de Ronchi D, Serretti A. HTR1B as a risk profile maker in psychiatric disorders: A review through motivation and memory. Eur J Clin Pharmacol 2010; 66: 5–27

Duclot F, Kabbaj M. The role of early growth response 1 (EGR1) in brain plasticity and neuropsychiatric disorders. Front Behav Neurosci 2017; 11: 35–55

Dymecki SM. Flp recombinase promotes site-specific DNA recombination in embryonic stem cells and transgenic mice. Proc Natl Acad Sci 1996; 93: 6191–6196

Eden E, Navon R, Steinfeld I, Lipson D, Yakhini Z. GOrilla: A tool for discovery and visualization of enriched GO terms in ranked gene lists. BMC Bioinformatics 2009; 10: DOI: 10.1186/1471-2105-10-48

Eposti F, Signorini MG, Lamanna J, Gullo F, Wanke E. How do TTX and AP5 affect the post-recovery neuronal network activity synchronization? Annu Int Conf IEEE Eng Med Biol Soc 2007; 3012–3015

Fan J, Thalody G, Kwagh J, Burnett E, Shi H, Lewen G, et al. Assessing seizure liability using multi-electrode arrays (MEA). Toxicol in Vitro 2019; 55: 93–100

Fedtsova N, Quina LA, Wang S, Turner EE. Regulation of the development of tectal neurons and their projections by transcription factors Brn3a and Pax7. Dev Biol 2008; 316: 6–20

Fee C, Banasr M, Sibille E. Somatostatin-Positive Gamma-Aminobutyric Acid Interneuron Deficits in Depression: Cortical Microcircuit and Therapeutic Perspectives. Biol Psychiatry 2017; 82: 549–559

Feng S-W, Chen Y, Tsai W-C, Chiou H-YC, Wu S-T, Huang L-C, et al. Overexpression of TELO2 decreases survival in human high-grade gliomas. Oncotarget 2016; 7: 46056–46066

Ferguson BR, Gao WJ. Thalamic Control of Cognition and Social Behavior Via Regulation of Gamma-Aminobutyric Acidergic Signaling and Excitation/Inhibition Balance in the Medial Prefrontal Cortex. Biol Psychiatry 2018; 83: 657–669

Foss-Feig JH, Adkinson BD, Ji JL, Yang G, Srihari VH, McPartland JC, et al. Searching for Cross-Diagnostic Convergence: Neural Mechanisms Governing Excitation and Inhibition Balance in Schizophrenia and Autism Spectrum Disorders. Biol Psychiatry 2017; 81: 848–861

Fourcaudot E, Dé Ric Gambino F, Humeau Y, Casassus G, Shaban H, Poulain B, et al. cAMP/PKA signaling and RIM1 mediate presynaptic LTP in the lateral amygdala. Proc Natl Acad Sci USA 2008; 105: 15130–15135

Fremeau RT, Troyer MD, Pahner I, Nygaard GO, Tran CH, Reimer RJ, et al. The Expression of Vesicular Glutamate Transporters Defines Two Classes of Excitatory Synapse. Neuron 2001; 31: 247–260

Friedman NP, Robbins TW. The role of prefrontal cortex in cognitive control and executive function. Neuropsychopharmacology 2022; 47: 72–89

Fu J, Guo O, Zhen Z, Zhen J. Essential Functions of the Transcription Factor Npas4 in Neural Circuit Development, Plasticity, and Diseases. Front Neurosci 2020; 14: 603373

Fuchs E, Ayali A, Robinson A, Hulata E, Ben-Jacob E. Coemergence of regularity and complexity during neural network development. Dev Neurobiol 2007; 67: 1802–1814

Gard C, Gonzalez Curto G, Frarma YEM, Chollet E, Duval N, Auzié V, et al. Pax3- and Pax7-mediated Dbx1 regulation orchestrates the patterning of intermediate spinal interneurons. Dev Biol 2017; 432: 24–33

Ghosh A, Carnahan J, Greenberg ME. Requirement for BDNF in Activity-Dependent Survival of Cortical Neurons. Science (1979) 1994; 263: 1618–1623

de Gois S, Schäfer MKH, Defamie N, Chen C, Ricci A, Weihe E, et al. Homeostatic scaling of vesicular glutamate and GABA transporter expression in rat neocortical circuits. J Neurosci 2005; 25: 7121–7133

Goldshmit Y, Walters CE, Scott HJ, Greenhalgh CJ, Turnley AM. SOCS2 Induces Neurite Outgrowth by Regulation of Epidermal Growth Factor Receptor Activation. J Biol Chem 2004; 279: 16349–16355

Gonzalez-Burgos G, Hashimoto T, Lewis DA. Alterations of cortical GABA neurons and network oscillations in schizophrenia. Curr Psychiatry Rep 2010; 12: 335–344

Goold CP, Nicoll RA. Single-Cell Optogenetic Excitation Drives Homeostatic Synaptic Depression. Neuron 2010; 68: 512–528

Goto M, Mizuno M, Matsumoto A, Yang Z, Jimbo EF, Tabata H, et al. Role of a circadian-relevant gene NR1D1 in brain development: Possible involvement in the pathophysiology of autism spectrum disorders. Sci Rep 2017; 7: 43945

Guan A, Wang S, Huang A, Qiu C, Li Y, Li X, et al. The role of gamma oscillations in central nervous system diseases: Mechanism and treatment. Front Cell Neurosci 2022; 16: 202–210

Gullo F, Maffezzoli A, Dossi E, Wanke E. Short-latency cross- and autocorrelation identify clusters of interacting cortical neurons recorded from multi-electrode array. J Neurosci Methods 2009; 181: 186–198

Gygi SP, Rist B, Griffin TJ, Eng J, Aebersold R. Proteome Analysis of Low-Abundance Proteins Using Multidimensional Chromatography and Isotope-Coded Affinity Tags. J Proteome Res 2002; 1: 47–54

Hakak Y, Walker JR, Li C, Hung Wong W, Davis KL, Buxbaum JD, et al. Genome-wide expression analysis reveals dysregulation of myelination-related genes in chronic schizophrenia. Proc Natl Acad Sci USA 2001; 98: 4746–4751

Halliday DM, Rosenberg JR, Breeze P, Conway BA. Neural spike train synchronization indices: Definitions, interpretations, and applications. IEEE Trans Biomed Eng 2006; 53: 1056–1066

ben Hamida S, Mendonça-Netto S, Arefin TM, Nasseef MT, Boulos LJ, McNicholas M, et al. Increased Alcohol Seeking in Mice Lacking Gpr88 Involves Dysfunctional Mesocorticolimbic Networks. Biol Psychiatry 2018; 84: 202–212

Han Y, Kaeser PS, Südhof TC, Schneggenburger R. RIM determines Ca2+ channel density and vesicle docking at the presynaptic active zone. Neuron 2011; 69: 304–316

Heavner WE, Lautz JD, Speed HE, Gniffke EP, Immendorf KB, Welsh JP, et al. Remodeling of the Homer-Shank interactome may mediate homeostatic plasticity. Sci Signal 2021; 14: eabd7325

Heck N, Golbs A, Riedemann T, Sun J-J, Lessmann V, Luhmann HJ. Activity-Dependent Regulation of Neuronal Apoptosis in Neonatal Mouse Cerebral Cortex. Cereb Cortex 2008; 18: 1335–1349

Held RG, Kaeser PS. ELKS active zone proteins as multitasking scaffolds for secretion. Open Biol 2018; 8: 170258

Hensch TK, Fagiolini M, Mataga N, Stryker MP, Baekkeskov S, Kash SF, et al. Local GABA Circuit Control of Experience-Dependent Plasticity in Developing Visual Cortex. Science (1979) 1998; 282: 1504–1508

Hu JH, Park JM, Park S, Xiao B, Dehoff MH, Kim S, et al. Homeostatic Scaling Requires Group I mGluR Activation Mediated by Homer1a. Neuron 2010; 68: 1128–1142

Hu Z, Xiao X, Zhang Z, Li M. Genetic insights and neurobiological implications from NRXN1 in neuropsychiatric disorders. Mol Psychiatry 2019; 24: 1400–1414

Huang ZJ, Kirkwood A, Pizzorusso T, Porciatti V, Morales B, Bear MF, et al. BDNF Regulates the Maturation of Inhibition and the Critical Period of Plasticity in Mouse Visual Cortex. Cell Press 1999; 98: 739–755

Huber W, Carey VJ, Gentleman R, Anders S, Carlson M, Carvalho BS, et al. Orchestrating high-throughput genomic analysis with Bioconductor. Nat Methods 2015; 12: 115–121

Huo B, Yang Y, Li M, Wan J, Zhang W, Yu B, et al. Pax3 inhibits Neuro-2a cells proliferation and neurite outgrowth. J Cell Mol Med 2021; 25: 1252–1262

Hyman SE. Neurotransmitters. Curr Biol 2005; 15: R154–R158

Ibata K, Sun Q, Turrigiano GG. Rapid Synaptic Scaling Induced by Changes in Postsynaptic Firing. Neuron 2008; 57: 819–826

Ichikawa M, Muramoto K, Kobayashi K, Kawahara M, Kuroda Y. Formation and maturation of synapses in primary cultures of rat cerebral cortical cells: an electron microscopic study. Neurosci Res 1993; 16: 95–103

Iida S, Shimba K, Sakai K, Kotani K, Jimbo Y. Synchronous firing patterns of induced pluripotent stem cell-derived cortical neurons depend on the network structure consisting of excitatory and inhibitory neurons. Biochem Biophys Res Commun 2018; 501: 152–157

Imig C, Min SW, Krinner S, Arancillo M, Rosenmund C, Südhof TC, et al. The Morphological and Molecular Nature of Synaptic Vesicle Priming at Presynaptic Active Zones. Neuron 2014; 84: 416–431

Ito D, Tamate H, Nagayama M, Uchida T, Kudoh SN, Gohara K. Minimum neuron density for synchronized bursts in a rat cortical culture on multi-electrode arrays. Neuroscience 2010; 171: 50–61

Ivenshitz M, Segal M. Neuronal density determines network connectivity and spontaneous activity in cultured hippocampus. J Neurophysiol 2010; 104: 1052–1060

Iwai R, Tabata H, Inoue M, Nomura K ichiro, Okamoto T, Ichihashi M, et al. A Prdm8 target gene Ebf3 regulates multipolar-to-bipolar transition in migrating neocortical cells. Biochem Biophys Res Commun 2018; 495: 388–394

Jeon WJ, Dean B, Scarr E, Gibbons A. The Role of Muscarinic Receptors in the Pathophysiology of Mood Disorders: A Potential Novel Treatment? Curr Neuropharmacol 2015; 13: 739–749

Jewett KA, Lee KY, Eagleman DE, Soriano S, Tsai NP. Dysregulation and restoration of homeostatic network plasticity in fragile X syndrome mice. Neuropharmacology 2018; 138: 182–192

Jiang DY, Wu Z, Forsyth CT, Hu Y, Yee SP, Chen G. GABAergic deficits and schizophrenia-like behaviors in a mouse model carrying patient-derived neuroligin-2 R215H mutation. Mol Brain 2018; 11: 31

Kaeser PS, Deng L, Wang Y, Dulubova I, Liu X, Rizo J, et al. RIM proteins tether Ca2+ channels to presynaptic active zones via a direct PDZ-domain interaction. Cell 2011; 144: 282–295

Kaizuka T, Takumi T. Postsynaptic density proteins and their involvement in neurodevelopmental disorders. J Biochem 2018; 163: 447–455

Kasahara J, Fukunaga K, Miyamoto E. Activation of Calcium/Calmodulin-dependent Protein Kinase IV in Long Term Potentiation in the Rat Hippocampal CA1 Region. J Biol Chem 2001; 276: 24044–24050

Kilman V, van Rossum MCW, Turrigiano GG. Activity Deprivation Reduces Miniature IPSC Amplitude by Decreasing the Number of Postsynaptic GABA A Receptors Clustered at Neocortical Synapses. J Neurosci 2002; 22: 1328–1337

Kim B, Araujo R, Howard M, Magni R, Liotta LA, Luchini A. Affinity enrichment for mass spectrometry: improving the yield of low abundance biomarkers. Expert Rev Proteomics 2018a; 15: 353–366

Kim S, Kim H, Um JW. Synapse development organized by neuronal activity-regulated immediate-early genes. Exp Mol Med 2018b; 50: 1–7

Kirov G, Rujescu D, Ingason A, Collier DA, O'Donovan MC, Owen MJ. Neurexin 1 (NRXN1) deletions in schizophrenia. Schizophr Bull 2009; 35: 851–854

Kriegstein AR. Synaptic Responses of Cortical Pyramidal Neurons to Light Stimulation in the Isolated Turtle Visual System. J Neurosci 1987; 7: 2488–2492

Kumar RA, Sudi J, Babatz TD, Brune CW, Oswald D, Yen M, et al. A de novo 1p34.2 microdeletion identifies the synaptic vesicle gene RIMS3 as a novel candidate for autism. J Med Genet 2010; 47: 81–90

Lachamp PM, Liu Y, Liu SJ. Glutamatergic modulation of cerebellar interneuron activity is mediated by an enhancement of GABA release and requires protein kinase A/RIM1α signaling. J Neurosci 2009; 29: 381–392

Lallemand Y, Luria V, Haffner-Krausz R, Lonai P. Maternally expressed PGK-Cre transgene as a tool for early and uniform activation of the Cre site-specific recombinase. Transgenic Res 1998; 7: 105–112

Lange A, Mills RE, Lange CJ, Stewart M, Devine SE, Corbett AH. Classical Nuclear Localization Signals: Definition, Function, and Interaction with Importin α. J Biol Chem 2007; 282: 5101–5105

Lazarevic V, Schöne C, Heine M, Gundelfinger ED, Fejtova A. Extensive remodeling of the presynaptic cytomatrix upon homeostatic adaptation to network activity silencing. J Neurosci 2011; 31: 10189–10200

Lê S, Josse J, Rennes A, Husson F. FactoMineR: An R Package for Multivariate Analysis. J Stat Softw 2008; 25: 1–18

Leal G, Comprido D, Duarte CB. BDNF-induced local protein synthesis and synaptic plasticity. Neuropharmacology 2014; 76: 639–656

Lee V, Maguire J. Impact of inhibitory constraint of interneurons on neuronal excitability. J Neurophysiol 2013; 110: 2520–2535

Levinson JN, El-Husseini A. Building excitatory and inhibitory synapses: Balancing neuroligin partnerships. Neuron 2005; 48: 171–174

Li L, Yun SH, Keblesh J, Trommer BL, Xiong H, Radulovic J, et al. Egr3, a synaptic activity regulated transcription factor that is essential for learning and memory. Mol Cell Neurosci 2007; 35: 76–88

Liang F, Zhang B, Tang J, Guo J, Li W, Eng AL, et al. RIM3γ is a postsynaptic protein in the rat central nervous system. J Comp Neurol 2007; 503: 501–510

Liao Y, Smyth GK, Shi W. FeatureCounts: An efficient general purpose program for assigning sequence reads to genomic features. Bioinformatics 2014; 30: 923–930

Lim AFY, Lim WL, Ch'ng TH. Activity-dependent synapse to nucleus signaling. Neurobiol Learn Mem 2017; 138: 78–84

Lima Caldeira G, Peça J, Carvalho AL. New insights on synaptic dysfunction in neuropsychiatric disorders. Curr Opin Neurobiol 2019; 57: 62–70

Lin J, Wang C, Yang C, Fu S, Redies C. Pax3 and Pax7 interact reciprocally and regulate the expression of cadherin-7 through inducing neuron differentiation in the developing chicken spinal cord. J Comp Neurol 2016; 524: 940–962

Linnarsson Lab, 2024: Mouse Brain Atlas. Available from: http://mousebrain.org/adolescent/genesearch.html. (Date: 10.06.2023). Zeisel A et al. Molecular Architecture of the Mouse Nervous System. Cell 2018; 174: 999-1014

Liu YQ, Yu F, Liu WH, He XH, Peng BW. Dysfunction of hippocampal interneurons in epilepsy. Neurosci Bull 2014; 30: 985–998

van Loo KMJ, Rummel CK, Pitsch J, Müller JA, Bikbaev AF, Martinez-Chavez E, et al. Calcium channel subunit α2σ4 is regulated by early growth response 1 and facilitates epileptogenesis. J Neurosci 2019; 39: 3175–3187

van Loo KMJ, Schaub C, Pernhorst K, Yaari Y, Beck H, Schoch S, et al. Transcriptional regulation of T-type calcium channel CaV3.2: Bi-directionality by early growth response 1 (Egr1) and repressor element 1 (RE-1) protein -silencing transcription factor (REST). J Biol Chem 2012; 287: 15489–15501

Lorsch ZS, Hamilton PJ, Ramakrishnan A, Parise EM, Salery M, Wright WJ, et al. Stress resilience is promoted by a Zfp189-driven transcriptional network in prefrontal cortex. Nat Neurosci 2019; 22: 1413–1423

Love MI, Huber W, Anders S. Moderated estimation of fold change and dispersion for RNA-seq data with DESeq2. Genome Biol 2014; 15: 550

Ma C, Su L, Seven AB, Xu Y, Rizo J. Reconstitution of the Vital Functions of Munc18 and Munc13 in Neurotransmitter Release. Science (1979) 2013; 339: 421–425

Mably AJ, Colgin LL. Gamma oscillations in cognitive disorders. Curr Opin Neurobiol 2018; 52: 182–187

Maier T, Güell M, Serrano L. Correlation of mRNA and protein in complex biological samples. FEBS Lett 2009; 583: 3966–3973

Mann EO, Paulsen O. Role of GABAergic inhibition in hippocampal network oscillations. Trends Neurosci 2007; 30: 343–349

Manu KA, Cao PHA, Chai TF, Casey PJ, Wang M. p21cip1/waf1 coordinate autophagy, proliferation and apoptosis in response to metabolic stress. Cancers (Basel) 2019; 11: 1112

Mapelli J, Gandolfi D, Vilella A, Zoli M, Bigiani A. Heterosynaptic GABAergic plasticity bidirectionally driven by the activity of pre- and postsynaptic NMDA receptors. Proc Natl Acad Sci U S A 2016; 113: 9898–9903

Marballi KK, Alganem K, Brunwasser SJ, Barkatullah A, Meyers KT, Campbell JM, et al. Identification of activity-induced Egr3-dependent genes reveals genes associated with DNA damage response and schizophrenia. Transl Psychiatry 2022; 12: 320

Marballi KK, Gallitano AL. Immediate early genes anchor a biological pathway of proteins required for memory formation, long-term depression and risk for schizophrenia. Front Behav Neurosci 2018; 12: 23

Martin M. Cutadapt removes adapter sequences from high-throughput sequencing reads. EMBnet J 2011; 17: 10–12

Massobrio P, Tessadori J, Chiappalone M, Ghirardi M. In vitro studies of neuronal networks and synaptic plasticity in invertebrates and in mammals using multielectrode arrays. Neural Plast 2015; 2015: 196195

McNally JM, McCarley RW. Gamma band oscillations: A key to understanding schizophrenia symptoms and neural circuit abnormalities. Curr Opin Psychiatry 2016; 29: 202–210

Mellacheruvu D, Wright Z, Couzens AL, Lambert JP, St-Denis NA, Li T, et al. The CRAPome: A contaminant repository for affinity purification-mass spectrometry data. Nat Methods 2013; 10: 730–736

Michel K. Neuronal functions of RIM3γ and RIM4γ. Dissertation Rheinische Friedrich-Wilhelms-Universität Bonn, 2015

Michel K, Müller JA, Oprişoreanu A-M, Schoch S. The presynaptic active zone: A dynamic scaffold that regulates synaptic efficacy. Exp Cell Res 2015; 335: 157–164

Miller EK, Lundqvist M, Bastos AM. Working Memory 2.0. Neuron 2018; 100: 463–475

Mittelstaedt T, Alvaréz-Baron E, Schoch S. RIM proteins and their role in synapse function. Biol Chem 2010; 391: 599–606

Monteiro P, Feng G. SHANK proteins: Roles at the synapse and in autism spectrum disorder. Nat Rev Neurosci 2017; 18: 147–157

Moret C, Briley M. The possible role of 5-HT receptors in psychiatric disorders and their 1BrD potential as a target for therapy. Eur J Pharmacol 2000; 404: 1–12

Mossink B, Verboven AHA, van Hugte EJH, Klein Gunnewiek TM, Parodi G, Linda K, et al. Human neuronal networks on micro-electrode arrays are a highly robust tool to study disease-specific genotype-phenotype correlations in vitro. Stem Cell Rep 2021; 16: 2182–2196

Mueser KT, McGurk SR. Schizophrenia. Lancet 2004; 363: 2063–2072

Müller JA. Molecular function of RIM1α: role of phosphorylation sites. Dissertation Rheinische Friedrich-Wilhelm-Universität Bonn, 2020

Müller JA, Betzin J, Santos-Tejedor J, Mayer A, Oprişoreanu AM, Engholm-Keller K, et al. A presynaptic phosphosignaling hub for lasting homeostatic plasticity. Cell Rep 2022; 39: 110696

Müller M, Genç Ö, Davis GW. RIM-binding protein links synaptic homeostasis to the stabilization and replenishment of high release probability vesicles. Neuron 2015; 85: 1056–1069

Müller M, Liu KSY, Sigrist SJ, Davis GW. RIM controls homeostatic plasticity through modulation of the readily-releasable vesicle pool. J Neurosci 2012; 32: 16574–16585

Müller M, Pym ECG, Tong A, Davis GW. Rab3-GAP Controls the Progression of Synaptic Homeostasis at a Late Stage of Vesicle Release. Neuron 2011; 69: 749–762

Muramoto K, Ichikawa M, Kawahara M, Kobayash K, Kuroda Y. Frequency of synchronous oscillations of neuronal activity increases during development and is correlated to the number of synapses in cultured cortical neuron networks. Neurosci Lett 1993; 163: 163–165

Nabavi S, Fox R, Proulx CD, Lin JY, Tsien RY, Malinow R. Engineering a memory with LTD and LTP. Nature 2014; 511: 348–352

Nakayama K, Kiyosue K, Taguchi T. Diminished neuronal activity increases neuron-neuron connectivity underlying silent synapse formation and the rapid conversion of silent to functional synapses. J Neurosci 2005; 25: 4040–4051

Negri J, Menon V, Young-Pearse TL. Assessment of spontaneous neuronal activity In vitro using multi-well multi-electrode arrays: Implications for assay development. eNeuro 2020; 7: 1–27

Nelson S. Temporal Interactions in the Cat Visual System. III. Pharmacological Studies of Cortical Suppression Suggest a Presynaptic Mechanism. J Neurosci 1991; 1: 369–380

Nguyen P v., Woo NH. Regulation of hippocampal synaptic plasticity by cyclic AMP-dependent protein kinases. Prog Neurobiol 2003; 71: 401–437

Nishi H, Hashimoto K, Panchenko AR. Phosphorylation in Protein-Protein Binding: Effect on Stability and Function. Structure 2011; 19: 1807–1815

Nucifora FC, Woznica E, Lee BJ, Cascella N, Sawa A. Treatment resistant schizophrenia: Clinical, biological, and therapeutic perspectives. Neurobiol Dis 2019; 131: 104257

Obi-Nagata K, Temma Y, Hayashi-Takagi A. Synaptic functions and their disruption in schizophrenia: From clinical evidence to synaptic optogenetics in an animal model. Proc Jpn Acad Ser B Phys Biol Sci 2019; 95: 179–197

O'Donovan KJ, Tourtellotte WG, Millbrandt J, Baraban JM. The EGR family of transcription-regulatory factors: progress at the interface of molecular and systems neuroscience. Trends Neurosci 1999; 22: 167–173

Ohtsuka T, Takao-Rikitsu E, Inoue E, Inoue M, Takeuchi M, Matsubara K, et al. CAST: A novel protein of the cytomatrix at the active zone of synapses that forms a ternary complex with RIM1 and Munc13-1. J Cell Biol 2002; 158: 577–590

Oppenheim RW. Cell death during development of the nervous system. Annu Rev Neurosci 1991; 14: 453–501

Panja D, Bramham CR. BDNF mechanisms in late LTP formation: A synthesis and breakdown. Neuropharmacology 2014; 76: 664–676

Parra-Damas A, Saura CA. Synapse-to-Nucleus Signaling in Neurodegenerative and Neuropsychiatric Disorders. Biol Psychiatry 2019; 86: 87–96

Parsons M, Oi VT, Huang C-M, Herzenberg LA. Structural Characterization of Mouse Immunoglobulin Allotypic Determinants (Allotopes) Defined by Monoclonal Antibodies. Immunogenetics 1983; 18: 323–334

Pegoraro S, Broccard FD, Ruaro ME, Bianchini D, Avossa D, Pastore G, et al. Sequential steps underlying neuronal plasticity induced by a transient exposure to gabazine. J Cell Physiol 2010; 222: 713–728

Pelkey KA, Topolnik L, Yuan XQ, Lacaille JC, McBain CJ. State-Dependent cAMP Sensitivity of Presynaptic Function Underlies Metaplasticity in a Hippocampal Feedforward Inhibitory Circuit. Neuron 2008; 60: 980–987

van Pelt J, Wolters PS, Corner MA, Rutten WLC, Ramakers GJA. Long-term characterization of firing dynamics of spontaneous bursts in cultured neural networks. IEEE Trans Biomed Eng 2004; 51: 2051–2062

Perl K, Ushakov K, Pozniak Y, Yizhar-Barnea O, Bhonker Y, Shivatzki S, et al. Reduced changes in protein compared to mRNA levels across non-proliferating tissues. BMC Genomics 2017; 18: 305

Petroff OAC. Book Review: GABA and Glutamate in the Human Brain. Neuroscientist 2002; 8: 562–573

Picher MM, Oprişoreanu AM, Jung SY, Michel K, Schoch S, Moser T. Rab interacting molecules 2 and 3 directly interact with the pore-forming Cav 1.3 Ca2+ channel subunit and promote its membrane expression. Front Cell Neurosci 2017; 11: 160

Pitzer M. The development of monoaminergic neurotransmitter systems in childhood and adolescence. Int J Dev Neurosci 2019; 74: 49–55

van den Pol AN, Obrietan K, Belousov AB, Yang Y, Heller AHC. Early Synaptogenesis In Vitro: Role of Axon Target Distance. J Comp Neurol 1998; 399: 541–560

Que Z, Olivero-Acosta MI, Zhang J, Eaton M, Tukker AM, Chen X, et al. Hyperexcitability and Pharmacological Responsiveness of Cortical Neurons Derived from Human iPSCs Carrying Epilepsy-Associated Sodium Channel Nav1.2-L1342P Genetic Variant. J Neurosci 2021; 41: 10194–10208

Regehr WG. Short-term presynaptic plasticity. Cold Spring Harb Perspect Biol 2012; 4: 1–19

Rijo-Ferreira F, Takahashi JS. Genomics of circadian rhythms in health and disease. Genome Med 2019; 11: 82

Ritchie ME, Phipson B, Wu D, Hu Y, Law CW, Shi W, et al. Limma powers differential expression analyses for RNA-sequencing and microarray studies. Nucleic Acids Res 2015; 43: e47

Ruijter JM, Baker RE, de Jong BM, Romijn HJ. Chronic blockade of bioelectric activity in neonatal rat cortex grown in vitro: Morphological effects. Int J Dev Neurosci 1991; 9: 331–333

Rzhetsky A, Wajngurt D, Park N, Zheng T, Sulzberger JP. Probing genetic overlap among complex human phenotypes. Proc Natl Acad Sci U S A 2007; 104: 11694–11699

Saalmann YB. Intralaminar and medial thalamic influence on cortical synchrony, information transmission and cognition. Front Syst Neurosci 2014; 8: 83

Saalmann YB, Kastner S. Gain control in the visual thalamus during perception and cognition. Curr Opin Neurobiol 2009; 19: 408–414

Scharfman HE. The Neurobiology of Epilepsy. Curr Neurol Neurosci Rep 2007; 7: 348–354

Schoch S, Castillo PE, Jok T, Mukherjee K, Geppert M, Wang Y, et al. RIM1a forms a protein scaffold for regulating neurotransmitter release at the active zone. Nature 2002; 415: 321–326

Schoch S, Gundelfinger ED. Molecular organization of the presynaptic active zone. Cell Tissue Res 2006; 326: 379–391

Serra M, Guaraldi M, Shea TB. Inhibitory neurons modulate spontaneous signaling in cultured cortical neurons: Density-dependent regulation of excitatory neuronal signaling. Phys Biol 2010; 7: 026009

Shan W, Nagai T, Tanaka M, Itoh N, Furukawa-Hibi Y, Nabeshima T, et al. Neuronal PAS domain protein 4 (Npas4) controls neuronal homeostasis in pentylenetetrazole-induced epilepsy through the induction of Homer1a. J Neurochem 2018; 145: 19–33

Sheng Z-H, Westenbroek RE, Catterall WA. Physical link and functional coupling of presynaptic calcium channels and the synaptic vesicle docking/fusion machinery. J Bioenerg Biomembr 1998; 30: 335–345

Shibasaki T, Sunaga Y, Fujimoto K, Kashima Y, Seino S. Interaction of ATP Sensor, cAMP Sensor, Ca2+ Sensor, and Voltage-dependent Ca2+ Channel in Insulin Granule Exocytosis. J Biol Chem 2004; 279: 7956–7961

Singer W. Synchronization of Cortical Activity and its Putative Role in Information Processing and Learning. Annu Rev Physiol 1993; 55: 349–374

Smart TG, Paoletti P. Synaptic neurotransmitter-gated receptors. Cold Spring Harb Perspect Biol 2012; 4: a009662

Smith SS, Shen H, Gong QH, Zhou X. Neurosteroid regulation of GABAA receptors: Focus on the α4 and δ subunits. Pharmacol Ther 2007; 116: 58–76

Smolen P, Baxter DA, Byrne JH. How can memories last for days, years, or a lifetime? Proposed mechanisms for maintaining synaptic potentiation and memory. Learn Mem 2019; 26: 133–150

Sohal VS, Rubenstein JLR. Excitation-inhibition balance as a framework for investigating mechanisms in neuropsychiatric disorders. Mol Psychiatry 2019; 24: 1248–1257

Spiegel I, Mardinly AR, Gabel HW, Bazinet JE, Couch CH, Tzeng CP, et al. Npas4 regulates excitatory-inhibitory balance within neural circuits through cell-type-specific gene programs. Cell 2014; 157: 1216–1229

Staley KJ, Longacher M, Bains JS, Yee A. Presynaptic modulation of CA3 network activity. Nat Neurosci 1998; 1: 201–209

Stell BM, Mody I. Receptors with Different Affinities Mediate Phasic and Tonic GABA A Conductances in Hippocampal Neurons. J Neurosci 2002; 22: RC223

Südhof TC. The synaptic vesicle cycle. Annu Rev Neurosci 2004; 27: 509–547

Südhof TC. Neuroligins and Neurexins Link Synaptic Function to Cognitive Disease. Nature 2008; 455: 903–911

Südhof TC. The presynaptic active zone. Neuron 2012; 75: 11–25

Südhof TC. Neurotransmitter release: The last millisecond in the life of a synaptic vesicle. Neuron 2013; 80: 675–690

Südhof TC. The cell biology of synapse formation. J Cell Biol 2021; 220: e202103052

Südhof TC, Rizo J. Synaptic vesicle exocytosis. Cold Spring Harb Perspect Biol 2011; 3: a005637

Sutton MA, Ito HT, Cressy P, Kempf C, Woo JC, Schuman EM. Miniature Neurotransmission Stabilizes Synaptic Function via Tonic Suppression of Local Dendritic Protein Synthesis. Cell 2006; 125: 785–799

Sutton RB, Fasshauer D, Jahn R, Brunger AT. Crystal structure of a SNARE complex involved in synaptic exocytosis at 2.4 Å resolution. Nature 1998; 395: 347–353

Takao-Rikitsu E, Mochida S, Inoue E, Deguchi-Tawarada M, Inoue M, Ohtsuka T, et al. Physical and functional interaction of the active zone proteins, CAST, RIM1, and Bassoon, in neurotransmitter release. J Cell Biol 2004; 164: 301–311

The M, MacCoss MJ, Noble WS, Käll L. Fast and Accurate Protein False Discovery Rates on Large-Scale Proteomics Data Sets with Percolator 3.0. J Am Soc Mass Spectrom 2016; 27: 1719–1727

Tien NW, Kerschensteiner D. Homeostatic plasticity in neural development. Neural Dev 2018; 13: 1–7

Tokuda M, Ahmed BY, Lu YF, Matsui H, Miyamoto O, Yamaguchi F, et al. Involvement of calmodulin-dependent protein kinases-I and -IV in long-term potentiation. Brain Res 1997; 755: 162–166

Treiman DM. GABAergic Mechanisms in Epilepsy. Epilepsia 2001; 42: 8–12

Tremblay R, Lee S, Rudy B. GABAergic Interneurons in the Neocortex: From Cellular Properties to Circuits. Neuron 2016; 91: 260–292

Tukker AM, Wijnolts FMJ, de Groot A, Westerink RHS. Human iPSC-derived neuronal models for in vitro neurotoxicity assessment. Neurotoxicology 2018; 67: 215–225

Turrigiano G. Too many cooks? Intrinsic and synaptic homeostatic mechanisms in cortical circuit refinement. Annu Rev Neurosci 2011; 34: 89–103

Turrigiano G. Homeostatic synaptic plasticity: Local and global mechanisms for stabilizing neuronal function. Cold Spring Harb Perspect Biol 2012; 4: 1–17

Turrigiano GG, Leslie KR, Desai NS, Rutherford LC, Nelson SB. Activity-dependent scaling of quantal amplitude in neocortical neurons. Nature 1998; 391: 892–896

Turrigiano GG, Nelson SB. Homeostatic plasticity in the developing nervous system. Nat Rev Neurosci 2004; 5: 97–107

Uchino S, Waga C. SHANK3 as an autism spectrum disorder-associated gene. Brain Dev 2013; 35: 106–110

Ulrich T. Modulation of synaptic signalling complexes by Homer proteins. J Neurochem 2002; 81: 407–413

Uriu Y, Kiyonaka S, Miki T, Yagi M, Akiyama S, Mori E, et al. Rab3-interacting molecule γ isoforms lacking the rab3-binding domain induce long lasting currents but block neurotransmitter vesicle anchoring in voltage-dependent P/Q-type Ca2+ channels. J Biol Chem 2010; 285: 21750–21767

Vogel C, Marcotte EM. Insights into the regulation of protein abundance from proteomic and transcriptomic analyses. Nat Rev Genet 2012; 13: 227–232

Volpicelli LA, Levey AI. Muscarinic acetylcholine receptor subtypes in cerebral cortex and hippocampus. Prog Brain Res 2004; 145: 59–66

Wagenaar DA, Pine J, Potter SM. An extremely rich repertoire of bursting patterns during the development of cortical cultures. BMC Neurosci 2006; 7: 1–18

Wang J, Lee J, Liem D, Ping P. HSPA5 Gene encoding Hsp70 chaperone BiP in the endoplasmic reticulum. Gene 2017; 618: 14–23

Wang S, Chong ZZ, Shang YC, Maiese K. Wnt1 Inducible Signaling Pathway Protein 1 (WISP1) Blocks Neurodegeneration through Phosphoinositide 3 Kinase/Akt1 and Apoptotic Mitochondrial Signaling Involving Bad, Bax, Bim, and Bcl-x L. Curr Neurovasc Res 2012; 9: 20-31

Wang X, Liu Q, Zhang B. Leveraging the complementary nature of RNA-Seq and shotgun proteomics data. Proteomics 2014; 14: 2676–2687

Wang X, Lu T, Bendor D, Bartlett E. Neural coding of temporal information in auditory thalamus and cortex. Neuroscience 2008; 157: 484–493

Wang Y, Okamoto M, Schmitz F, Hofmann K, Südhof TC. Rim is a putative Rab3 effector in regulating synaptic-vesicle fusion. Nature 1997; 388: 593–598

Wang Y, Südhof TC. Genomic definition of RIM proteins: Evolutionary amplification of a family of synaptic regulatory proteins. Genomics 2003; 81: 126–137

Wang Y, Sugita S, Südhof TC. The RIM/NIM family of neuronal C2 domain proteins: Interactions with Rab3 and a new class of Src homology 3 domain proteins. J Biol Chem 2000; 275: 20033–20044

Watanabe M, Ohe Y, Katakai K, Kabeya K, Fukumura Y, Kobayashi I, et al. Glutamine is involved in the dependency of brain neuron survival on cell plating density in culture. Neuroreport 1998; 9: 2353–2357

Watt AJ, van Rossum MCW, Macleod KM, Nelson SB, Turrigiano GG. Activity Coregulates Quantal AMPA and NMDA Currents at Neocortical Synapses. Neuron 2000; 26: 659–670

Waxman EA, Lynch DR. N-methyl-D-aspartate receptor subtypes: Multiple roles in excitotoxicity and neurological disease. Neuroscientist 2005; 11: 37–49

Weidenhofer J, Bowden NA, Scott RJ, Tooney PA. Altered gene expression in the amygdala in schizophrenia: Up-regulation of genes located in the cytomatrix active zone. Mol Cell Neurosci 2006; 31: 243–250

Weidenhofer J, Scott RJ, Tooney PA. Investigation of the expression of genes affecting cytomatrix active zone function in the amygdala in schizophrenia: Effects of antipsychotic drugs. J Psychiatr Res 2009; 43: 282–290

Weisskopf MG, Castillo PE, Zalutsky RA, Nicoll RA. Mediation of Hippocampal Mossy Fiber Long-Term Potentiation by Cyclic AMP. Science (1979) 1994; 265: 1878–1882

West AE, Greenberg ME. Neuronal activity-regulated gene transcription in synapse development and cognitive function. Cold Spring Harb Perspect Biol 2011; 3: 1–21

Whissell PD, Lecker I, Wang DS, Yu J, Orser BA. Altered expression of δgABAA receptors in health and disease. Neuropharmacology 2015; 88: 24–35

Whitlock JR, Heynen AJ, Shuler MG, Bear MF. Learning Induces Long-Term Potentiation in the Hippocampus. Science (1979) 2006; 313: 1093–1097

Wichmann T, Soares J. Neuronal firing before and after burst discharges in the monkey basal ganglia is predictably patterned in the normal state and altered in parkinsonism. J Neurophysiol 2006; 95: 2120–2133

Woitecki AMH, Müller JA, van Loo KMJ, Sowade RF, Becker AJ, Schoch S. Identification of synaptotagmin 10 as effector of NPAS4-mediated protection from excitotoxic neurodegeneration. J Neurosci 2016; 36: 2561–2570

Xin F, Radivojac P. Post-translational modifications induce significant yet not extreme changes to protein structure. Bioinformatics 2012; 28: 2905–2913

Xu P, Berto S, Kulkarni A, Jeong B, Joseph C, Cox KH, et al. NPAS4 regulates the transcriptional response of the suprachiasmatic nucleus to light and circadian behavior. Neuron 2021; 109: 3268–3282

Xu X, Radulescu C, Utami K, Pouladi M. Obtaining Multi-electrode Array Recordings from Human Induced Pluripotent Stem Cell–Derived Neurons. Bio Protoc 2017; 7: 1–12

Yap EL, Greenberg ME. Activity-Regulated Transcription: Bridging the Gap between Neural Activity and Behavior. Neuron 2018; 100: 330–348

Yizhar O, Fenno LE, Prigge M, Schneider F, Davidson TJ, Ogshea DJ, et al. Neocortical excitation/inhibition balance in information processing and social dysfunction. Nature 2011; 477: 171–178

Young T-H, Huang J-H, Hung S-H, Hsu J-P. The role of cell density in the survival of cultured cerebellar granule neurons. J Biomed Mater Res 2000; 52: 748–53

Zalutsky RA, Nicoll RA. Comparison of Two Forms of Long-Term Potentiation in Single Hippocampal Neurons. Science (1979) 1990; 248: 1619–1624

Zhou W, Li X, Liu M, Zhao Y, Zhu G, Luo Q. Homeostatically regulated synchronized oscillations induced by short-term tetrodotoxin treatment in cultured neuronal network. BioSystems 2009; 95: 61–66

Ziv NE, Fisher-Lavie A. Presynaptic and postsynaptic scaffolds: Dynamics fast and slow. Neuroscientist 2014; 20: 439–452

Zucker RS, Regehr WG. Short-term synaptic plasticity. Annu Rev Physiol 2002; 64: 355–405

8 Acknowledgements

First of all, I would like to express my gratitude to my supervisors Prof. Susanne Schoch and Prof. Dirk Dietrich for giving me the unique opportunity of working on this project, which enabled me to gather very valuable experiences in this field of research and has enriched my academic growth in many ways. Thank you for your ongoing support, your patience and for sharing your exceptional expertise and outstanding knowledge with me.

I would also like to give special thanks to Dr. Alex Müller, who was always ready to offer help and advice with any kind of problem. Thank you so much for supporting me. Your help has really meant a lot to me.

Furthermore, I would like to thank Annika Mayer, Katia Poguzhelskaya, Hyuntae Kim and everyone else in the Schock/Becker/Dietrich/Pitsch Lab for the valuable advice and scientific exchange, as well as the moral support and for generally making it a great time. It was a pleasure to get to know you and to work with all of you.

I would also like to especially thank Sabine Opitz, Pia Trebing and Shayne Gilgenbach for doing incredible work every day, that made it possible for me to perform any experiments at all.

Finally, I would like to thank my best friends Jelena Miljanovic and Charly Behringer, as well as my family, for their unwavering support during the last years, their wisdom and all their love. Thank you for everything.